**Università degli Studi di Padova**

DEPARTMENT OF INFORMATION ENGINEERING
*MASTER'S DEGREE IN* BIOENGINEERING FOR
NEUROSCIENCES

# Assessment of hemodynamic and connectivity alterations in brain gliomas through sparse DCM

*MASTER CANDIDATE*
***Giulia Pagnin***

*SUPERVISOR*
***Prof.ssa Alessandra Bertoldo***

*CO-SUPERVISORS*
***Ing. Giorgia Baron***
***Dott.ssa Erica Silvestri***

ACADEMIC YEAR 2022/2023
15 DECEMBER 2022

*A MIA NONNA,*

*MARIA*.

# Abstract

Brain tumor is a neurological disease that not only affects perilesional areas, but can also produce altered interactions between brain regions remote from the lesion.

This thesis's main aim is to employ a sparse DCM algorithm, which has shown its ability to infer whole-brain EC and region-wise hemodynamic response through a Sparse Bayesian Learning approach, to infer whole-brain alterations in effective connectivity derived from resting-state fMRI data of patients affected by brain glioma.

Ideally, this model should provide a solid basis to develop novel techniques for predicting cognitive and behavioral deficits originating from brain lesions, other than simulation tools for designing personalized treatments based on the pathophysiology underlying brain disorders.

# Contents

# Introduction

Over the last few years, the study of the connectivity of the brain has been widely developed in order to obtain information about the interplay between brain structure and function. Thanks to non-invasive imaging techniques like Magnetic Resonance Imaging (MRI), it has been possible to study and explore the structural and functional interactions among different brain areas, relying on the representation of the brain connectome as a graph and on computational tools provided by the so-called graph theory. Graph theory framework allows the description of the brain by using nodes and edges, the former representing brain areas, while the latter the interactions between them. Those interactions can be real anatomical connections (structural connectivity), correlation values (functional connectivity), or directed links (effective connectivity).

Brain networks are invariably complex and share a number of common features with networks from other biological and physical systems. Network characterization of structural and functional connectivity data is increasing and rests on several important motivations. First of all, complex network analysis promises to reliably quantify brain networks with a small number of neurobiologically meaningful and easily computable measures. Those instruments are important to study brain disorders since the comparisons of structural or functional network topologies between subject populations appear to reveal presumed connectivity abnormalities in neurological and psychiatric disorders[1]. Specifically, human patients affected by brain glioma present several whole-brain functional and structural alterations that are usually pointed out in areas close to the brain tumor. However, one main limitation of performing the assessment of impaired regions only in perilesional areas is that they overlook distal brain regions or networks that could be functionally impaired by the tumor[2].

Brain tumors and especially gliomas haven’t been much studied in past years due to technical limitations. In recent years, thanks to the improvement and development of the MRI sequences, it has become possible to acquire images and signals with higher temporal and spatial resolutions, allowing the application of more sophisticated computational models to infer quantitative measures about the progression and the implications of the pathology, like Dynamic Causal Modelling. As already seen in other pathologies, the study of Effective Connectivity (EC) alterations could give us more information than the simple Functional Connectivity (FC) matrix. Thanks to acquired fMRI Blood Oxygen Level Dependent (BOLD) signals, it might be possible also to investigate the alterations in the area of effective connectivity. Several studies have investigated the glioma effect on structural and functional brain connectivity[3], but in-depth studies about effective connectivity, which is much more informative as it provides us with details regarding directionality, are scarcely present in the literature.

The most widely used mathematical framework to deal with effective connectivity is Dynamic Causal Modelling (DCM)[4]. This bayesian model has been proposed in a recent sparse version by Prando et al.[5],in order to make the estimation process more robust and reliable and allow to get estimates about the directed connections between brain areas through the so-called Effective Connectivity (EC) matrix and the hemodynamic response.

The aim of this Master Thesis is to investigate the hemodynamic and effective connectivity alterations that could be induced by brain gliomas through the application of sparse DCM[5]). Specifically, the relationship between metabolic alterations and the hemodynamics in the brain, obtained by [18F] Fluorodeoxyglucose (FDG) Positron Emission Tomography (PET) and fMRI BOLD signals, has been also analyzed to detect alterations both at single-subject and group levels. This relation is useful to test the sensitivity of the estimated HRF and thus the sensitivity of the model to the presence of the tumor, as well as demonstrating that the variations are subject-specific and variable with respect to the affected area.

This thesis is structured as follows:

- **Chapter 1** presents the resting-state fMRI framework and its relationship with PET.
- **Chapter 2** introduces the hemodynamic response and a particular hemodynamic model, called Balloon model, used to present it.
- **Chapter 3** presents the general concept of brain connectivity, providing an overview of the main graph theory approaches and of the theory of functional gradients.
- **Chapter 4** is dedicated to Dynamic Causal Modelling and the role of sparse DCM algorithm in inferring whole-brain effective connections.
- **Chapter 5** briefly describes brain gliomas and investigates their main effects on brain hemodynamics.
- **Chapter 6** illustrates the analyzed fMRI datasets, as well as the preprocessing pipeline, the methods used to relate the hemodynamic response and the PET microparameters, the effective connectivity analysis, and the initialization of the parameters set before the application of the sparse algorithm.
- **Chapter 7** graphically describes the results of the analysis and those returned by the algorithm, as well as other postprocessing elaborations applied to output data.
- **Chapter 8** presents a detailed discussion of the obtained results, providing some explanations that can justify the findings illustrated in the previous chapter.
- **Chapter 9** is dedicated to conclusions and the description of future work.

# 1 Functional brain activity at rest

## 1.1 Resting-state fMRI

fMRI is a neuroimaging technique that allows measuring neural activities by considering their relationship with physiological changes. During brain activation, local increase of cerebral blood flow and local cerebral blood volume are observable in conjunction with an increase in the cerebral metabolic rate of oxygen ($CMRO_2$), causing a local capillary and venous blood increase of oxygenation. Indeed, inside cells, cellular respiration allows producing ATP which is the primary energy carrier in living things and is fundamental for every brain activity. Especially in regions involved in the process of performing an activity, it can be observed that blood flow increases. In fact, cellular respiration requires two reagents: oxygen and glucose, which generate energy for the cells[6]. This usage and request for oxygen are translated into a variation of the balance of oxygenated and deoxygenated hemoglobin. The first one is a diamagnetic protein (magnetic moment = 0) while the second one is paramagnetic, which is sensitive to the magnetic field. As a result, in presence of local neural activities, it may be noticed an increase in oxygenated hemoglobin (HbO) and a decrease in deoxygenated hemoglobin (Hb). Due to its paramagnetic properties, the decrease of deoxyhemoglobin concentration lies at the base of fMRI by taking advantage of the so-called Blood Oxygen Level Dependent (BOLD) effect[7]. Consequently, the BOLD signals recorded in fMRI are a consequence of the so-called neuro-vascular coupling cascade, which considers the neural activity, metabolic rates, and physiological effects (cerebral blood flow (CBF), cerebral blood volume (CBV), and blood oxygenation).

The fMRI for activation studies is based on motor, visual or cognitive stimulation, while the resting state fMRI method allows to assess the individual behavior in undisturbed and rest conditions, apparently doing nothing. Using the relative changes from baseline in the BOLD signal during the performance of a task or in response to a stimulus, it results that certain areas of the brain are activated. In recent years, there has been an increasing interest in the application of this technique at rest, in fact resting-state fMRI has allowed to investigate synchronous activations between regions that are spatially distinct, occurring in the absence of a task or stimulus, revealing the identification of Resting State Networks (Figure 1.1)[7].

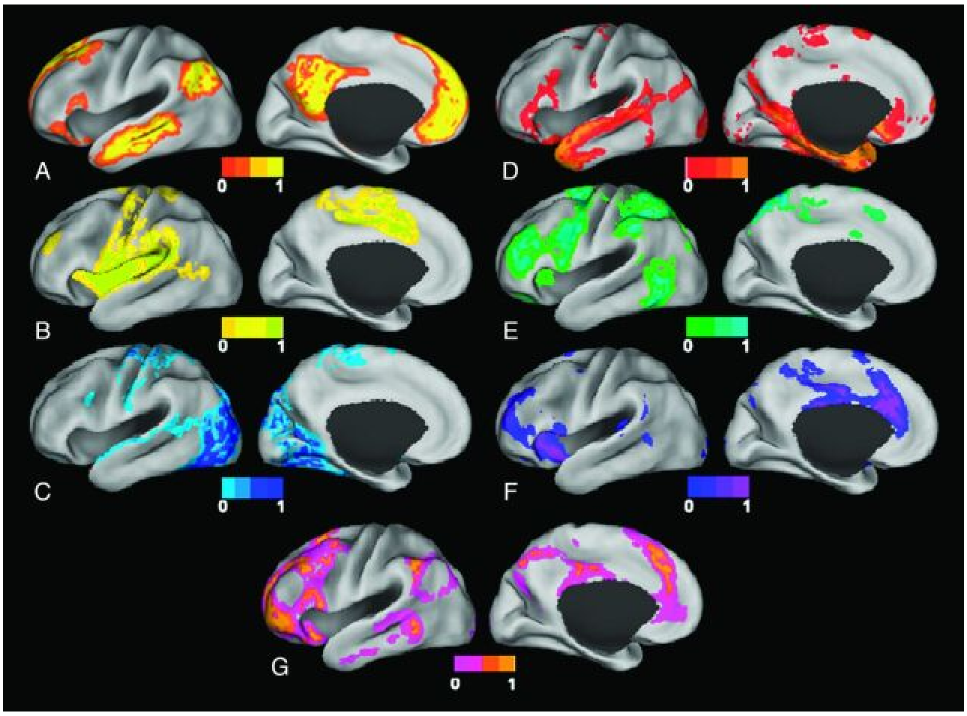

**Figure 1.1. Surface plots of RSNs.** (A) Default mode network. (B) Somatomotor network. (C) Visual network. (D) Language network. (E) Dorsal attention network. (F) ventral attention network. (G) Frontoparietal control network[7].

## 1.2 Combining fMRI and [18F]FDG PET

Combining fMRI and [18F]FDG PET provided new tools to study functional processes in the brain. Both fMRI, which measures rapid changes in blood flow and oxygenation during activation, and PET, which assesses glucose metabolism, are highly studied to evaluate brain activity and functions. Differences between the fMRI activation data and the PET activation data were discovered in both space and quantity, but these findings show the viability of using combined PET-MRI to investigate the brain simultaneously in active and passive states, providing rich and complementary data to advance our understanding of brain function and neural networks[8].

Absolute quantitative analyses of the dynamic PET data allow to follow the different physiological processes the injected radiotracer underwent during the PET experiment. For what concern the [18F]FDG, this is a glucose analogue which enters the tissue via glucose transporters and can then be either phosphorylated by hexokinases to [18F]FDG-6-phosphate ([18F]FDG-6-P), or transported from tissue back to blood. [18F]FDG-6-P cannot be transported out of the tissue, and is not metabolized further through glycolysis like glucose-6-phosphate [9], [10] . In particular, by interpreting [18F]FDG plasma concentration and tissue activity curves with compartmental models with three (3K model) rate constants, one arrives at [18F]FDG transport and phosphorylation [11]. Kinetic models for PET typically derive from the one-, two-, or three-compartment model in which a directly measured blood curve (concentration of radiotracer in the blood as a function of time) serves as the model's input function. The model's differential equation coefficients are assumed to be fixed values that reflect the unique kinetic characteristics of the system's individual tracer molecule. In the case of [18F]FDG PET dynamic data, the kinetic model is the two compartment three kinetic parameters depicted in Figure 1.2.

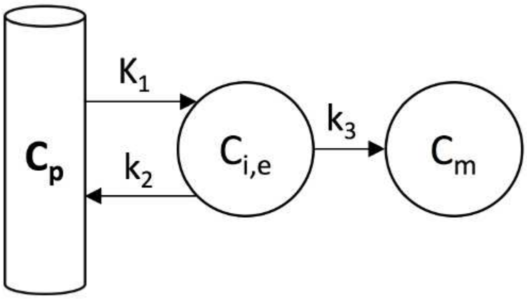

**Figure 1.2. Two tissue compartment model.** The figure shows the structure of the 2TC-3k model for measuring the metabolic rate of glucose with $^{18}$F-FDG (adapted from ). $C_P$, arterial plasma $^{18}$F-FDG concentration; $C_{i,e}$, tracer interstitial and intracellular concentration; $C_m$, $^{18}$F-FDG 6-phosphate intracellular concentration; *K1* and *k2*, $^{18}$F-FDG transport from plasma to interstitial-intracellular space and back, respectively; *k3*, $^{18}$F-FDG phosphorylation.[12]

The related differential equation is reported in (1.1), where CP represents the arterial plasma 18F-FDG concentration; Ci,e, the tracer interstitial and intracellular concentration; Cm, the 18F-FDG 6-phosphate intracellular concentration; CT represents the total activity concentration within the voxel; Cb(t), the arterial blood tracer concentration; K1 (ml/cm3/min) and k2 (1/min), the 18F-FDG transport from plasma to interstitial-intracellular space and back, respectively; k3 (1/min), the 18F-FDG phosphorylation; and finally Vb is the fraction of the total volume (i.e. voxel) occupied by blood pool[12].

$$\begin{cases} \frac{dC_{i,e}(t)}{dt} = K_1 C_P(t) + (k_2 + k_3) C_{i,e}(t) & C_{i,e}(0) = 0 \\ \frac{dC_m(t)}{dt} = k_3 C_{i,e}(t) & C_m(0) = 0 \\ C_T(t) = (1 - V_b)(C_{i,e}(t) + C_m(t)) + V_b C_b(t) \end{cases} \qquad (1.1)$$

Several literature studies have provided some insights into the complementary information provided by these two neuroimaging techniques. As illustrated in the paper of Zhang et al.[13], the authors investigated the relationship between the regional cerebral glucose metabolism rate (rGMR) of FDG-PET and the hemodynamic response of BOLD fMRI signals in patients affected by schizophrenia, finding a significant correlation between them. The relationship between neuronal activity, oxygen metabolism, and hemodynamic responses has been also investigated in rat somatosensory cortex, finding a linear increase in cerebral oxygen consumption with synaptic activity[14].

# 2 The hemodynamic model

## 2.1 The Hemodynamic Response Function

With the advent of event-related fMRI, there is a rising recognition of the importance of nonlinearities between the actual observed signal and neuronal activity. These nonlinear relationships are frequently portrayed as interactions between stimuli, which can cause the suppression and lengthening of the latency of responses to one stimulus as a result of another stimulus[15]. The change unit in the MR signal measured by the coils due to the increase of neural activity is called Hemodynamic Response Function (HRF). Its shape varies with the stimulus properties, such as short or persistent stimulus that can potentially lead to a plateau status in the hemodynamic response (Figure 2.1).

An important property of the hemodynamic response is the initial dip (Figure 2.1), an undershoot before the typical signal shape of the hemodynamic response. It has raised many hypotheses about the reason for its presence, but none of these has been demonstrated as the cause of this phenomenon[16]. One of these hypotheses supposes this initial dip is caused by the increase of deoxyhemoglobin after the decrease of oxyhemoglobin before the incoming blood flow due to the activation of that brain area after the stimulus[16].

In addition, the BOLD signal time course during brain activation has been reported to exhibit several transient features at the end of the stimulus: a post-stimulus undershoot that has been modeled as an elevated oxygen extraction after the flow has returned to baseline, required to replenish depleted tissue oxygen stores[17].

Many models have been developed to describe these hemodynamic features [15], [18], like the biophysical model for the BOLD effect or the Balloon model[18].

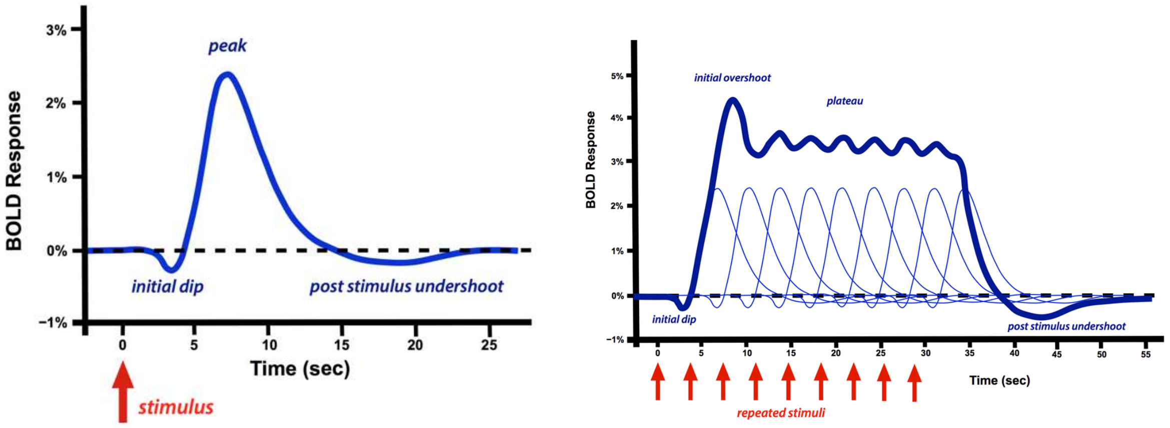

**Figure 2.1: Hemodynamic response.** The figures show the hemodynamic responses following a short (left panel) and repeated (right panel) stimulus that is modeled as a stimulus-evoked BOLD response following neural activation[19].

## 2.2 The Balloon hemodynamic model

The hemodynamic model in Figure 2.2 essentially combines the Balloon model and a simple linear dynamical model of changes in regional cerebral blood flow (rCBF) caused by neuronal activity.

The rCBF is described through a linear dynamic model, composed of two equations:

$$f_{in} = s \tag{2.1}$$

$$\dot{s} = x(t) - ks - \gamma(f_{in} - 1) \tag{2.2}$$

In particular, this description represents the model of a damped oscillator governed by the later described biophysical parameters $k$ and $\gamma$. The variable $s$ represents the induced flow signal corresponding to the rate of change of the normalized flow entering the affected brain area. In addition, the vasodilatation signal $s$ is generated by the neuronal activity $x(t)$.

The Balloon Model describes the behavior of an active brain area regarded as a venous balloon crossed by venous blood that expands when there’s a higher blood flow compared with a baseline condition. Together with effective connectivity, the Balloon Model is a fundamental component that contributes to describe, as will be illustrated in the following sections, the BOLD signal in DCM. All variables are expressed in normalized form, relative to resting values. The BOLD signal $y$ is taken to be a static nonlinear function of normalized venous volume $v$ and normalized total deoxyhemoglobin voxel content $q$.

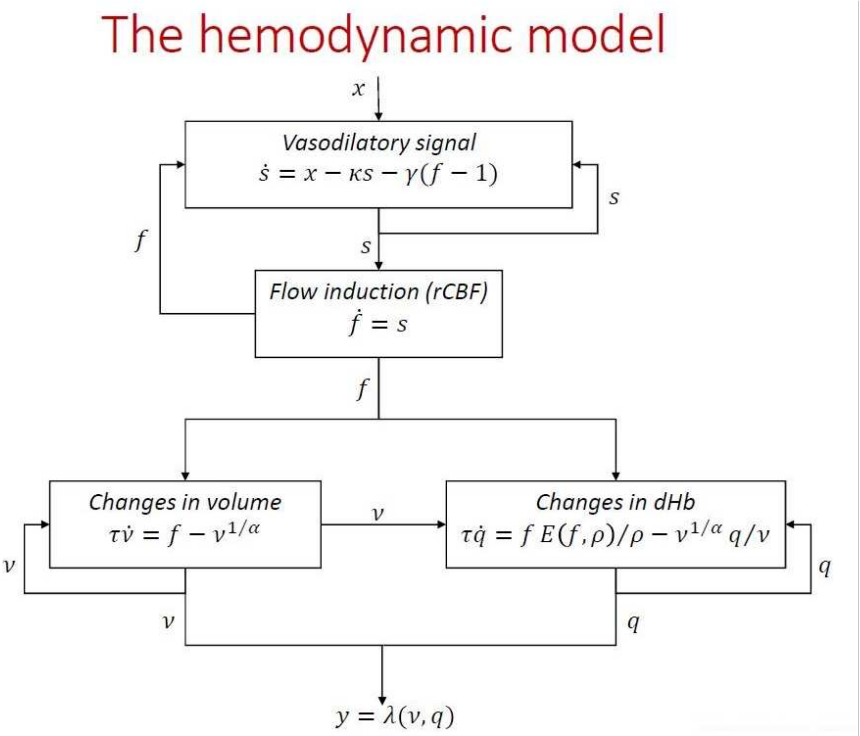

**Figure 2.2: Hemodynamic Model.** Scheme of the hemodynamic model in a region of interest, the neuronal activity $x$ causes an increase in vasodilation and a signal activity-dependent s that in turn augments the blood flow. This increase is followed by a change in volume and deoxyhemoglobin, the whole process flows into the BOLD signal $y$[4].

# 3 Effective Connectivity

## 3.1 Human brain connectivity

The principles of organization of the human brain, considered as a complex network of regions interacting with each other, reflect a combination of segregated (local) and integrated (distributed) processes that define brain function [20]–[22]. The theory of functional segregation considers different areas of the brain as specialized for different functions, while functional integration underlies the idea that the cognitive processes are not limited to specific and restricted brain regions, but rather they are part of a bigger interplay involving several areas. Both are based on the study and analysis of anatomical and functional connections between brain regions, which translates into the wider framework of brain connectivity[5].

The main forms of brain connectivity, which allow to study and analyze the interactions between brain regions, can be summarized as follows (Figure 3.1)[23]:

- Anatomical or Structural Connectivity (SC) measures the density or probability of anatomical pathways that connect two brain areas. This approach aims to provide a complete description of the physical tracks of the human nervous system, the so-called human brain *connectome*[22].

- Functional Connectivity (FC) gives information about the temporal correlation in neuronal activation between spatially remote areas through the estimation of pairwise statistical dependencies.

- Effective Connectivity (EC) explores the causal and thus directed influence that one neuronal system exerts over another. It is expressed by a wiring diagram that reflects directional effects within a neuronal network, unlike SC and FC which don’t give any information about the causality or directionality of those connections.

The difference between EC and FC with respect to SC is that they refer to more abstract metrics with no immediate connection to physical and anatomical structures.

The advantage of introducing directionality, thus the added value of effective connectivity, is that it refers explicitly to the directed influence of one neural system over another, either at a synaptic or regional level.

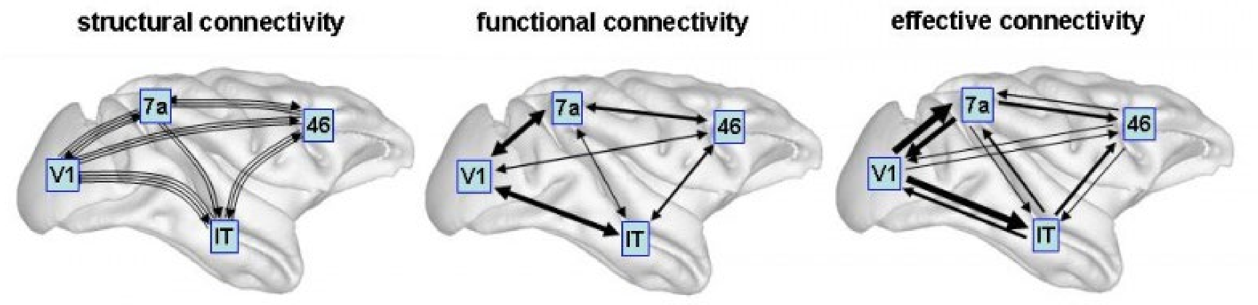

**Figure 3.1: Structural, Functional, and Effective Connectivity.** On the left, undirect and weighted Structural Connectivity (different number of connections), in the middle: undirect and weighted Functional Connectivity (different node strength connections); On the right: direct and weighted Effective Connectivity (different directed connections)[24].

# 3.2 Graph theoretical tools for the analysis of brain networks

Graph theory is based on the consideration of the brain as a graph composed of vertices (also called nodes or points) that are connected by edges (also called links or lines) which, in their simplest form, can be summarized in the form of a connection (or adjacency) matrix. In such a graph model of the brain, the nodes could refer to the individual neurons or entire cerebral areas, while the edges represent the interactions between them. Edges could be binary or weighted values, and they can be directed or undirected, depending on how interactions are estimated from empirical data[20]. This way of envisioning the brain allows to analyze complex networks in order to quantify their structural and functional infrastructure[21].

In fact, the two most common species of brain graphs describe structural and functional connectivity among neural elements. Structural graphs are generally sparse and temporally stable, while functional graphs record statistical dependencies among neuronal time series and hence are often dense and highly variable across time[20].

Graphs can be investigated on the basis of the adjacency (weighted or binarized) matrix, obtaining information as the node degree, which is the number of edges incident on that specific node, or the node strength, an analogue of node degree but with weighted edges. Another pathway is based on the graph embedding or dimensionality reduction of that matrix, for example, Principal Component Analysis or Laplacian Maps.

The development of network neuroscience has been sparked by the use of graph theory to represent the intricate structure and operation of the brain. Figure 3.2 illustrates the four steps through which graph theory can be used to investigate structural and functional brain networks. The first step is to define the network nodes, which can be identified by electroencephalography or multielectrode-array electrodes, by MRI or diffusion tensor imaging data. The next step is to calculate a continuous measure of node association, like the connection probability between two regions of an individual diffusion tensor imaging data set functional connections, in order to define an association matrix by adding up all pairwise associations between nodes. The final step regards the estimation of the network parameters of interest in this graphical representation of the brain network[21].

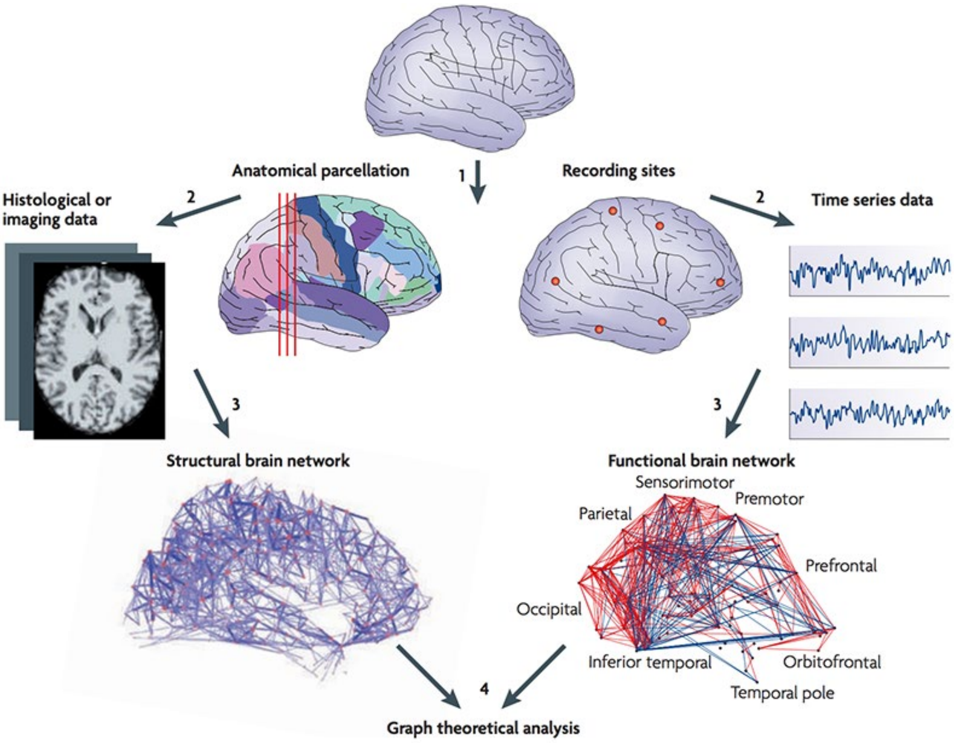

**Figure 3.2: Structural and functional brain networks.** Graph theory allows for studying structural and functional brain networks[25].

## 3.3 Gradients

Another effective procedure recently used in many studies is graph embedding using laplacian eigenmaps; this method is useful not only for dimensionality reduction (i.e. spectral clustering on ROIs based on their connectivity profile) but also because of its physical interpretation as spectral decomposition of the graph signal.

An easy way to derive the graph Laplacian is to express the connectivity matrix as (weighted) adjacency matrix $W$, indexed by nodes, where $Wij$ is 0 if and only if there is no edge between nodes $i$ and $j$, and $Wij$ represents the weight of the edge ($i$,$j$) otherwise. By summing a row of W, we obtain the strength of the corresponding node and by entering these values in a diagonal matrix, called degree matrix $D$, it is possible to obtain the graph Laplacian as $L = D – W$. From this matrix, the eigenvectors and corresponding eigenvalues are obtained. The Laplacian eigenvectors, commonly known as connectivity gradients, have been found to effectively describe cortical architecture as a continuum of spatial harmonics that can overlap in space (graph nodes)[26].

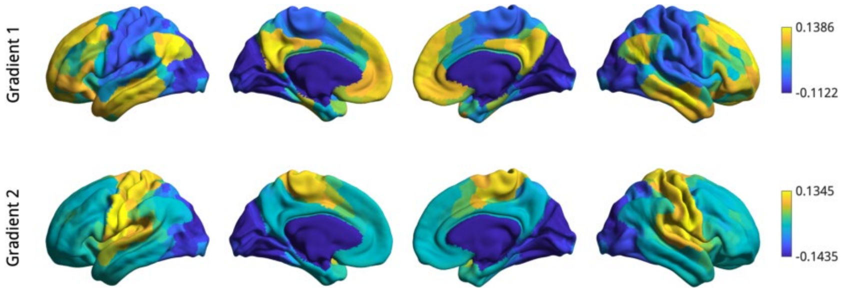

**Figure 3.3: Gradients.** Cortical surface representation of the human brain’s Gradient 1 and Gradient 2[27].

Furthermore, as shown in Figure 3.4, it has been noticed that FC-derived gradients evolve followings the hierarchy of functional organization of networks[28].

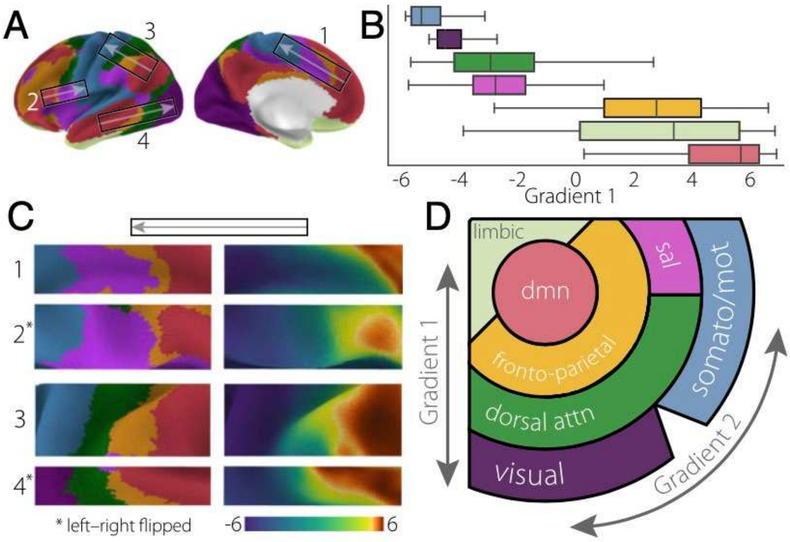

**Figure 3.4. Relationship between gradients and brain networks.** (A) Principal gradient values from each of the seven networks are presented as (B) boxplots ordered by the mean value. (C) Illustrative cutouts were taken from figure A to show the repeated patterns of network spatial adjacency captured by the principal gradient. (D) A schematic of the spatial relationships of canonical resting-state networks[28].

In this Master Thesis, some of these tools will be applied to EC. To the best of our understanding, gradients have never been applied to effective connectivity in oncological patients. The study of the impact of ischemic stroke on connectivity gradients, as studied in [29], is the only found application of this method to pathology.

# 4 Dynamic Causal Modelling

## 4.1 Dynamic Causal Modelling

As presented in seminal work by Friston et al.[4], the DCM approach builds on a nonlinear multiple input multiple output (MIMO) dynamical system; indeed the BOLD fMRI response is the output for each of the brain areas, considering experimentally designed inputs (tasks) and random neural fluctuations (resting-state). Starting from the input BOLD signals, the procedure of model inversion allows estimating the hemodynamic response function, the neuronal states, and the matrix of effective connections, in order to obtain an estimate of the BOLD timeseries resulting from the model as similar as possible to the acquired BOLD signals from fMRI. The process is based on the application of Variational Bayes and Expectation-Maximization algorithms, as deeply described in Friston et al.[4].

The general mathematical model of DCM provides a two-level system consisting of a differential equation that gives information about the coupling among neural populations, and a dynamic map from the neuronal activity to the measured BOLD signal y(t), the so-called neuro-vascular coupling (4.1).

$$\begin{aligned} \dot{x}(t) &= f\left(x(t), u(t); \theta_f\right) + v(t) \\ y(t) &= h(x(t); \theta_h) + e(t), \quad e(t)\sim\mathcal{N}(0, R) \end{aligned} \tag{4.1}$$

The first equation in (4.1) expresses the relationship between the behavior of the neuronal activity of the brain regions at time $t$, $x(t) = [x_1(t) \ldots x_n(t)]^T$. The term $u(t)$ represents the external stimuli or task demands during the experiment; $v(t)$ stands for the stochastic contribution due to intrinsic brain fluctuations; $q_f$ describes the model at the neuronal level (including effective connectivity). The second equation gives information about the expression of the BOLD signal through the hemodynamic model, evaluated as a combination of two components: the so-called Balloon Model and the dynamic model related to the regional Cerebral Blood Flow (rCBF) variation.

It describes the evolution of the BOLD signal at time *t* with $h(x(t); q_h)$ representing the hemodynamic response defined by its own biophysical parameters $q_h$, while the additional term $e(t)$ symbolizes the observation white gaussian noise with covariance matrix *R*.

The original formulation of DCM[4] regarded that neural activity was caused only by external stimuli $u(t)$, without considering the stochastic term $v(t)$, and formulates the *f* function as bilinear:

$$\dot{x}(t) = \Big(A + \sum_{j=1}^{m} u_j(t)B_j\Big)x(t) + Cu(t) \tag{4.2}$$

In formula (4.2), term *A* stands for the network connectivity in absence of external excitations, $B_j$ counts as the change in neuronal coupling brought on by the *j-th* input and C simulates the direct impact of experimental manipulations on neuronal activity.

To handle resting-state fMRI (rs-fMRI) data, Friston et al.[30] developed a variant of the original DCM. The absence of external stimuli in this situation, $u(t)=0$, entails that the brain activity is driven only by random fluctuations $v(t)$. It follows that the function *f* in (1.3) is linearized as:

$$\dot{x}(t) = Ax(t) + v(t) \tag{4.3}$$

considering *A* as the effective connectivity matrix. The hemodynamic component is still modeled through the nonlinear system described in Figure 2.1.

## 4.1.1 Biophysical parameters of the hemodynamic response

Considering the model described in (4.1) and Figure 2.1, the hemodynamic component is characterized by the parameter $q_h$ that includes 5 biophysical parameters: $q_h$ = {k,g,t,a,r}. The prior values of those parameters commonly employed in the model are reported in Table 4.1.

| | | | |
|---|---|---|---|
| $k$ | Rate of signal decay | 0.65 per s | 0.015 |
| $\gamma$ | Rate of flow-dependent elimination | 0.41 per s | 0.002 |
| $\tau$ | Hemodynamic transit time | 0.98 s | 0.0568 |
| $\alpha$ | Grubb's exponent | 0.32 | 0.0015 |
| $\rho$ | Resting oxygen extraction fraction | 0.34 | 0.0024 |

**Table 4.1. Biophysical parameter priors.** The table shows , for each parameter, its brief description, the prior value for the mean and for the variance.

As previously described in figure 2.1, every parameter has a specific biological meaning and the increase or decrease of their values causes a variation in the hemodynamic response.
The *Signal Decay k* reflects the decay or elimination signal *s(t)* present in (2.2), which follows the impulse. At the spatial scale of a few mm, it appears that the rapid spatial diffusion of *s(t)* leads to an increase in cerebral blood flow in the region in question through relaxation of the arteriolar musculature.
The *Autoregulation γ* represents the time constant of the autoregulatory feedback mechanism, the physiological nature of which remains unspecified. It could, in fact, indicate how long it takes a vessel to return to its basal condition after the signal of vasodilation.
The *Hemodynamic transit time* τ is defined as the ratio of venous volume to blood flow under resting conditions. In other words, it is the time taken by the blood flow to cross the venous balloon, i.e. a possible brain area, also called Mean Transit Time (MTT).
The *Grubb's exponent α* regulates the outflow from the venous balloon through a non-linear relationship.
The *Resting oxygen extraction ρ* denotes the fraction of oxygen that is extracted from the bloodstream as it passes through the venous balloon and serves metabolic functions[15].

# 4.2 Sparse Dynamic Causal Modelling

The sparse Dynamic Causal Model (sparse DCM), presented in Prando et al.[5], is an improvement of the standard resting-state DCM approach developed by Friston et al.[30] that worked only with few nodes. This method allows estimating whole-brain effective connectivity from resting-state fMRI data and thus gives much more information than the standard approach.
Differently from the original DCM formulation, which assumes that neural activity proceeds from external stimuli, the sparse algorithm builds on a variant of DCM (the stochastic DCM[30]).

The reformulation provided by the sparse DCM includes a discretization of the original non-linear continuous-time model and a statistical linearization of the hemodynamic response function, that generates a Gaussian prior on the HRF that can be later exploited for model inversion. This allows us to better exploit the low temporal resolution of fMRI scanners and decrease the computational burden without losing statistical performance.

The sparse estimation algorithm alternates between an RTS smoother, and the update of θ through the maximization of Q(θ, $\theta^{(l)}$) (Section 2.3 of [5]). At each iteration, the ML estimation of the hyperparameters through the reweighted procedure is executed as an inner step (the details of the complete procedure are reported in Appendix B of [5]).

## 4.2.1 Effective Connectivity matrix

In sparse DCM[5] the discretization and linearization procedure lead to the system described in (3.1), where A refers to the effective connectivity matrix, *w(k)* represents the white gaussian noise component associated with endogenous fluctuations with variance Q and *e(k)* describes the measurement error through a stochastic white gaussian variable with variance *R*.

$$\begin{cases} \mathbf{x}(k+1) & = & \mathbf{A}\mathbf{x}(k) + \mathbf{w}(k) \\ y(k) & = & \mathbf{H}\mathbf{x}(k) + e(k). \end{cases} \tag{4.4}$$

The two matrices, respectively *A* and *H,* are defined in (4.5).

$$\begin{gathered} \mathbf{A} := \begin{bmatrix} e^{AT_R} & 0 \\ I_{n(s-1)} & 0 \end{bmatrix} \\ \mathbf{H} := \begin{bmatrix} h_{1,0} & 0 & \cdots & 0 & h_{1,1} & 0 & \cdots & 0 & \cdots & h_{1,s-1} & 0 & \cdots & 0 \\ 0 & h_{2,0} & \ddots & \vdots & 0 & h_{2,1} & \ddots & \vdots & \cdots & 0 & h_{2,s-1} & \ddots & \vdots \\ \vdots & \ddots & \ddots & 0 & \vdots & \ddots & \ddots & 0 & \cdots & \vdots & \ddots & \ddots & 0 \\ 0 & \cdots & 0 & h_{n,0} & 0 & \cdots & 0 & h_{n,1} & \cdots & 0 & \cdots & 0 & h_{n,s-1} \end{bmatrix} \end{gathered} \tag{4.5}$$

The matrix of interest *A* is one of the parameters of $q = \{A, s, h_1, \ldots, h_n, l_1, \ldots, l_n\}$, obtained after the optimization of the Expectation-Maximization (EM) procedure (explained in detail at section 2.3 of [5]).

The EC matrix is non-symmetric and each row and column represents a specific region of interest. An example of an EC matrix is displayed in (Figure 4.1). The information about the effective connections between each pair of regions is directed, for example, the weight of the link in position 10,20 (row, column) of the matrix represents the strength of the link that region 20 exerts on region 10. Another peculiarity of the EC matrix is that it might be a matrix with positive or negative values. In the example matrix, positive connections are highlighted in yellow, while negative ones are in blue. Values in the diagonal give information about the recurrent links of each region.

Through the Graph Theory representation of the brain, it's then possible to visualize the so-called nodes (regions of interest like brain networks) and the respective edges, our effective connections.

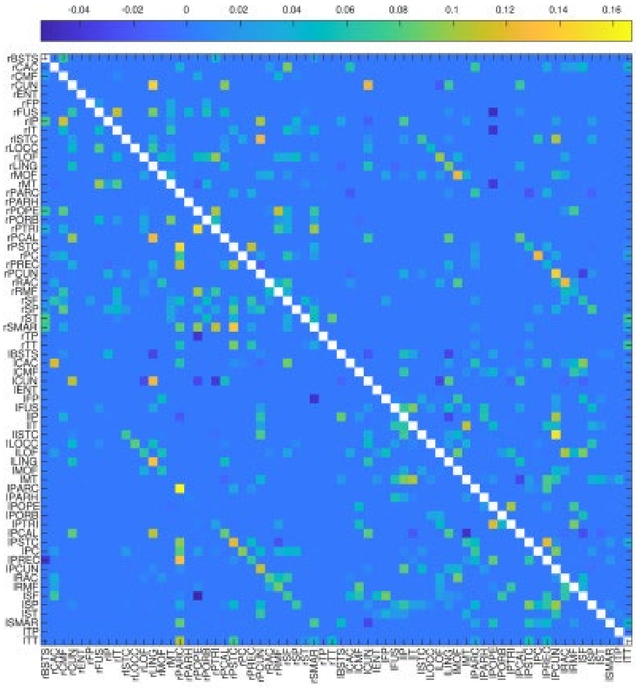

(a) Estimated EC.

**Figure 4.1: Estimated Effective Connectivity Matrix.** The figure shows an example of the effective connectivity matrix of 66 brain regions, in yellow positive connections and in blue negative ones[5].

# 5 Brain gliomas: connectivity disruptions and hemodynamic alterations

## 5.1 Brain tumors

The most frequent form of brain tumor in human adults is glioma, which represents 81% of all malignant brain tumors[31]. Compared to other types of brain tumor, gliomas typically have a poor prognosis, as can be noticed in (Figure 5.1). Traditionally, factors influencing prognosis included patient age and physical condition, tumor histopathology and location, surgical treatment (such as the extent of resection), post-surgical adjuvant therapy and others.

World Health Organization (WHO) grade is a widely used grading system for gliomas. High-grade gliomas (HGGs), such as grade-III (anaplastic astrocytoma) and IV (glioblastoma multiforme) gliomas are thought to grow more quickly and have worse outcomes than WHO grade-II gliomas[32].

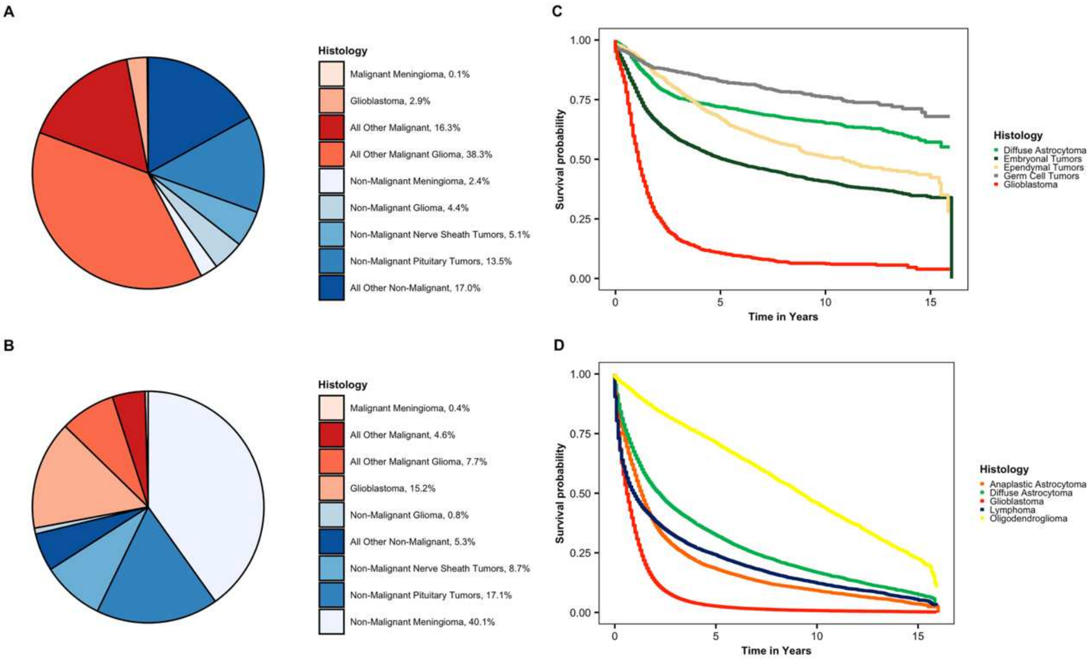

**Figure 5.1: Incidence and survival for primary brain and other CNS tumors.** Distribution of primary brain and other CNS tumors by behavior for **A** children (0–19 years), and **B** adults (20 years and older). Kaplan–Meier survival curves for the five most common histologies within 4 children (0–19 years), and **D** adults (20 years and older)[33].

## 5.2 Hemodynamic alterations in gliomas

The studies on humans have focused only on alterations in certain brain networks like the Primary Motor Cortex (PMC) in the affected hemisphere with respect to the contralateral one. Indeed, it was pointed out that the BOLD signal intensity and the Time To Peak (TTP), which are related to the hemodynamic response, are altered in the tumor-affected PMCs hemisphere compared to the unaffected one[34].

While this work focused on the alterations of the whole BOLD signal, the study by Montgomery et al.[35] describes a whole-experimental procedure carried out on mice to fully characterize the hemodynamic response function in tumor conditions.

Specifically, the study is based on the observation of glioma growth and hemodynamic alterations in different brain areas after the injection of glioma cells into the subcortical white matter of the right frontal cortex. The observation started from 4 days post injection (DPI) until 36 DPI only for surviving subjects.

It was observed that the timeseries of resting-state neural activity (GCaMP) and hemodynamic (HbO, HbR, and HbT) from the tumor, at early timeseries, were clearly correlated with the contralateral anterior region (Figure 5.2 B). However, as the tumor progresses (32-34 DPI), it is possible to observe a decrease in amplitude and high frequency content of the neural activity, while the hemodynamic activity seems to slow down, especially HbT (Figure 5.2 C). This change in the dynamics of the signals is also highlighted by the decrease in correlation of GCaMP and HbT signals both in bilateral frontal and visual regions during tumor progression (Figure 5.2 D).

To figure out alterations in the surrounding and contralateral regions of the brain, they analyzed the hemodynamic response functions in motor and whisker regions (Figure 5.3 C). Apart from variations in amplitude and some bilateral activity, the only consistent effect of the tumor is a slightly negative response visible within the lesioned area in late time points (pink arrowheads in mouse 3), while HRFs have similar shapes and amplitudes in both frontal and whisker regions at early and late time-points. The disruptions to the deconvolved HRFs in the tumor-bearing region (d) are visible in all animals.

Focusing on the alterations in hemodynamic response functions, during tumor progression from 11 to 28 DPI, the decrease in amplitude and distortion in the normal shape of the response is clearly visible (Figure 5.4 C and F).

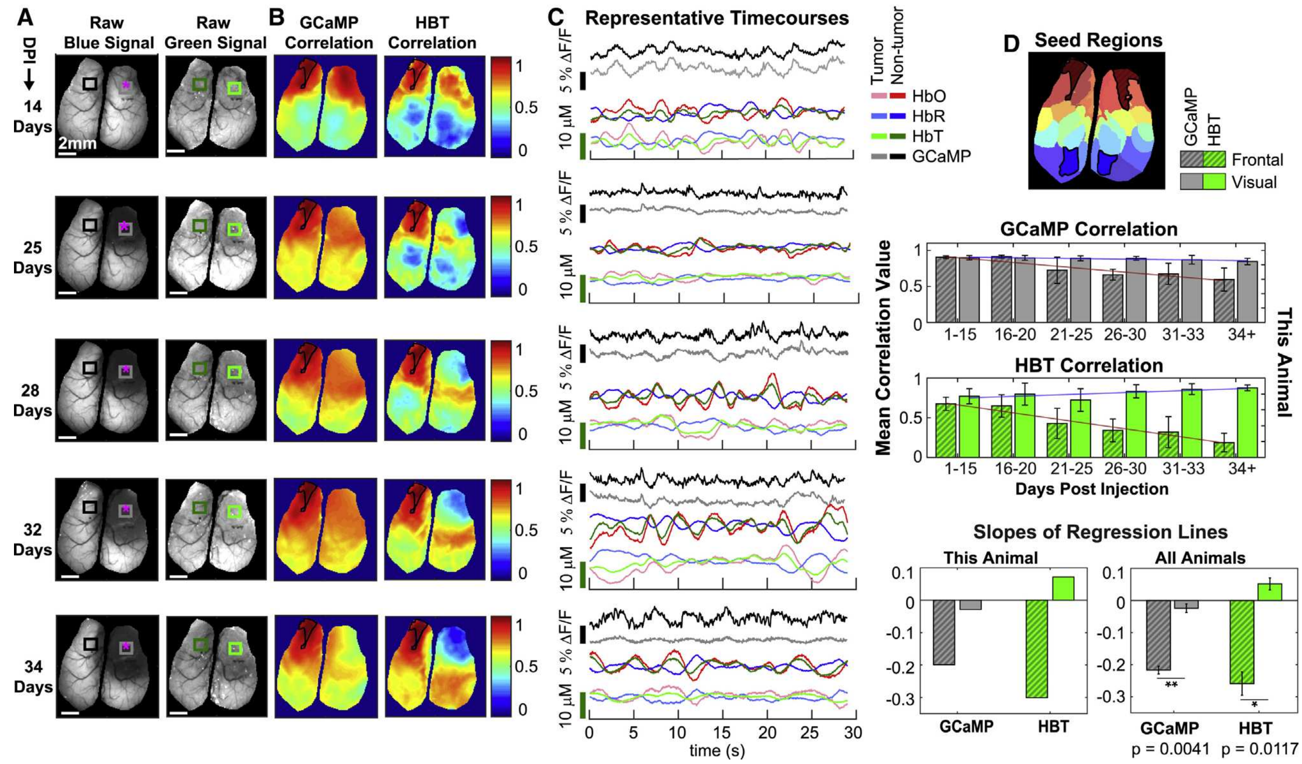

**Figure 5.2. Correlation of GCaMP and Hemodynamic Signals between tumor and non-tumor regions during tumor progression.** **(A)** Images of the raw fluorescence signal, in magenta the site of injection. **(B)** Correlation of signals relative to the anterior left frontal seed region (contralateral to the tumor) for both GCaMP6f and HbT. **(C)** Time courses were taken from representative runs for bilaterally symmetric tumor and non-tumor regions of interest (ROIs) indicated by squares in (A). **(D)** Top: k-means clustered regions used to choose frontal cortex (dark red diagonal hatch line fill) and visual cortex (dark blue) regions for correlation analysis. Center: bar plots of both GCaMP6f and hemodynamic correlation between bilateral frontal (gray with diagonal hatch line fill) and visual regions (gray fill) as the tumor progresses, shown for one representative animal. Bottom: slopes of regression lines for GCaMP6f and hemodynamic correlation trends for one representative animal, and across all animals.

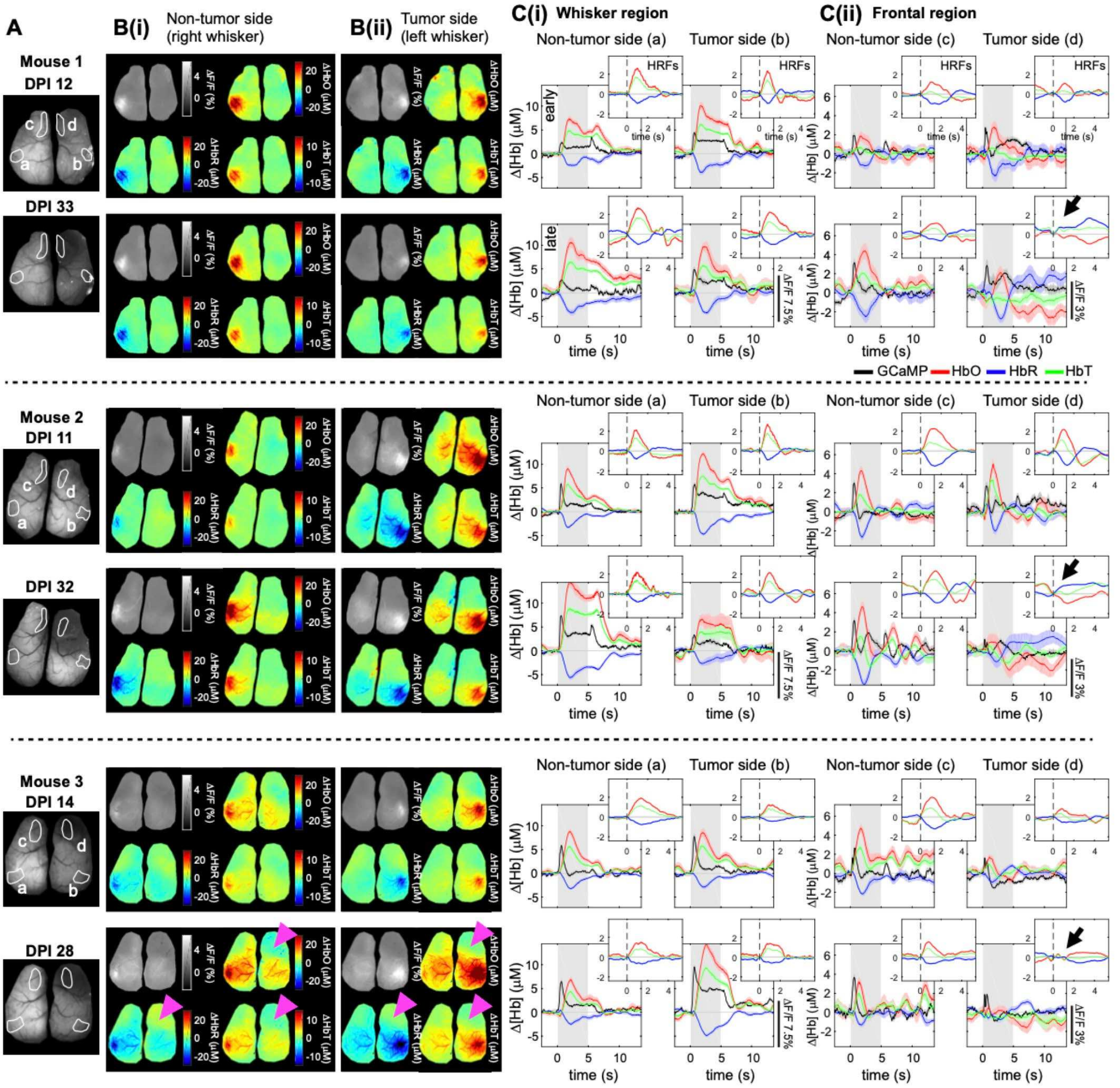

**Figure 5.3. Neurovascular response to whisker stimulus during tumor progression in all mice. (A)** ROIs chosen, belonging to motor and whisker regions. **(B)** Neural and hemodynamic averaged responses maps. B(i) shows non-tumor side responses to right whisker pad stimulation, and B(ii) shows tumor-side responses to left whisker pad stimulation **(C)** Shows averaged neural and hemodynamic responses in the ROIs indicated in A.

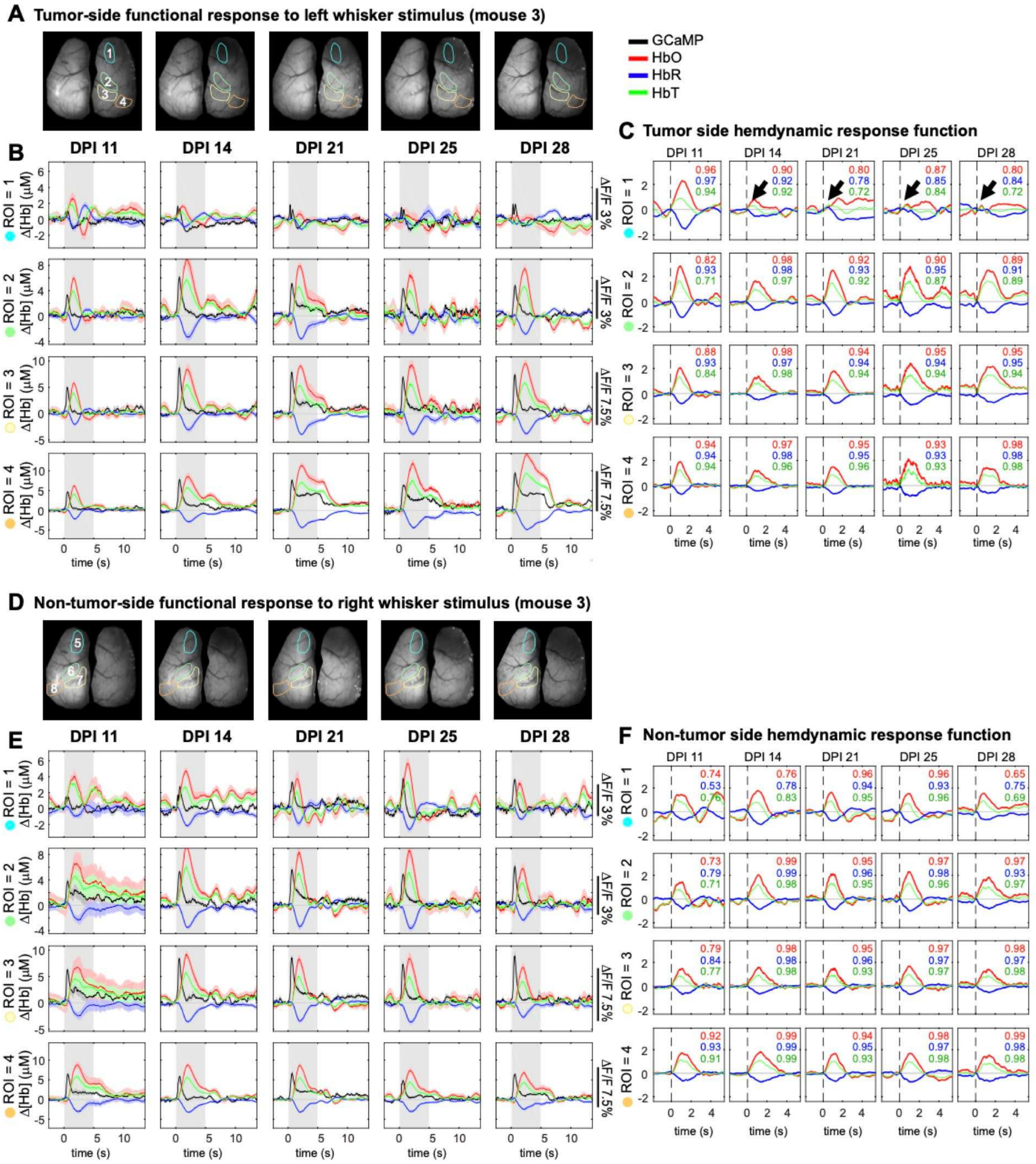

**Figure 5.4. Whisker stimulus (mouse 3). (A and D)** show regions of interest across 5 post-injection time-points (DPIs 11-25) in mouse 3, with A focusing on the tumor side of the cortex, and D focusing on the non-tumor side. **(B and E)** Averaged neural and hemodynamic responses within the ROIs indicated in A / E (rows) for progressive DPIs (columns). B shows tumor-side responses to contralateral (left) whisker stimulation, while E shows non-tumor side responses to contralateral (right) whisker stimulation. **(C and F)** show respectively tumor and non-tumor side hemodynamic response function, it is a deconvolution result for the same set of ROIs and DPIs shown in B and E.

# 5.3 Connectivity alterations in gliomas

The study of connectivity alterations in gliomas has developed mainly in the field of structural and functional connectivity.

The SC was investigated with both direct (i.e., tractography based) and indirect (i.e., atlas-based) approaches to quantifying white matter structural disconnections in gliomas[36], while functional connectivity was used to investigate the impact of brain tumors on the cortical synchronization of brain networks measured with resting-state fMRI (resting-state networks) both near the lesion and remotely and to test whether potential changes in resting-state networks correlate with cognitive status[2]. It was also investigated that the brain fluctuates over dynamic states (functional dynamics), not only in stationary ways and that functional dynamics might be valuable biomarkers to better disentangle high-grade gliomas traits[37].

In the literature, there are still no works on direct connectivity and almost nothing on the study of the hemodynamic response at the single-subject level and its relation to metabolic measures, consequently, the analysis and results of this thesis are the first attempts at a broader application.

# 6 Materials and Methods

This section will provide a complete description of the fMRI dataset and acquisition settings. In addition, it will provide an in-depth analysis of preprocessing and methods implemented before applying sparse DCM, and methods used for the analysis of the results. Moreover, some prior assumptions about the application of the sparse algorithm will be clearly explained. Part of the figures presented in this chapter has been generated with MATLAB2022a (MathWorks, Inc.) and Connectome Workbench (version 1.5.0).

## 6.1 Resting-state fMRI dataset

### 6.1.1 Subjects

Pre-surgical data of 12 patients from 25 to 83 years old with *de novo* brain tumors collected at the University Hospital of Padova have been employed in this study. All participants have regularly taken anticonvulsants for the control of epilepsy and corticosteroids. The protocol had been approved by the local Ethics Committee of the University Hospital of Padova and carried out in accordance with the 1964 Helsinki declaration and its later amendments. Informed consent was accepted by all patients[38]. A summary of the main dataset demographical information is reported in Table 6.1

### 6.1.2 rs-fMRI acquisition

Data were acquired on a 3 T Siemens Biograph mMR scanner equipped with a 16-channel head–neck coil. Anatomical imaging included $T_1$-weighted (T1w) 3D magnetization-prepared rapid acquisition gradient-echo (TR = 2400 ms, TE = 3.24 ms, TI = 1000 ms, FA = 8°, FOV = 256 × 256 mm, voxel size = 1 mm × 1 mm × 1 mm) images acquired both before and after contrast agent injection, a 3D $T_2$-weighted image (TR = 3200 ms, TE = 535 ms, FOV = 256 × 256 mm, voxel size = 1 mm × 1 mm × 1 mm), a 3D fluid attenuation inversion recovery (TR = 5000 ms, TE = 284 ms, TI = 1800 ms, FOV = 256 × 256 mm, voxel size = 1 mm × 1 mm × 1 mm) image. In addition, functional imaging comprised rs-fMRI EPI scans (TR = 1260 ms, TE = 30 ms, FA = 68°, FOV = 204 × 204 mm, voxel size = 3 mm × 3 mm × 3 mm, volumes = 750, MBAccFactor = 2, iPAT = 0, phase encoding direction antero-posterior) and two spin echo-EPI acquisitions with reverse phase encoding (TR = 4200 ms, TE = 70 ms, FOV = 204 × 204 mm, voxel size = 3 mm × 3 mm × 3 mm, MBAccFactor = 1) for EPI distortion correction purposes[38].

### 6.1.3 [18F]FDG PET data acquisition and image reconstruction

For each patient [18F]FDG data were simultaneously acquired with MRI data. After the tracer administration, a 60-minutes dynamic PET list mode acquisition was performed. An average dose of 206.5 MBq (range: 145-303 MBq, according to the body mass index) ([18F]FDG) was intravenously administered to each patient. The scanner was calibrated with recommended QA regimes implemented and daily QA pass before clinical use to ensure accuracy and consistency of scanning was maintained.

The dynamic PET images were reconstructed offline using the Siemens e7-tool for Biograph mMR. The image reconstruction pipeline included correction for scatter, dead time, attenuation (due to head and radio-frequency coil), tracer decay and normalization. Reconstruction was performed with Poisson ordered subset expectation maximization (3 iterations and 21 subsets) no spatial smoothing was performed after reconstruction. Patient's head attenuation map was estimated from the individual T1w MPRAGE image as in Izquierdo et al.[39]. A method that, when the study was initiated, was one of the best performing methods for MR-based attenuation correction. The reconstruction matrix size was 256x256x127 and the voxel size 2.8 x 2.8 x 2.0 $mm^3$. The dynamic was reconstructed using the following time grid: 10 x 6 s, 8 x 15 s, 9 x 60 s, 12 x 240 s with a total of 39 reconstructed volumes.

| ONCO_ID | Age | Gender | Tumor site - Hemisphere | Histology |
|---|---|---|---|---|
| 001 | 74 | M | LEFT | Diffuse glioneuronal tumor |
| 002 | 25 | F | LEFT | Oligodendroglioma |
| 003 | 43 | M | LEFT | Glioblastoma |
| 004 | 56 | F | LEFT | Intracranial mesenchymal tumor |
| 005 | 69 | M | LEFT | Glioblastoma |
| 006 | 83 | M | LEFT | N.A. |
| 007 | 67 | F | LEFT | Glioblastoma |

|  |  |  |  |  |
|---|---|---|---|---|
| 008 | 36 | M | Bilateral (>RIGHT) | Glioblastoma |
| 009 | 58 | F | RIGHT | Glioblastoma |
| 010 | 74 | M | Bilateral (>LEFT) | Diffuse large B-cell lymphoma |
| 011 | 83 | F | LEFT | Glioblastoma epitelioid |
| 012 | 42 | M | RIGHT | Glioblastoma |

**Table 6.1. Subjects' description.** The table indicates the age and gender of each subject, specifying the tumor hemisphere and histology.

### 6.1.3 Tumor segmentation

For the MRI perspective, the regions affected by the tumor  can be distinguished in four distinct subareas: the necrosis; the core of the tumor divided into the highly active region (contrast-enhanced tumor core, CET) and the moderately active region (non-contrast-enhanced tumor core, nCET), and the cerebral edema. Globally, this set of areas are called *lesion areas*, whereas the tumor consists in the first three subareas, namely necrosis, CET and nCET.

The aim of this work is to study the functional and hemodynamic behavior of the whole brain in presence of a tumor by excluding areas that are directly affected by it (e.g., necrosis).

Thus a lesion mask was manually delineated, in order to disregard the regions of the brain belonging to the tumor area. This was done by linearly registering the anatomical images of each patient to the patient naïve T1w image with the Advanced Normalization Tools (ANTs,26 v. 2.0.1). Using these images, the lesion mask and the tumor mask were manually drawn through the ITK-SNAP software (http://www.itksnap.org/) by an expert neuroradiologist with more than 5 years of experience. The detailed description of the procedure is out of the scopes of this thesis but can be found in [38].

An example of the obtained mask is provided for two representative patients in Figure 6.1 and Figure 6.2.

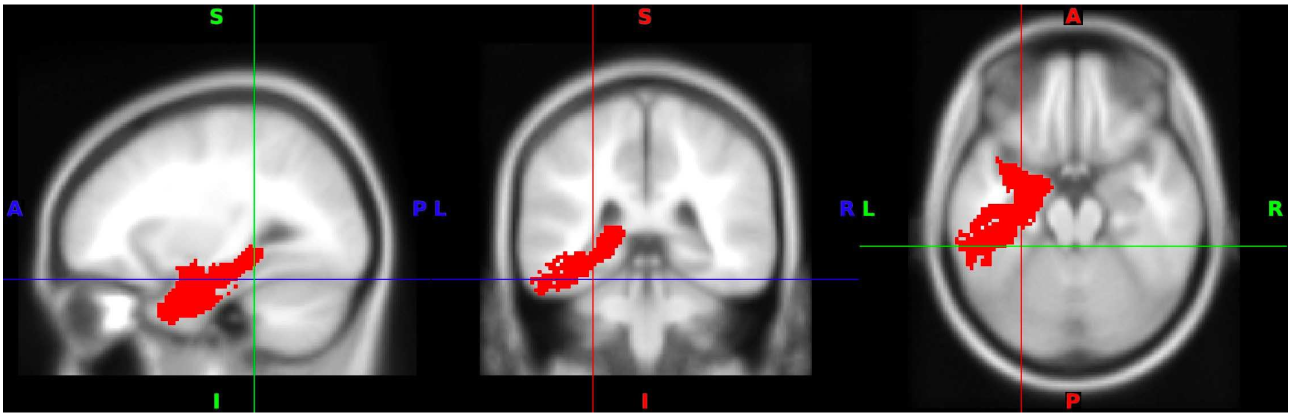

**Figure 6.1. Lesion of subject 1.** The tumor lesion is located in the temporal site lobe of the left hemisphere.

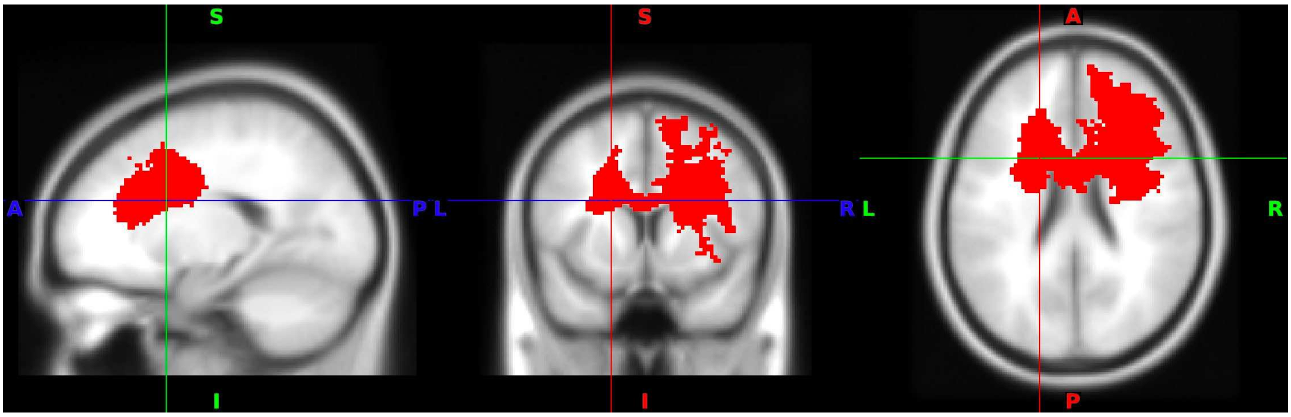

**Figure 6.2. Lesion of subject 8.** The bilateral tumor lesion is located in the frontal and corpus callosum site lobe.

# 6.2 Preprocessing

## 6.2.1 Functional preprocessing and Atlas parcellation

Functional pre-processing of rs-fMRI data included slice timing, readout distortion (FSL's TOPUP) correction, affine realignment of volumes to the central image of the acquisition (FSL's *mcflirt*), a non-linear mapping to the symmetric MNI152 atlas exploiting the subject-specific T1w (via FSL's boundary based registration) and high pass filtering (cut-off frequency: 0.008 Hz). Since the MBfactor of the EPI acquisition sequence differed between the patients and HCs data set, spurious variance related to scanner artifacts was regressed out from the patients' pre-processed data using an ICA-based approach [34]. Thus, the ICs related to sequence MBfactor or broad head movement artifacts were manually identified and regressed out from the original pre-processed data. Then, the first 5 principal components related to CSF and white matter signal were regressed out from rsfMRI timeseries, as well as head-motion parameters and the associated derivatives.

Finally, to quantify the subject-specific head motion during the scan, we computed the frame-wise displacement.

Then, fMRI signals have been projected onto an atlas provided by Schaefer et al.[40]. This functional atlas supplies a surface cortical parcellation by integrating both local gradient and global similarity approaches based on functional connectivity patterns[40]. The parcellations are available at multiple resolutions (100 parcels to 1000 parcels), but the choice fell on the atlas version composed of 100 parcels due to the computational limitations of the sparse DCM model. In fact, increasing the number of regions leads to a relevant rise in the number of parameters to be estimated and in turn to an exponential growth of the computational time required to invert these models[5]. Parcels are organized in 7 cortical large-scale Resting State Networks (RSNs) in (Figure 6.3) and in addition 12 subcortical ROIs have been considered. As a result, each subject-level dataset consists of 112 fMRI timeseries.

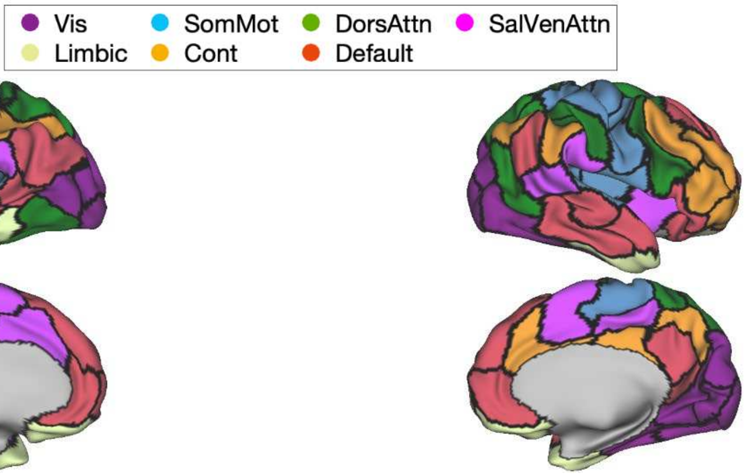

**Figure 6.3. Schaefer 2018 cortical atlas.** 100-area cortical parcellation, the legend corresponds to 7 cortical Resting State Networks (RSNs): *{‘LH Visual’}; {‘LH Somatomotor’}; {‘LH Dorsal Attention’}; {‘LH Salience Ventral Attention}; {‘LH Limbic’}; {‘LH Control}; {‘LH Default’}; {‘RH Visual'}; {‘RH Somatomotor’}; {‘RH Dorsal Attention}; {‘RH Salience Ventral Attention}; {‘RH Limbic’}; {‘RH Control}; {‘RH Default’}.*

## 6.2.2 Despiking and temporal filtering

In order to apply sparse DCM, the input fMRI BOLD signals must be defined over a uniform discrete time grid (TR = 1.26 s). It follows that volume censoring cannot be applied to reduce the effects of motion artifacts. Then the preprocessing method called despiking was applied in order to reduce the contribution of large spikes signals that could deteriorate the accuracy of volume registration and performances of the algorithm[41]. This process truncates and limits the magnitude of large spikes that are usually related to head movements. In Matlab, despiking is performed by means of the function *icatb_despike_tc*, which is included in the Group ICA Toolbox (https://trendscenter.org/software/). The function outputs despiked time courses as well as the indices of time frames that have been replaced (Figure 6.4).

After the despiking step, timeseries have been further filtered in order to reduce the noise outside frequencies of interest. Thus, a band-pass filter has been applied by combining a high-pass and a low-pass filter. Specifically, the timeseries have been temporally filtered with low-pass and high-pass Butterworth filters, keeping frequencies in the band 0.0078-0.2 Hz, to include information related to the hemodynamics (Figure 6.5 and Figure 6.6). The widely used cut-off values are between 0.0078-0.1 Hz, frequently employed in resting state fMRI analysis in order to filter out slow fluctuations and drift brought on by the MRI scanner as well as high frequency artifactual noise (due, for example, to heart pulsation or respiration). In this study, a larger frequency range was employed to retain the range of frequencies that is usually supported by the canonical HRF in the DCM framework[42], [43].

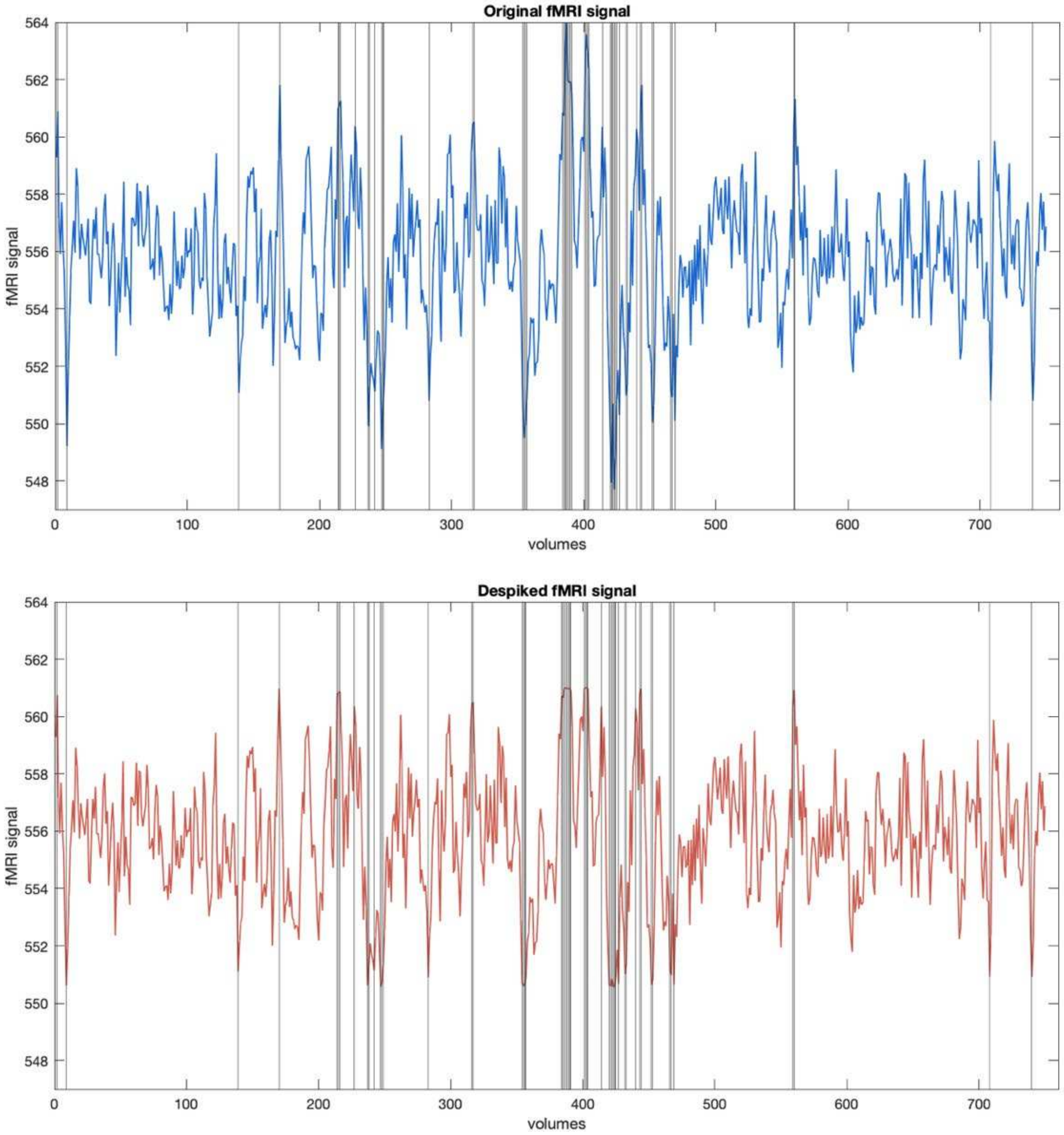

**Figure 6.4. Despiked fMRI signals.** Comparison between the original fMRI timeseries on the upper panel and the despiked timeseries on the lower panel that show smoothed peaks at vertical bands.

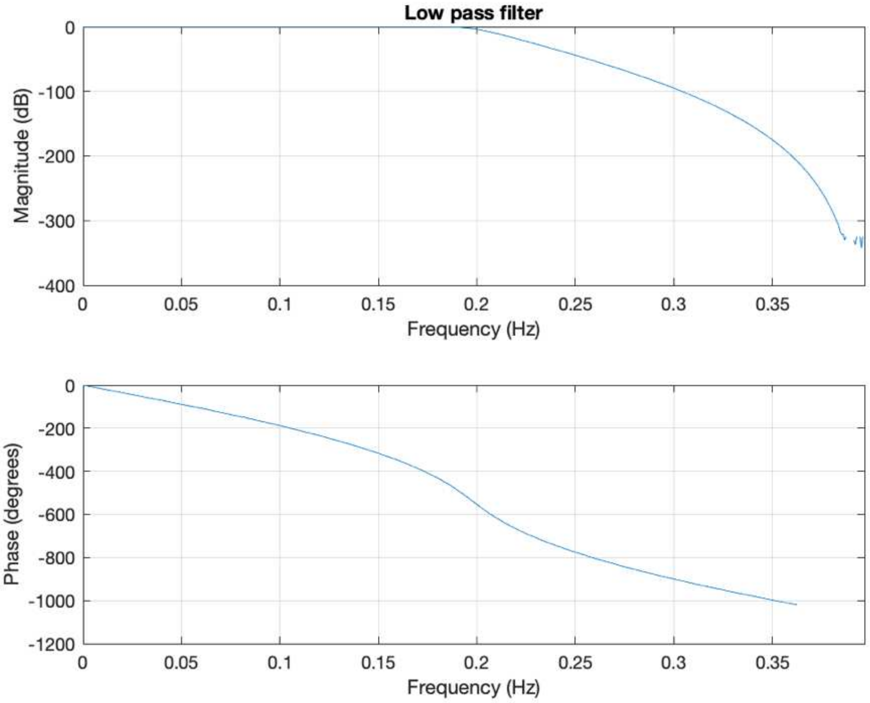

**Figure 6.5. Low pass filter.** Magnitude and phase of the low pass filter applied to fMRI data. The cut-off frequency is 0.2 Hz.

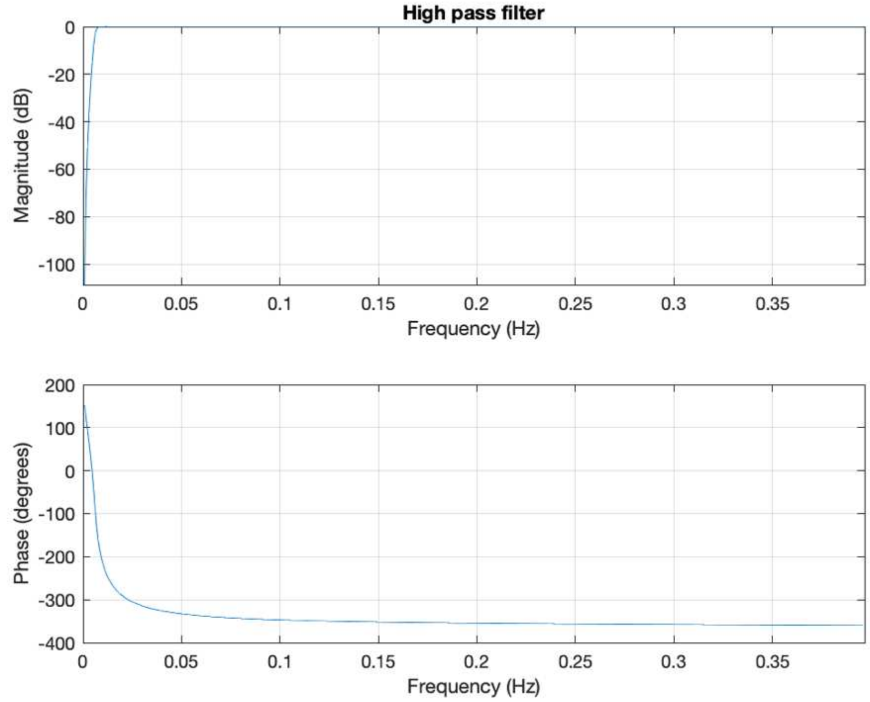

**Figure 6.6. High pass filter.** Magnitude and phase of the high pass filter applied to fMRI data. The cut-off frequency is 0.0078 Hz (1/128 s).

### 6.2.3 Consensus clustering

Before applying sparse DCM, it has been necessary to reduce the total number of nodes considered as inputs, thus the number of samples needed to estimate an arbitrary function with a given level of accuracy grows exponentially with respect to the number of input variables (i.e., dimensionality) of the function. This reduction was made by following the method described by Ryali et al.[44], which proposes a consensus clustering evidence accumulation approach to combine multiple clustering schemes and then cluster brain ROIs through rs-fMRI data. Unlike conventional approaches, CC-EAC can accurately determine the optimal number of stable clusters in rs-fMRI data and is robust to initialization and choice of free parameters[44]. The framework is based on a combination of a base K-means clustering (KC) and hierarchical clustering (HC).

Conversely, this clustering method was not applied to the number of subcortical AAL3 parcels, which remained unchanged. Compared to the method proposed by Ryali et al., there are some differences: the modified silhouette was used as the objective criteria for determining the number of clusters; clustering was only performed on ROIs that were functionally homogeneous (i.e. belonging to the same RSN) and also spatially contiguous in order to preserve the spatial consistency of the hemodynamic properties.

Initially, our rs-fMRI data were registered to the *Schaefer 100* 3D reference space; after the implementation of the consensus clustering framework, data were projected to a reduced space consisting of 62 cortical regions, which was named as *Schaefer 62* space (Figure 6.7).

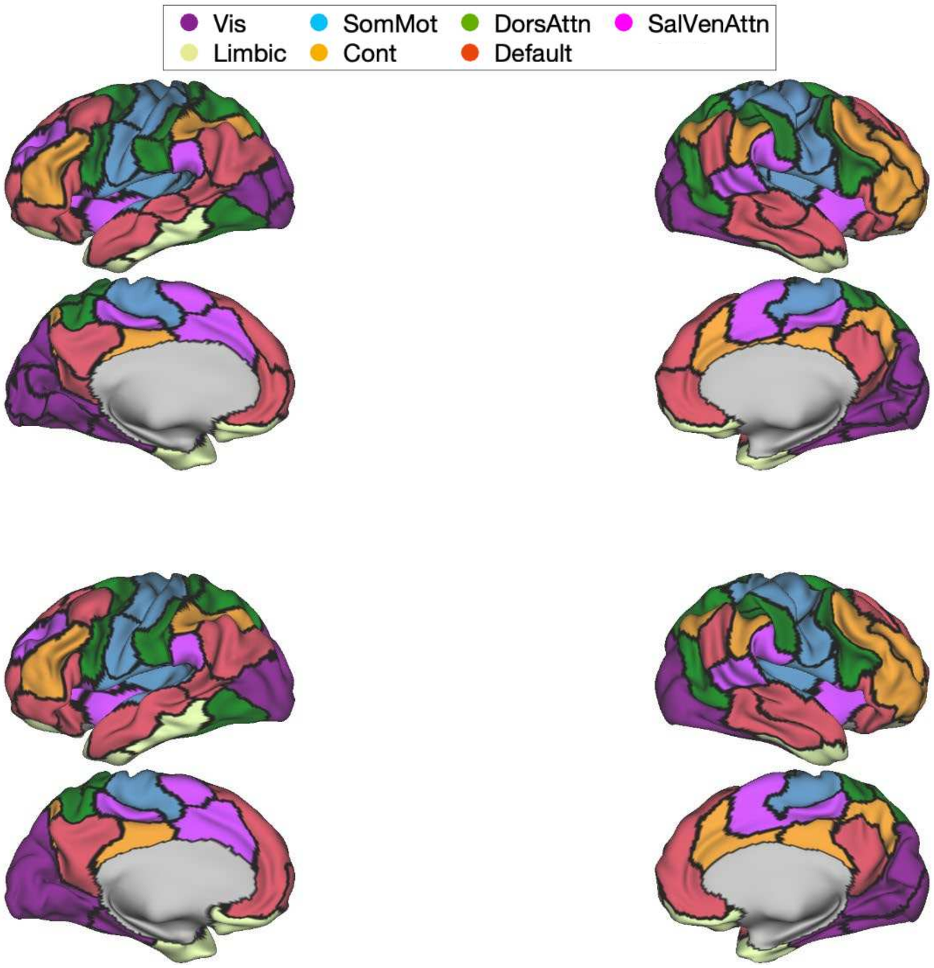

**Figure 6.7. Schaefer 100 and Schaefer 62.** Above, 3D visualization of the *Schaefer100* and below, *Schaefer62* parcellation, after the application of CC-EAC method[27].

# 6.3 Sparse DCM setup

## 6.3.1 Noise variance

Before applying sparse DCM, a parameter that must be set is the so-called noise variance, introduced in section 4.1. This value corresponds to the variance of the measurement noise, which is encoded in the R matrix in sDCM framework. To choose the optimal value, the procedure consisted in trying various weights for the *R* matrix (in terms of a fraction of the sample variance of the input BOLD signal) and finding a trade-off between empirical-simulated FC correlation (eFC-sFC factor) and Kolmogorov-Smirnov (KS) distance, as implemented in Deco et al.[45].

The calculation of the eFC-sFC factor is computed by considering the ground static Functional Connectivity (FC) matrix, defined as the matrix of correlations between each pair of BOLD signals

extracted from brain areas over the whole-time window of acquisition[45]. This matrix is symmetric, with correlation values in the range [-1, +1] and size *brain_areas x brain_areas*.
The eFC-sFC correlation factor is then calculated as the Pearson correlation between the upper triangular part of the empirical FC matrix, computed from the empirical BOLD signal, and the simulated FC matrix obtained from BOLD signals simulated through sDCM estimation (Figure 6.8). This data is obtained as a simulated time response of a dynamic system to arbitrary inputs, as described by the system matrices computed through the sparse estimation algorithm[5].

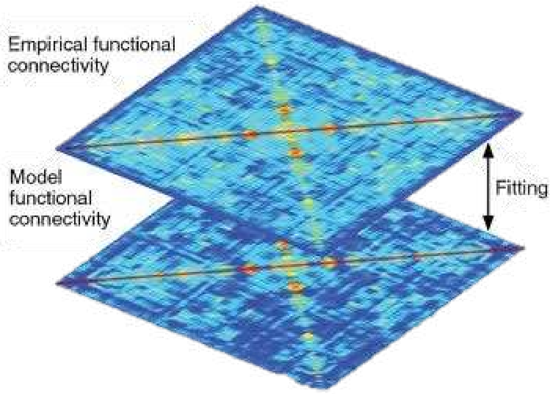

**Figure 6.8. eFC-sFC correlation factor.** The empirical FC was measured using observed fMRI BOLD activity, while the Model FC was obtained through the simulated data; the similarity of matrices is estimated by computing the Pearson correlation[46].

Before describing the choice of the optimal noise variance, the concept of Dynamic Functional Connectivity (FCD) must be introduced; in fact, the setting procedure cannot be performed only with static information, but the evolution and dynamics of the signal over time should be considered in order to provide an optimal value of this parameter.
As highlighted in Deco et al.[45], the estimation of the FCD matrix is required to characterize the time-dependent structure of resting-state fluctuations. As illustrated in Lurie et al.[47], there are many methods to estimate the FCD matrix from fMRI data. However, the sliding window approach is the most commonly used. In this view, the full-length BOLD signal is split up into a number of sliding windows of 10 seconds, overlapped by 5 seconds for each sliding window centered at time *t*, each regarding the computation of a separate FC matrix, FC(t). The FCD matrix (*number of sliding windows x number of sliding windows*) is symmetric and each (t1,t2) entry is defined by the Pearson correlation between the upper triangular part of the two matrices FC(t1) and FC(t2).

The upper triangular elements of the FCD matrices over all subjects and sessions are compared by generating their distribution and computing the Kolmogorov-Smirnov (KS) distance between the simulated and empirical data. The KS distance quantifies the maximal difference between the cumulative distribution functions of the two samples.

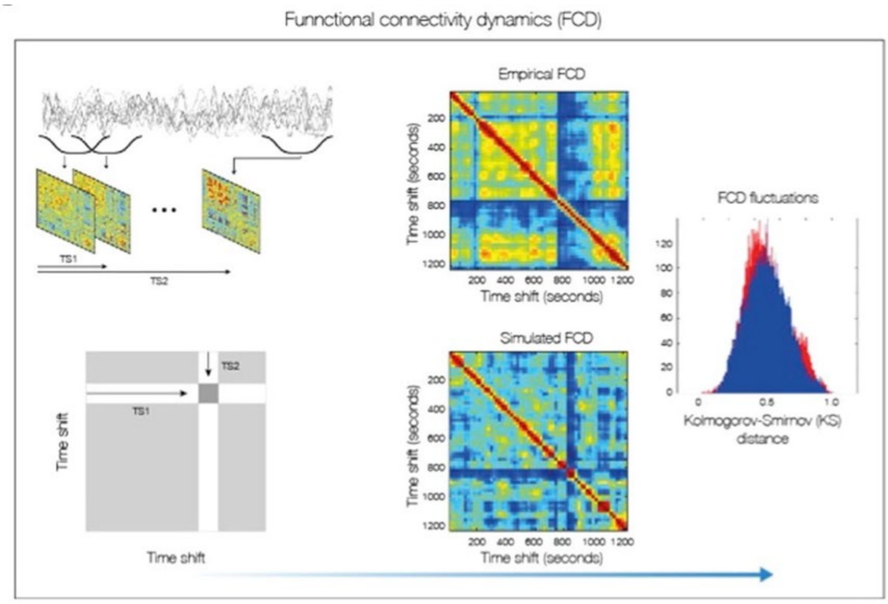

**Figure 6.9. Sliding windows approach and KS distance.** The sliding window approach is applied to fMRI BOLD signals; then the KD distance is calculated between the empirical and simulated FCD distribution[45].

Consequently, our objective of finding the optimal value of the noise variance results in finding the value that maximizes the correlation between empirical and simulated FC and minimizes the KS distance (see Results). This procedure is subject-specific and the value most frequently good in all subjects was chosen.

## 6.3.2 Setting of the hemodynamic prior

As largely described in Chapter 4, the hemodynamic response function of a patient affected by glioma is expected to be more variable and characterized by abnormal vascular properties. Indeed, the presence of glioma in the brain can induce metabolic and hemodynamic alterations that should be taken into consideration when the prior hemodynamic response function of sparse DCM is set. Unfortunately, to the best of our knowledge, there are not many research insights about the characterization of the whole-brain human hemodynamic response in presence of brain glioma. As a result, we focused on studies performed *in vivo* on mice to extract some meaningful information about the hemodynamic alterations induced by brain tumors[35].

Relying on the analysis of the hemodynamic alterations described in Montgomery et al.[35], we expected that the hemodynamic response function in oncological patients would be characterized by some peculiar properties, such as:

- Amplitude decrease
- Attenuation of the post-stimulus undershoot
- Increase of the Time To Peak
- Flatter shape of the response, hence a higher Mean Transit Time and FWHM

Consequently, the variance scale of the prior HRF was modified by taking into consideration all those evaluations and assumptions (see Results).

# 6.4 Estimation of the tumor overlap

As explained before, the fMRI analysis has been performed by excluding brain voxels included in the lesion volume (tumor mask). Thereby, some brain parcels, which will be named as overlapping ROIs in the following, are characterized by a partial intersection with the glioma and are then expected to surround the tumor lesion (whose core always affects white matter bundles nearby), while apparently unaffected ROIs will be encoded as pseudo-normal areas. In order to quantify the degree of overlapping, the tumor mask of each subject has been dilated through a spherical element of radius 2 thus accounting for minimal overlaps. Then, the percentage of voxels intersecting the tumor was calculated as the ratio between the *Schaefer62* number of voxels overlapping the dilated tumor mask and the total number of voxels in each parcel. These percentage values have been saved into a *n_parcels x n_subjects* matrix named as the tumor overlapping matrix (see Results).

# 6.5 Relationship between HRF parameters and [18F]FDG PET microparameters

## 6.5.1 HRF parameters

The hemodynamic response can be effectively investigated and described by some parameters that can be obtained by the visual description of the HRF. As described in the work by West et al.[48], some meaningful parameters can be extracted from the HRF curves to quantitatively describe the vascular heterogeneity of the brain (Figure 6.10).

The fundamental parameters which describe alterations or differences between several HRFs are:

- Time to Peak
- Time to Trough
- Rise Slope
- Peak Amplitude
- Fall Slope
- FWHM
- Peak to Trough
- Trough Amplitude
- Area Under the Curve (AUC)

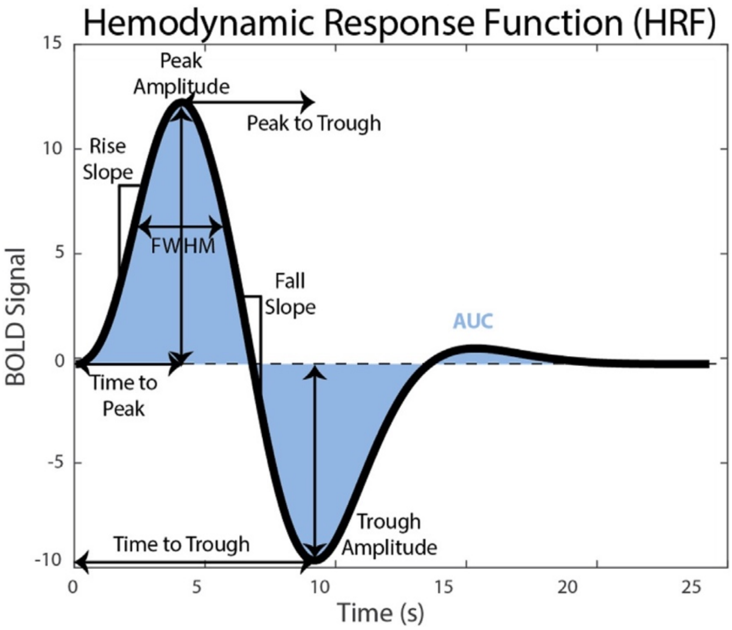

**Figure 6.10: Hemodynamic response function parameters.** Figure of the parameters of the hemodynamic response function: Time to Peak, Time to Trough, Rise Slope, Peak Amplitude, Fall Slope, FWHM, Peak to Trough, Trough Amplitude and Area Under the Curve (AUC)[48].

## 6.5.2 [18F]FDG PET microparameters

The tumor overlapping matrix could be useful to discriminate regions with a pseudo-normal behavior from those surrounding the tumor. As a result, also differences at a metabolic level are expected to be found, as well as hemodynamic and connectivity alterations.

[18F]FDG PET microparameters were estimated by the group of Professor Bertoldo exploiting the well-known 3K compartmental model described in section 1.2. In brief, as suggested in Zanotti-Fregonara et al.[49], the model input function was directly extracted from common carotid, a large

vessel included in the field of view of the dynamic PET images. The extracted raw signal was fitted using the modified Feng's three exponential model[50]. The model prediction of the fitted image derived input function was employed as nose-free arterial input of the model. The presence of radiometabolites do not affect the [18F]FDG tracer[49], therefore, no additional hypothesis or processing was required. Finally, the compartmental model parameters were estimated at voxel level using the weighted variational bayesian approach as described in Castellaro et al.[51].
PET microparameter maps have been used in particular to obtain both metabolic information (k3) and a proxy of cerebral blood flow (K1). For each patient, PET static images were linearly registered into the T1w naïve space by means of ANTs. Then, applying the inverse of this transformation the *Schaefer62* atlas was mapped into the individual PET space and for each parcel the average K1 and k3 was computed. For each parameter, we thus obtained a *n_parcels x n_subjects* matrix. In the end, those matrices have been z-scored to account for possible bias in the subject-level estimates. To avoid possible biases due to the presence of the tumor, the z-score was computed at the individual level and excluding the parcels with a non-null overlap with the tumor.

The two physiological parameters that have been taken into consideration are:

- K1, namely the delivery from plasma to interstitial-intracellular space (Figure 6.11)
- k3, namely the phosphorylation rate (Figure 6.12)

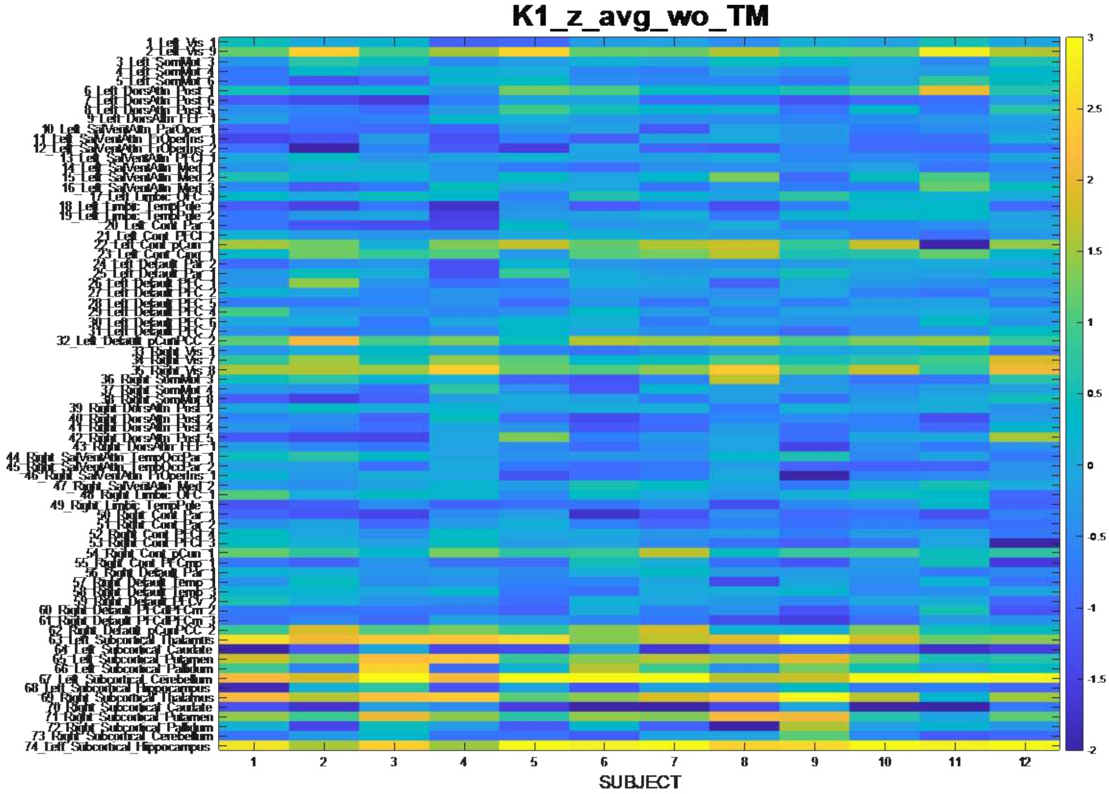

**Figure 6.11. K1 map.** Matrix representation of the K1 PET parameters for each subject in each cortical and subcortical ROI, after being averaged and z-scored, the parcels considered are without those of the tumor mask.

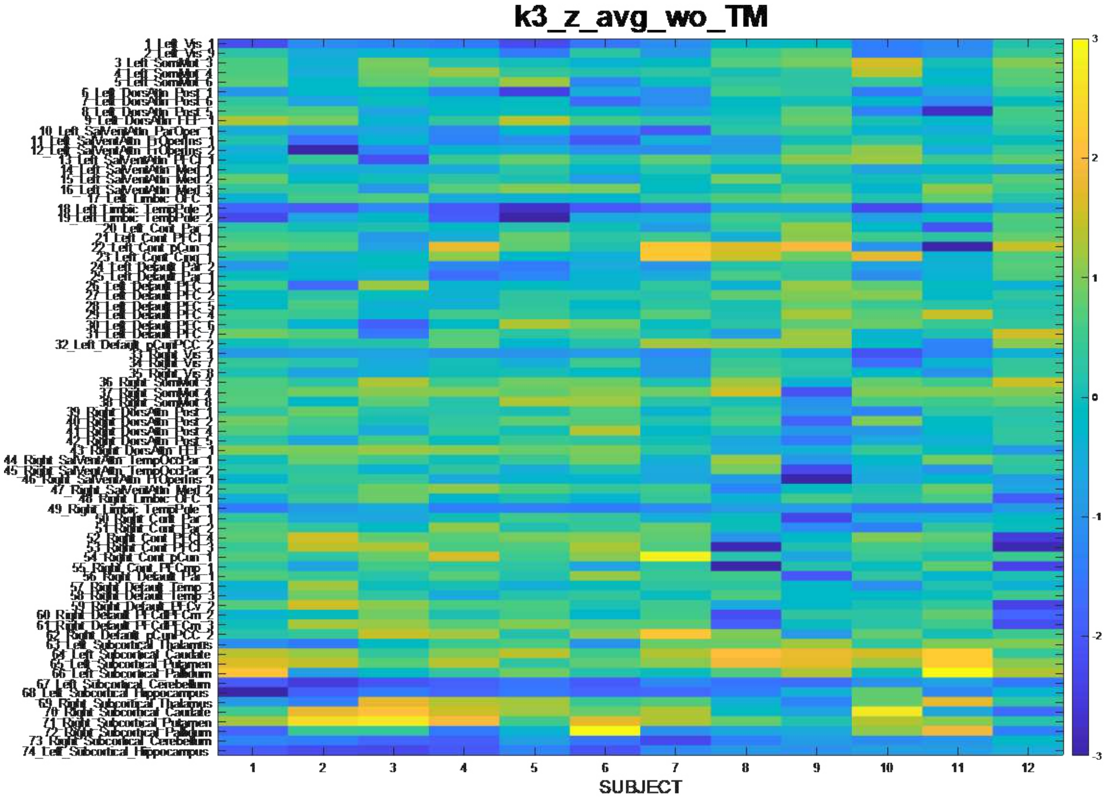

**Figure 6.12. k3 map.** Matrix representation of the k3 PET parameters for each subject in each cortical and subcortical ROI, after being averaged and z-scored, the parcels considered are without those of the tumor mask.

### 6.5.3 Classes creation and relationship with z-scored K1 and k3

After the computation of the binarized tumor overlap matrix, the overlapping regions were classified by comparing the selected parameter value with respect to the pseudonormal median value. This classification was performed by evaluating each pair of HRF parameters, i.e., *amplitude* and *FWHM.* In that specific example, each overlapping ROI has been classified in Class 1 if the *amplitude* value of the HRF in that parcel was higher than the median *amplitude* value of the pseudonormal ROIs, and if the *FWHM* value of the HRF in that parcel was higher than the median *FWHM* value of the pseudonormal ROIs. For Class 2 the combination was: higher for the first parameter and lower for the second, Class 3 lower for the first parameter and higher for the second, and Class 4 lower for the first parameter and lower for the second.

The values of PET microparameters K1 and k3 were plotted into boxplots by following the classification above. To find significant differences, a test on the two sample distribution variance, namely an *anova* statistical analysis was performed, and after correcting for multiple comparisons, differences between pairs of classes were obtained.

# 6.6 Effective Connectivity and Gradients

## 6.6.1 Graph theory

The sparse EC matrix has been divided into four sub-matrices in order to acquire information about the left, right, right-to-left, and left-to-right connections. For example, the intra-left hemisphere connections are all the values inside the sub-matrix that start in the left hemisphere and arrive in the same (Figure 6.13). The same was performed for the matrix without the subcortical regions.

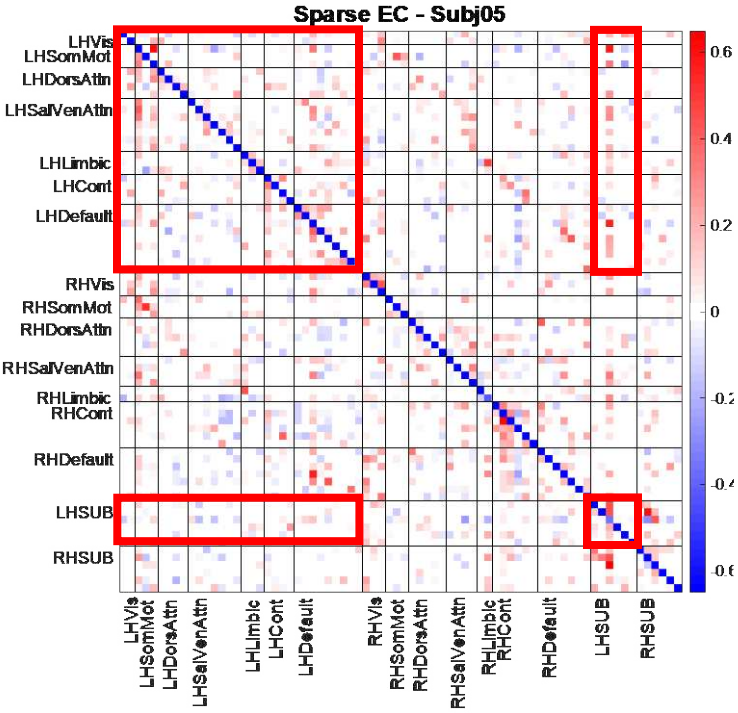

**Figure 6.13. Connections in EC matrix.** The figure shows an example of the sub-matrix of intra-left hemisphere connections, by considering subcortical regions.

## 6.6.2 Gradients

The computation of effective connectivity gradients was done using BrainSpace v0.2.1 toolbox, a compact and flexible toolbox that implements various approaches to build macroscale gradients from neuroimaging and connectome data[27].

The EC matrix is asymmetric, therefore it was necessary to make a distinction between incoming (row features, $EC_{in}$) and outgoing (column features, $EC_{out}$) links.

Specifically, the gradient maps were constructed through the *GradientMaps* object. The toolbox allows the implementation of many different kernels and dimensionality reduction techniques. In this case, the selected parameter setting for gradient calculation was defined as follows:

- Affinity computation: gaussian kernel (g=1/n_features)
- Embedding approach: Laplacian eigenmaps
- Alignment: procrusters alignment to the reference space (obtained by computing gradients on the concatenated EC matrix extracted from 12 healthy controls from the LEMON public dataset[52]).

This procedure was performed for both subject-level incoming EC and outgoing EC links, with the sparsity of input matrices set to 0, since the matrices have been already sparsified.

To choose how many gradient components to retain, it may be interesting to look at each component's lambda (eigenvalues of the Laplacian). In laplacian mapping, the lowest eigenvalues are the most important since they denote the main spectral partitions in the graph.

Since inspecting gradients together can be quite informative, the BrainSpace toolbox provides tools for plotting a set of gradients in 2D or 3D space and assigning them colors based on their position. This color can then be propagated to the surface to get an idea of the multidimensional interaction between the gradients (Figure 6.14).

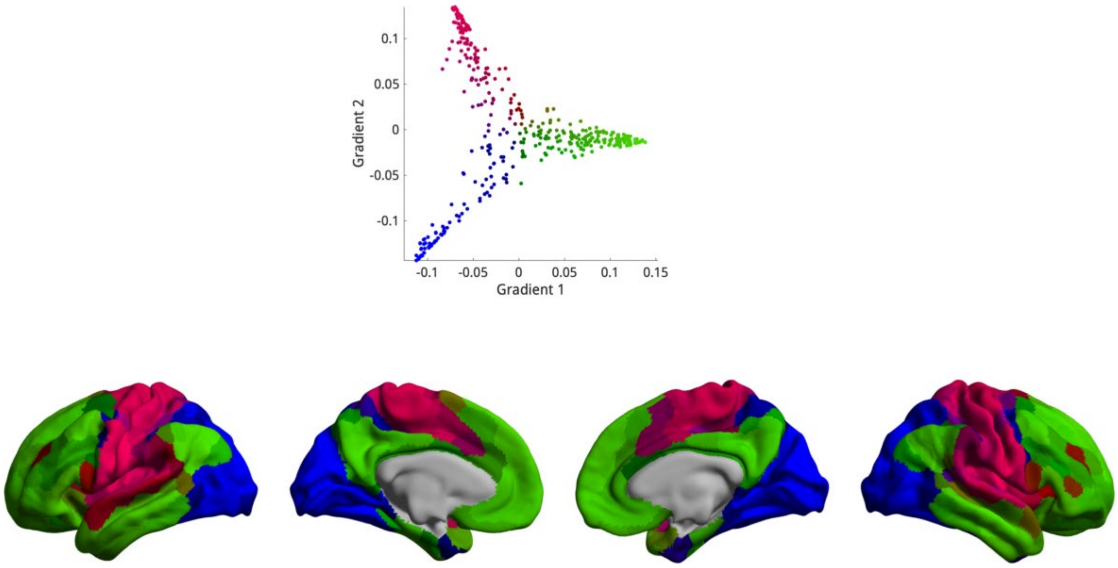

**Figure 6.14. 2D and 3D representations of Gradient 1 and Gradient 2.** Above 2D visualization through *gradient_in_euclidean* function of the first two gradients, below the surface representation with three colors of regions corresponding in the figure above. It is quite evident that the three lines in the scatter plot mostly correspond to the somatomotor (red), default mode (green), and visual (blue) networks [27]

The following analyses were performed considering the Gradient 1 and Gradient 2 distribution space. First of all, the silhouette coefficient for each overlapping ROI was computed, by considering the 7 networks as clusters. That result gives information about how a specific parcel is similar to its own cluster (cohesion), compared to other clusters (separation). These values were plotted through boxplots both at the group level and single-subject level, in order to find some significant differences (see Results). Statistically significant differences on medians were obtained thanks to a Wilcoxon rank sum test.

A subsequent analysis regarded the computation of the Euclidean distance for each parcel, comparing the values from the incoming and outgoing links with the control ones. As before, the analysis was performed for both group level and single-subject level, highlighting significant differences through a Wilcoxon rank sum test on medians.

# 7 Results

This chapter will explain the results of sparse DCM setup and the results of analyses after its application.

Specifically, only relevant figures and graphs will be included, leaving aside secondary results that will not be extensively discussed in the following. All quantitative measures have been obtained with MATLAB2022a (MathWorks, Inc.), while figures have been generated with MATLAB2022a, BrainSpace v0.2.1 Toolbox and Connectome Workbench (version 1.5.0).

## 7.1 Sparse DCM setup

As explained in Materials and Methods, before applying sparse DCM it was necessary to set the following parameters:

- Covariance matrix R, which indicates the input observation noise.
- Prior hemodynamic response, by taking into account the considerations explained in Materials and Methods.

### 7.1.1 Optimal noise variance

As previously explained in section 6.3.1, the choice for the best weight of the noise variance matrix R was performed by calculating the empirical-simulated FC correlation (Figure 7.1) and the empirical-simulated FCD Kolmogorov-Smirnov (KS) distance (Figure 7.2) by taking into consideration five reference subjects (see Table 6.1): 001, 002, 003, 004, and 005.

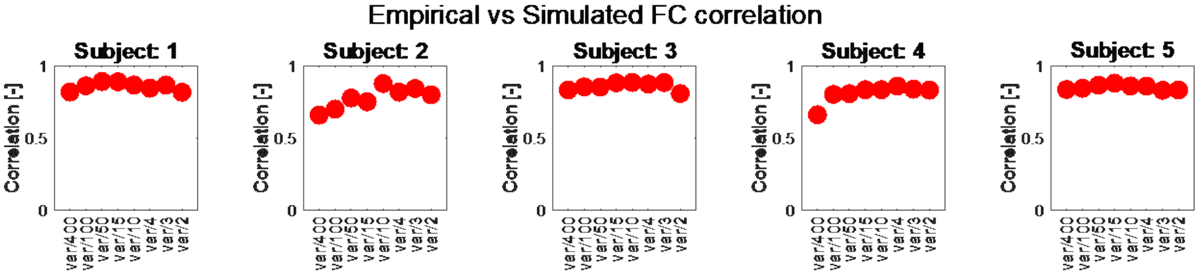

**Figure 7.1. Empirical-simulated FC correlation.** FC Pearson correlation values for each of the five subjects, by calculating the Pearson correlation through the empirical FC matrix and the simulated one. The eFC-sFC factor has been computed for eight weights of the noise variance: 1/400, 1/100, 1/50, 1/15, 1/10, 1/4, 1/3, and 1/2. This factor should be maximized.

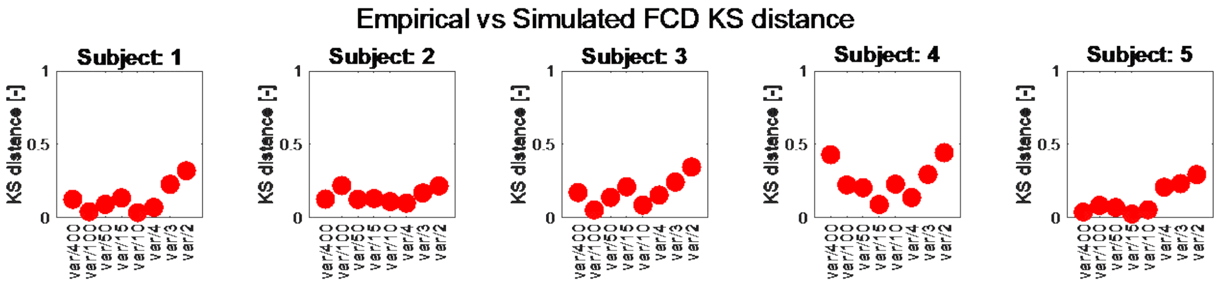

**Figure 7.2. Empirical-simulated FCD KS distance.** Kolmogorov-Smirnov distance FCD distribution for each of the five subjects, by calculating the KS distance through the empirical and simulated FCD distribution values. This distance has been computed for eight weights of the noise variance: 1/400, 1/100, 1/50, 1/15, 1/10, 1/4, 1/3, and 1/2. This factor should be minimized.

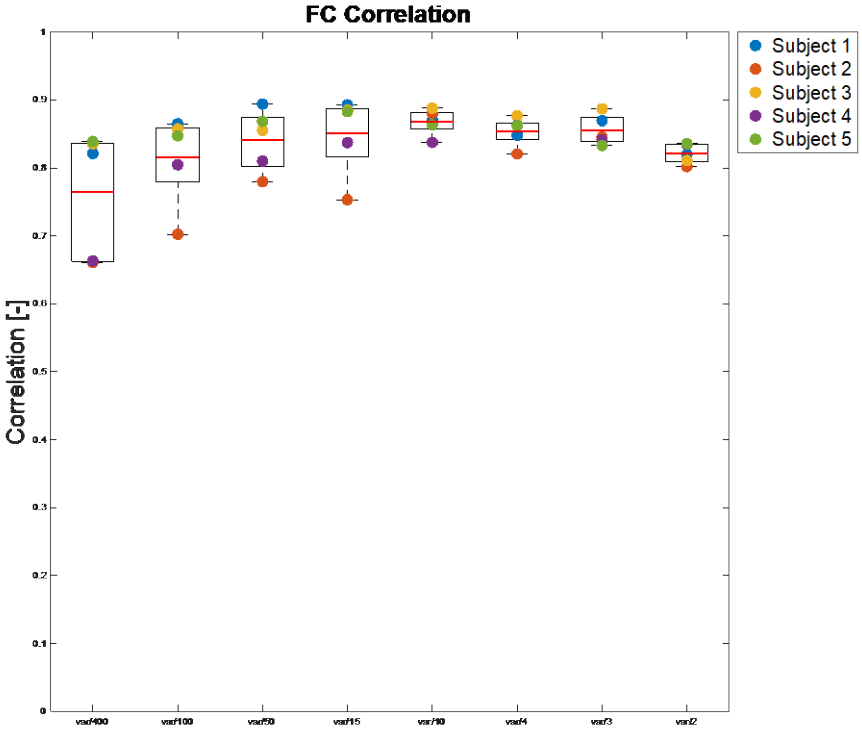

**Figure 7.3. Empirical-simulated FC correlation through subjects.** Visualization of the FC correlation values through subjects for each weight of the noise variance. The mean values across subjects are highlighted in boxplots with red lines.

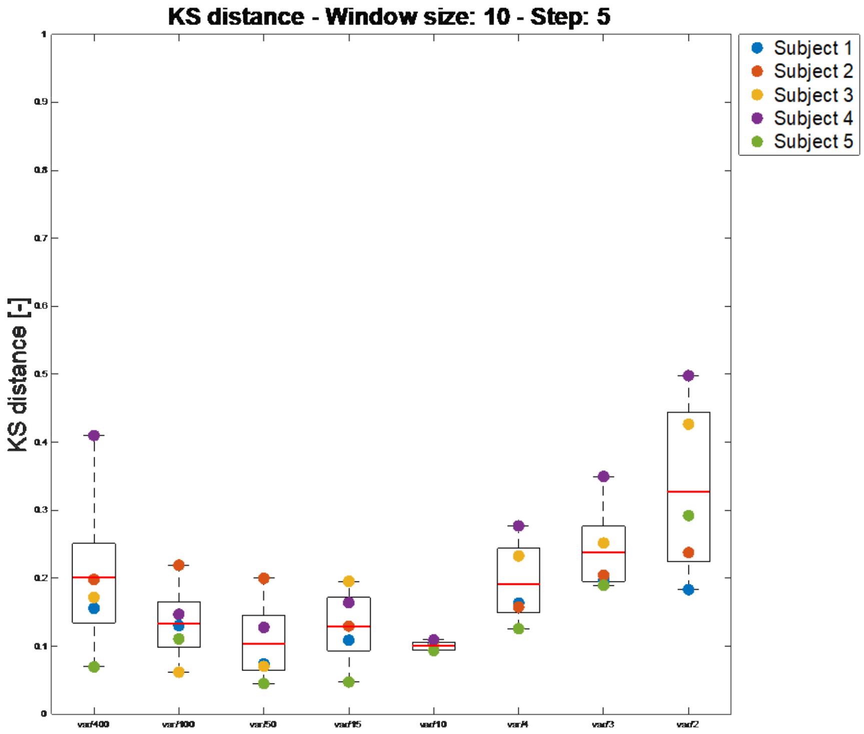

**Figure 7.4. Empirical-simulated FCD KD distance through subjects.** Visualization of the KS distance values through subjects for each weight of the noise variance, by setting the parameters of the sliding window approach (window size=10s and step=5s). The mean values across subjects are highlighted in boxplots with red lines.

## 7.1.2 Hemodynamic prior

The following figures show the variations in Balloon model parameters, and how these variations affect the shape of the hemodynamic response function. The final figure shows the shape of the hemodynamic prior.

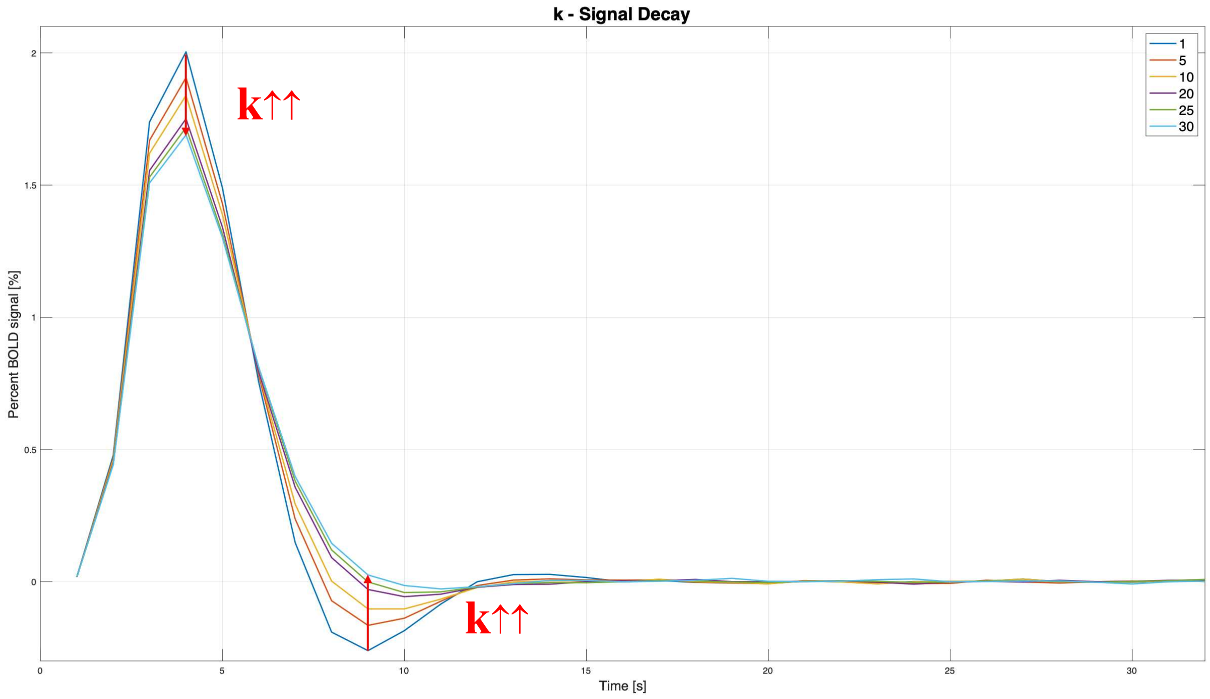

**Figure 7.5. Variation of HRF as the parameter k changes.** The figure shows the variation of the HRF when there is a change in the variance scale of the Balloon model parameter k (Signal Decay). As indicated by red arrows, as the variance scale value increases, the response is less wide and the undershoot less evident.

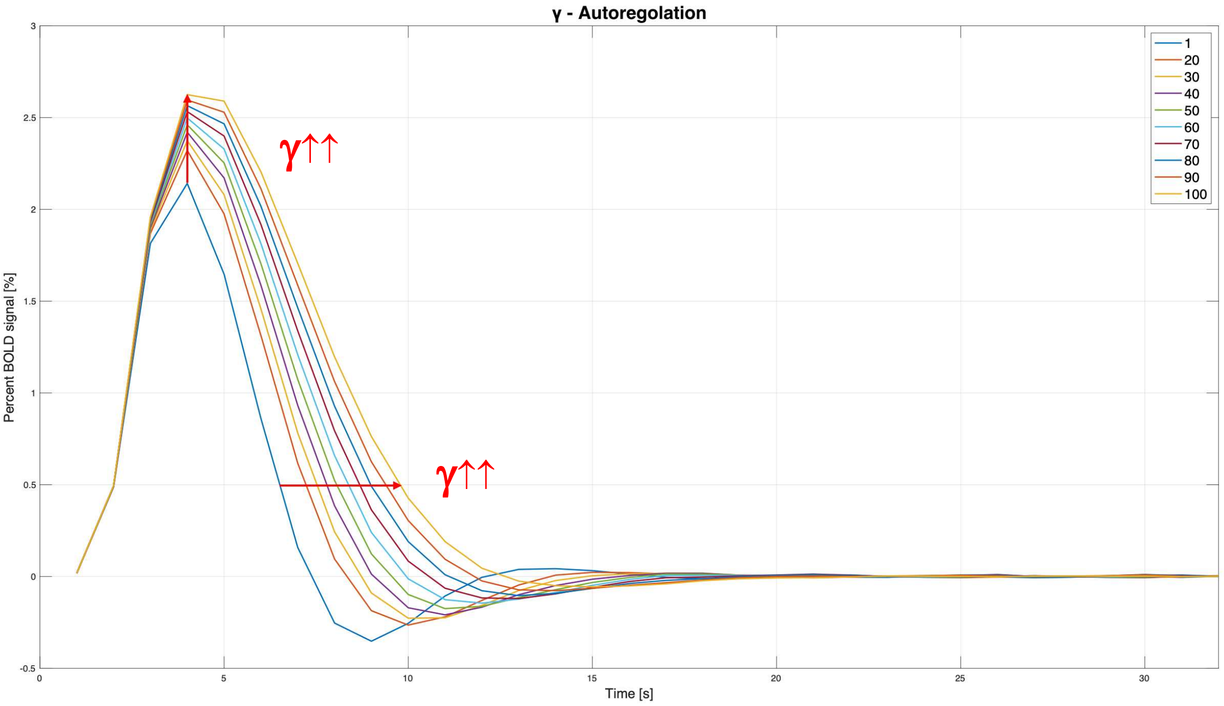

**Figure 7.6. Variation of HRF as the parameter g changes.** The figure shows the variation of the HRF when there is a change in the variance scale of the Balloon model parameter g (Autoregolation). As indicated by red arrows, as the variance scale value increases, the response is wider, the undershoot less evident, and there is a delay in the HRF.

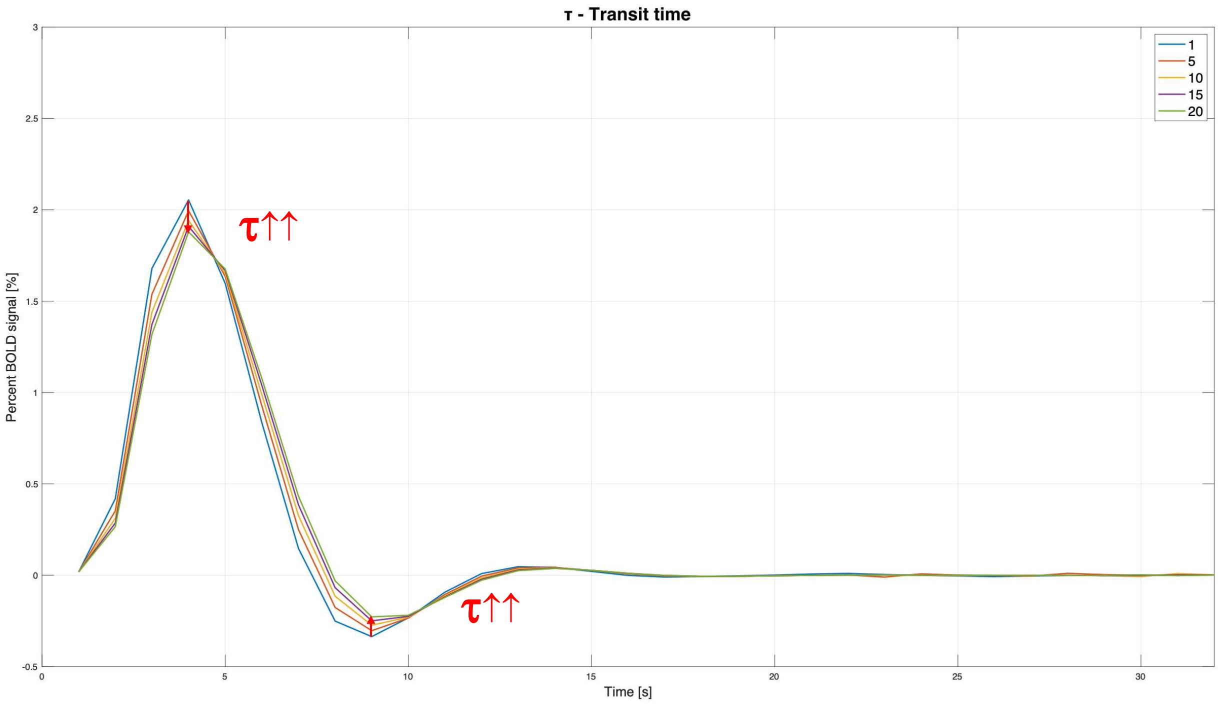

**Figure 7.7. Variation of HRF as the parameter t changes.** The figure shows the variation of the HRF when there is a change in the variance scale of the Balloon model parameter t (Transit Time). As indicated by red arrows, as the variance scale value increases, the response is less wide and the undershoot less evident, although the variation is less pronounced than in the previous parameters.

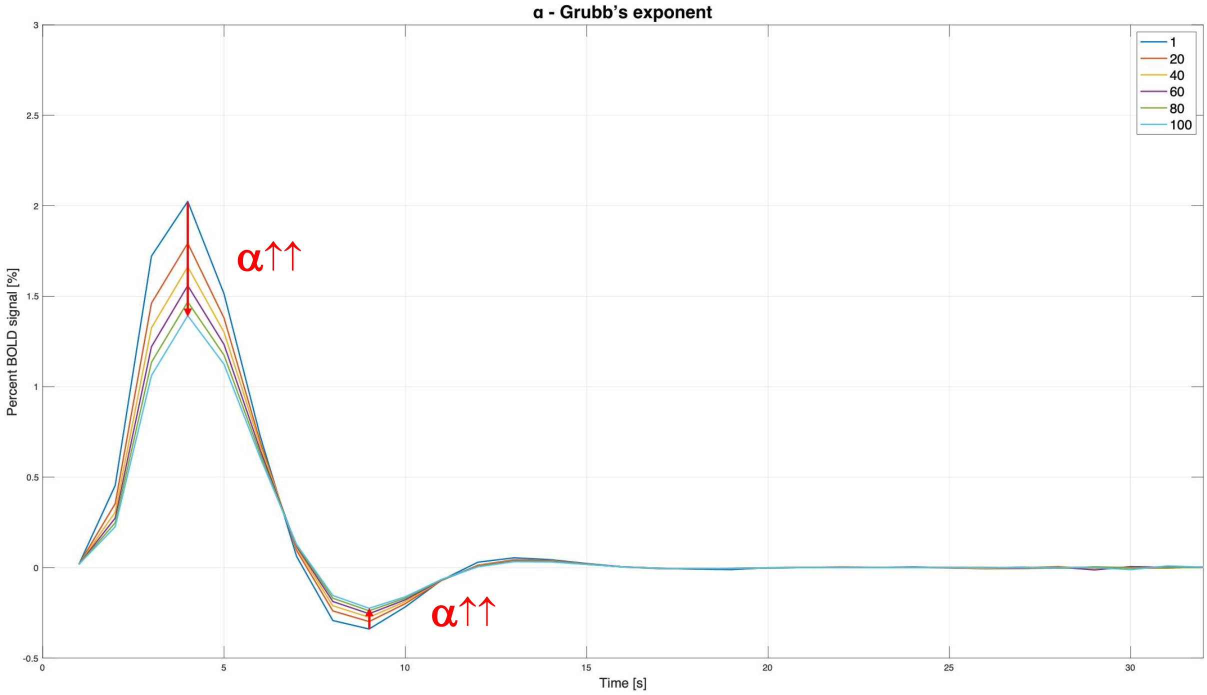

**Figure 7.8. Variation of HRF as the parameter a changes.** The figure shows the variation of the HRF when there is a change in the variance scale of the Balloon model parameter a (Grubb's exponent). As indicated by red arrows, as the variance scale value increases, the response is less wide and the undershoot less evident.

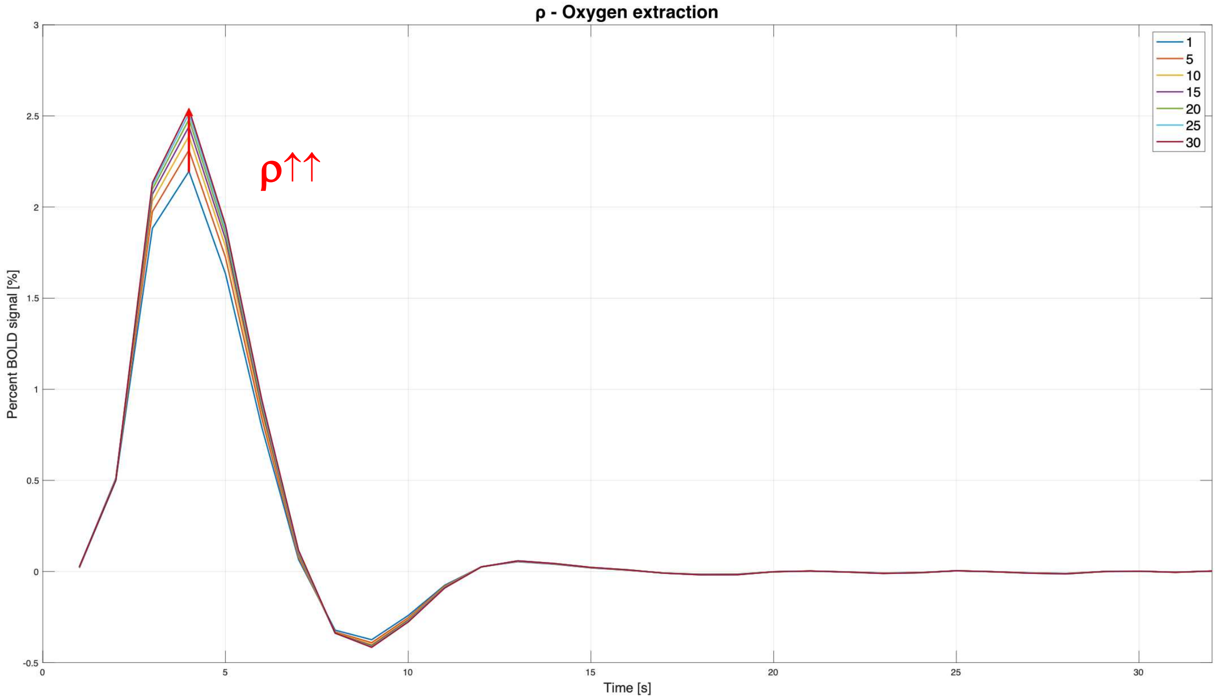

**Figure 7.9. Variation of HRF as the parameter r changes.** The figure shows the variation of the HRF when there is a change in the variance scale of the Balloon model parameter r (Oxygen extraction). As indicated by red arrows, as the variance scale value increases, the response is wider.

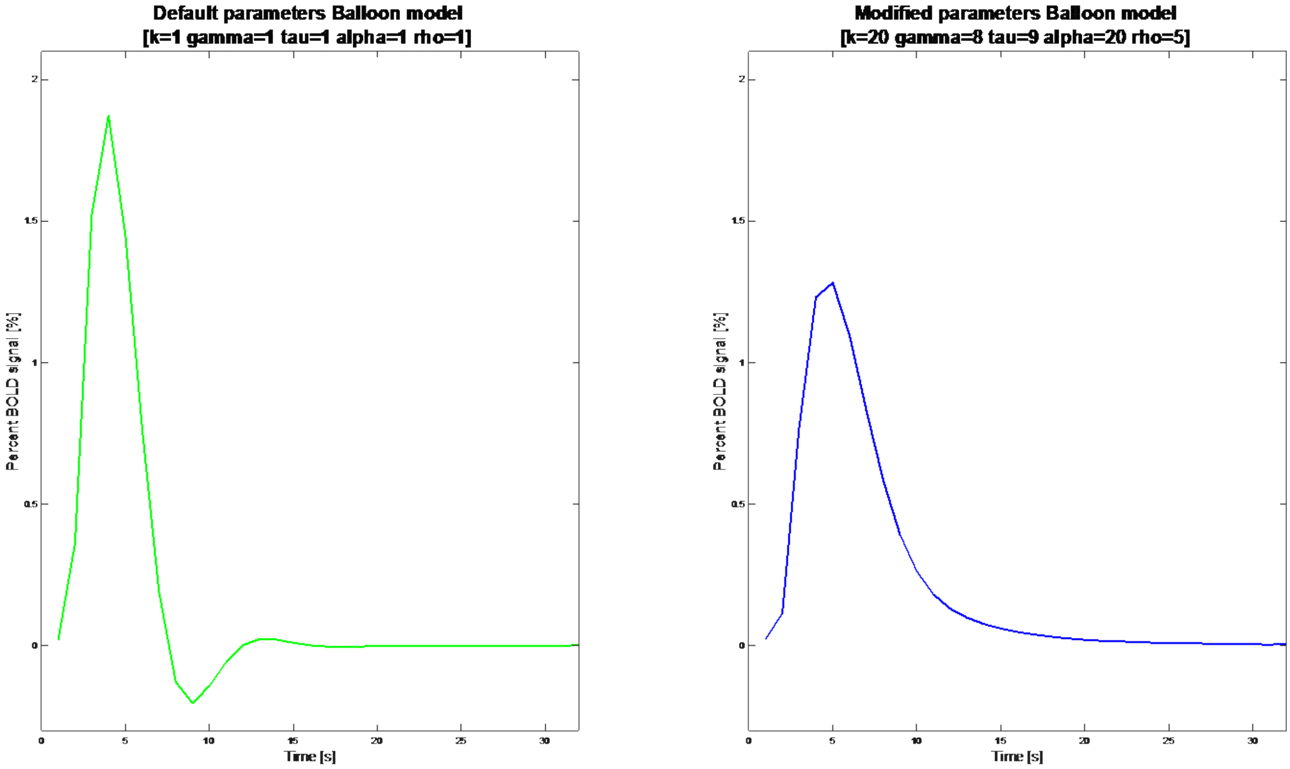

**Figure 7.10. Ideal hemodynamic response for the default set parameters and brain tumor subjects.** The figures depict the ideal mean and std hemodynamic responses of the default set parameters and the modified parameters describing brain tumor subjects. The hemodynamic response was derived through the Balloon model, by setting the variance scales of the parameters as indicated above.

## 7.2 Tumor overlap matrix

The aim of the following analysis was to find a relationship between the PET microparameters (K1 and k3) and the hemodynamic parameters. To find this relation, the overlapping matrix (Figure 7.6) was binarized by evaluating various thresholds (Figures from 7.7 to 7.9).

Figures from 7.7 to 7.9 show a decrease in the number of overlapping parcels, which is expected because of the higher threshold imposed. As a result, opting for higher thresholds is much more conservative and only regions with a high percentage of overlap are retained (Figure 7.10). Consequently, the following analysis will be performed for all thresholds to take this variability into account.

This decrease in the number of overlapping ROIs also evidences the regions more affected by the glioma, e.g. Subject 3 presents overlapping parcels only in the left hemisphere, consistently with the information described in Table 6.1. Conversely, Subject 8 presents a bilateral tumor that involves both left and right regions, such as parcels belonging to the left SalVentAttn network, left subcortical, and most in the right hemisphere.

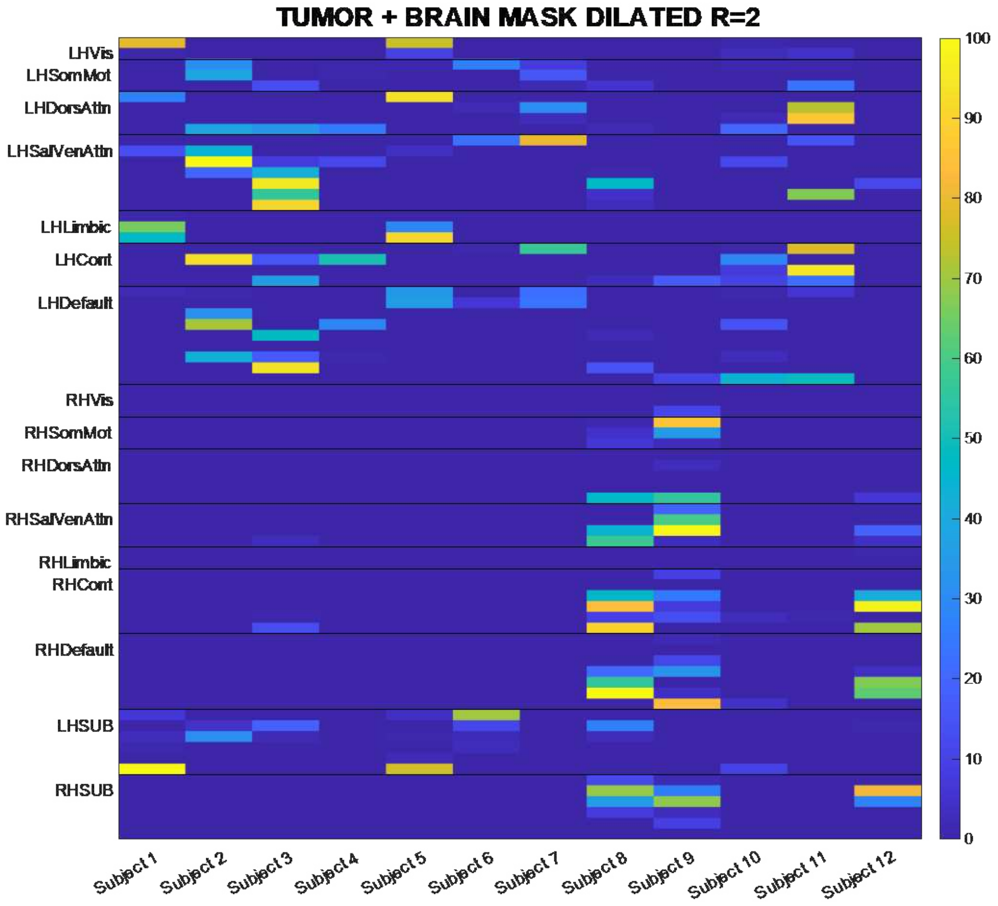

**Figure 7.11. Overlap matrix.** Overlap matrix between the lesion mask (or tumor mask) dilated by a spherical element of radius 2, the single-subject brain mask, and each of the 74 cortical and subcortical parcels. Columns represent the subjects; rows are the regions of the brain, and the figure shows the percent value of overlap.

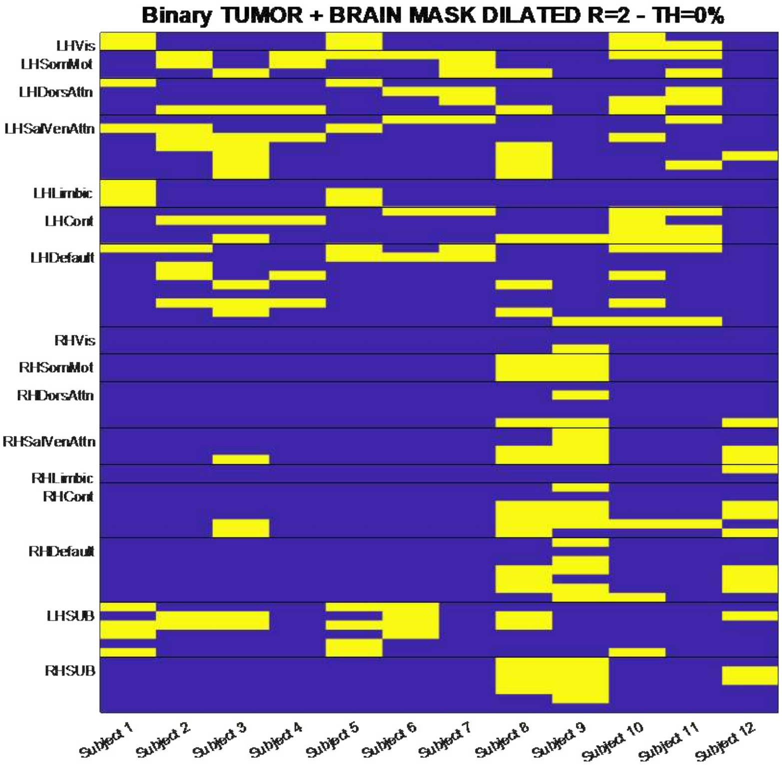

**Figure 7.12. Binary overlap matrix with threshold=0% imposed.** The overlap matrix in Figure 7.6 is binarized by imposing a threshold equal to 0%. In yellow, the brain parcels through subjects with an overlap percentage higher than the threshold.

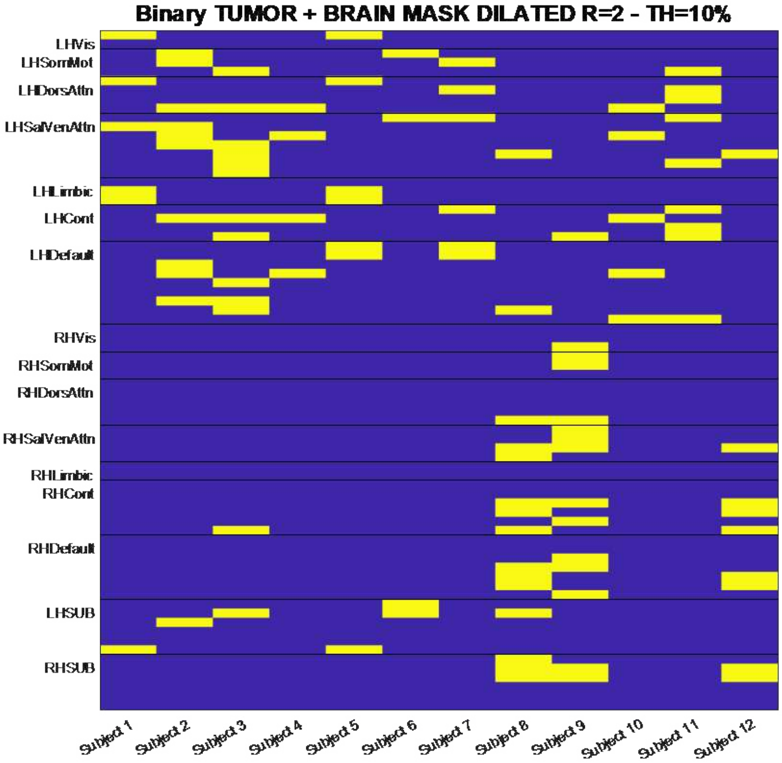

**Figure 7.13. Binary overlap matrix with threshold=10% imposed.** The overlap matrix in Figure 7.6 is binarized by imposing a threshold equal to 10%. In yellow, the brain parcels through subjects with an overlap percentage higher than the threshold.

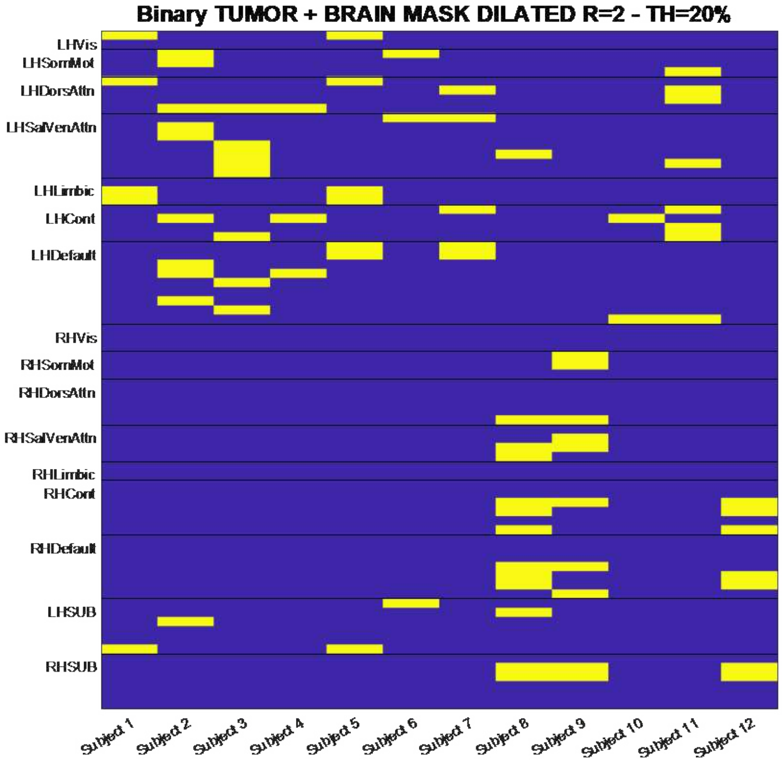

**Figure 7.14. Binary overlap matrix with threshold=20% imposed.** The overlap matrix in Figure 7.6 is binarized by imposing a threshold equal to 20%. In yellow, the brain parcels through subjects with an overlap percentage higher than the threshold.

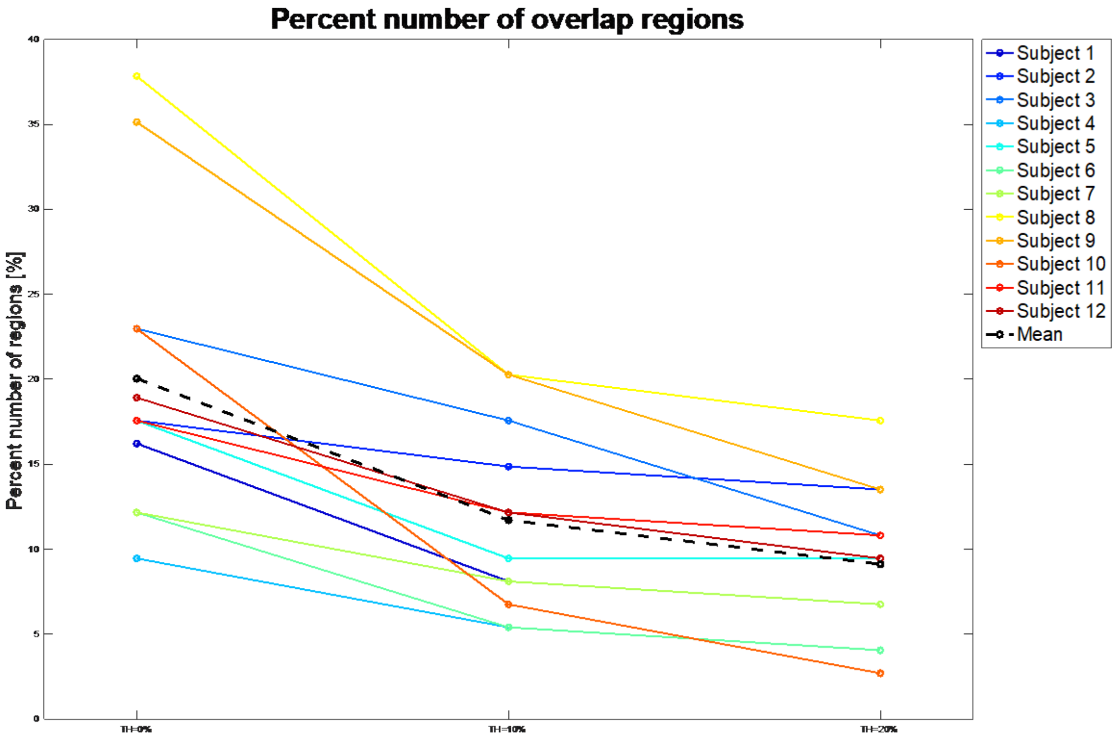

**Figure 7.15. The percent number of overlap regions for three different thresholds.** The figure depicts the percent number of overlap regions for each of the 12 subjects, imposing three different thresholds: 0%, 10%, and 20%. The black dashed line represents the mean of the overlapping regions for the three thresholds: this value decreases as the threshold increases.

# 7.3 Relationship between PET microparameters and HRF parameters

## 7.3.1 Evaluation of collinearity between HRF parameters

The figures below show the pipeline used to evaluate the Pearson correlation between the hemodynamic parameters, and their sensitivity to the tumor overlap.

| | Amplitude | Amplitude trough | AUC | Fall slope | Rise slope | FWHM | Peak to trough | Time to peak | Time to trough |
|---|---|---|---|---|---|---|---|---|---|
| Amplitude | 0 | 0.5659 | 0.736 | 0.9018 | 0.7763 | 0.2151 | 0.3491 | 0 | 0.3136 |
| Amplitude trough | 0.5659 | 0 | 0 | 0.7013 | 0.5797 | 0.2553 | 0.251 | 0.1135 | 0.3859 |
| AUC | 0.736 | 0 | 0 | 0.4544 | 0.4698 | 0.1896 | 0.1795 | 0 | 0 |
| Fall slope | 0.9018 | 0.7013 | 0.4544 | 0 | 0.6934 | 0.4789 | 0.3555 | 0 | 0.4288 |
| Rise slope | 0.7763 | 0.5797 | 0.4698 | 0.6934 | 0 | 0.2813 | 0.3423 | 0.1515 | 0.3851 |
| FWHM | 0.2151 | 0.2553 | 0.1896 | 0.4789 | 0.2813 | 0 | 0.1621 | 0.5131 | 0.3747 |
| Peak to trough | 0.3491 | 0.251 | 0.1795 | 0.3555 | 0.3423 | 0.1621 | 0 | 0 | 0.2952 |
| Time to peak | 0 | 0.1135 | 0 | 0 | 0.1515 | 0.5131 | 0 | 0 | 0 |
| Time to trough | 0.3136 | 0.3859 | 0 | 0.4288 | 0.3851 | 0.3747 | 0.2952 | 0 | 0 |

**Figure 7.16. Pearson correlation through hemodynamic response parameters.** Pearson correlation between each pair of hemodynamic parameter values. Each distribution was obtained from the concatenation of the parameter values in parcels through subjects. The figure shows only values of correlation for statistically significant pairs (pvalue <0.05), otherwise set to zero.

## 7.3.2 Sensitivity to tumor overlap of HRF parameters

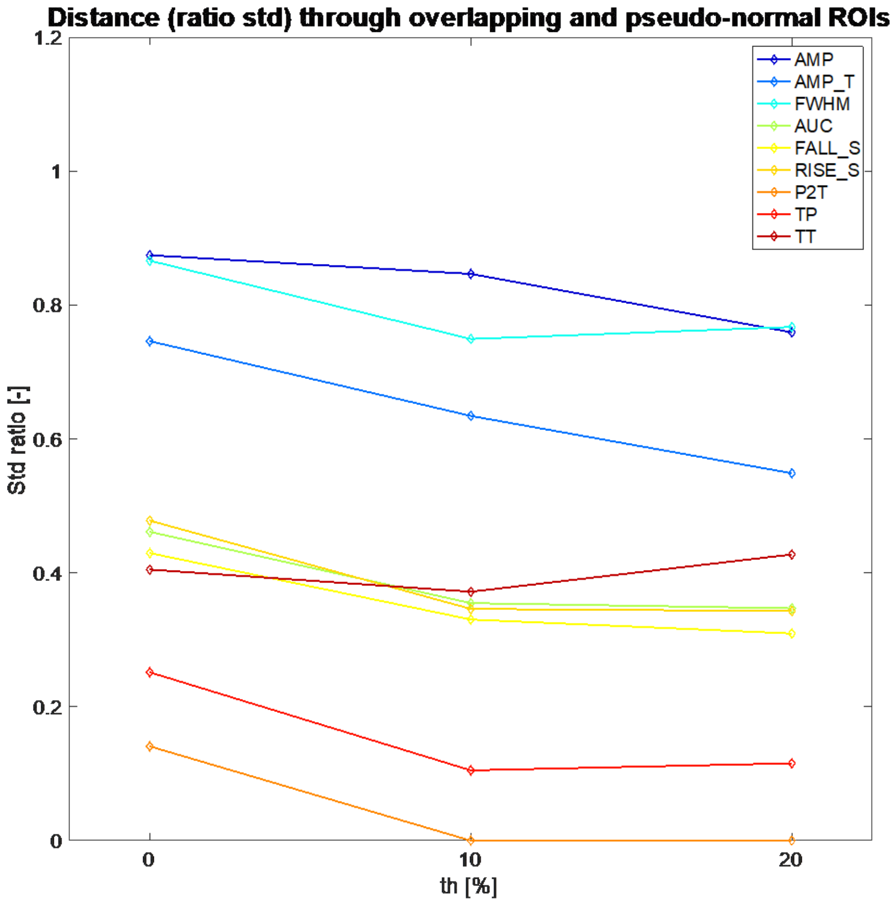

**Figure 7.17. Std ratio between overlapping and pseudonormal ROIs.** The figure shows the std ratio between overlapping and pseudonormal ROIs for each of the nine parameters and for the three thresholds of the overlap matrix. The std ratio values shown in the figure were calculated as the mean of the std ratio for all overlapping ROIs, as the difference between each overlapping ROI value and the median of the pseudonormal distribution, divided by the standard deviation of the pseudonormal distribution.

### 7.3.3 Parameter values through classes

From the analysis carried out previously on the hemodynamic response parameters, three were chosen and the figures below show the three pairs obtained by combining them.

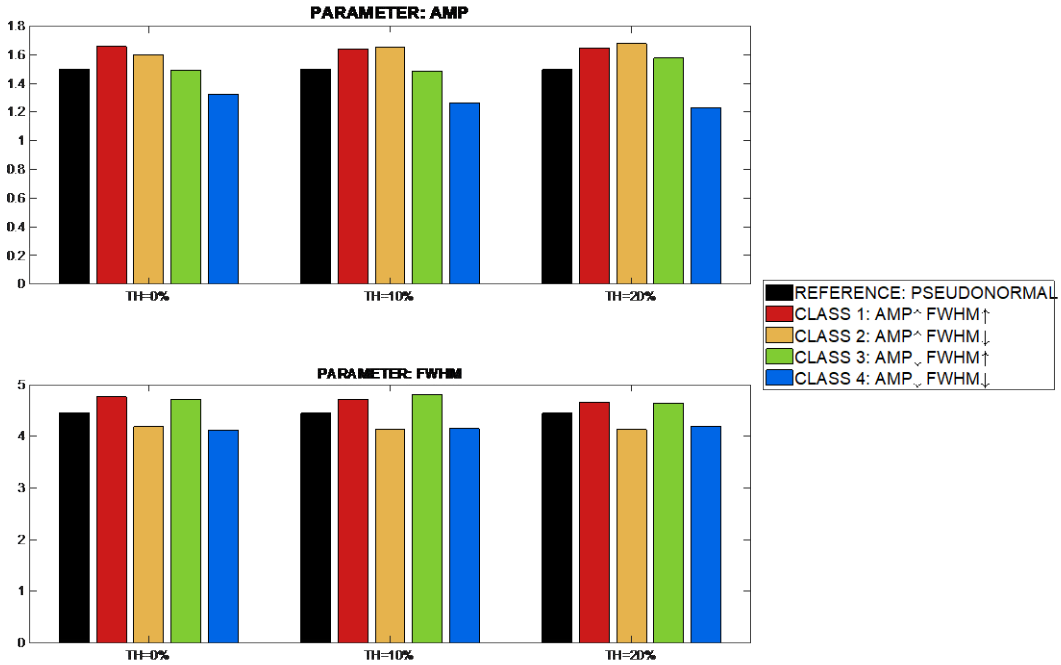

**Figure 7.18. AMP and FWHM values in each class.** The figure depicts the AMP and FWHM parameter values for every class, considering three different thresholds.

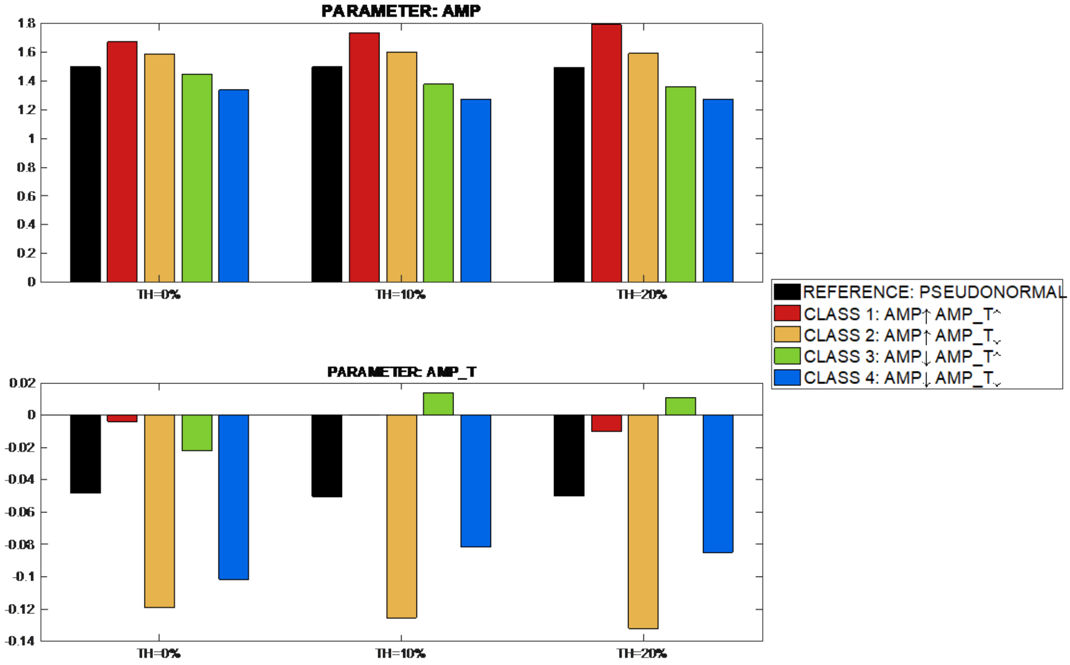

**Figure 7.19. AMP and AMP_T values in each class.** The figure depicts the AMP and AMP_T parameter values for every class, considering three different thresholds.

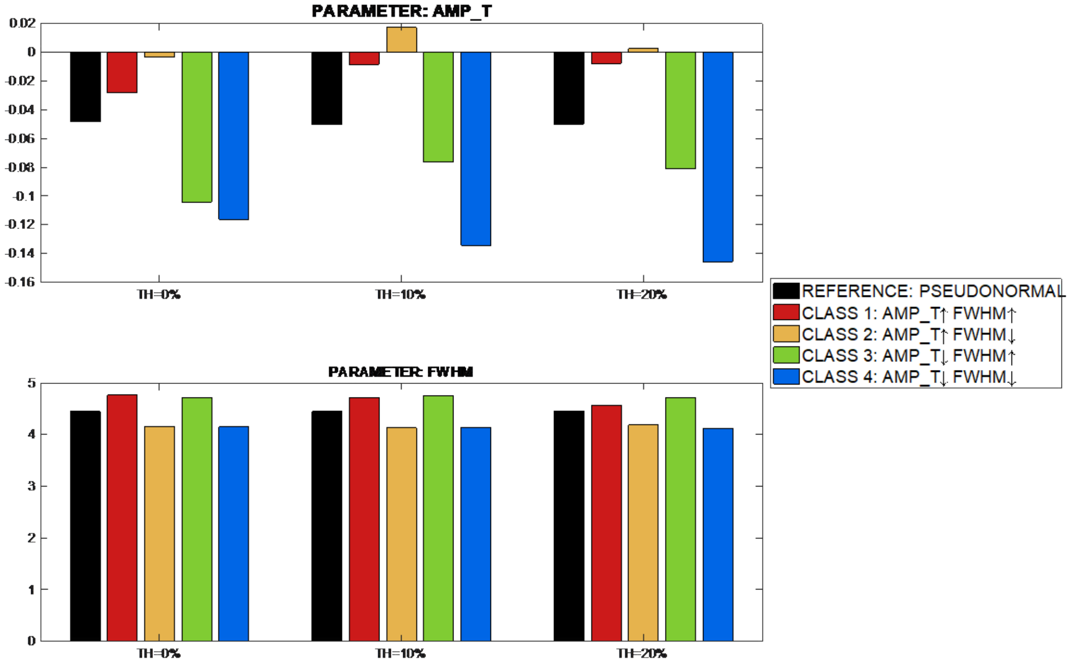

**Figure 7.20. AMP_T and FWHM values in each class.** The figure depicts the AMP_T and FWHM parameter values for every class, considering three different thresholds.

## 7.3.4 HRF through classes

The figures below show the mean of the hemodynamic response functions through the classes (and for every threshold) and their variability information with respect to the reference one.

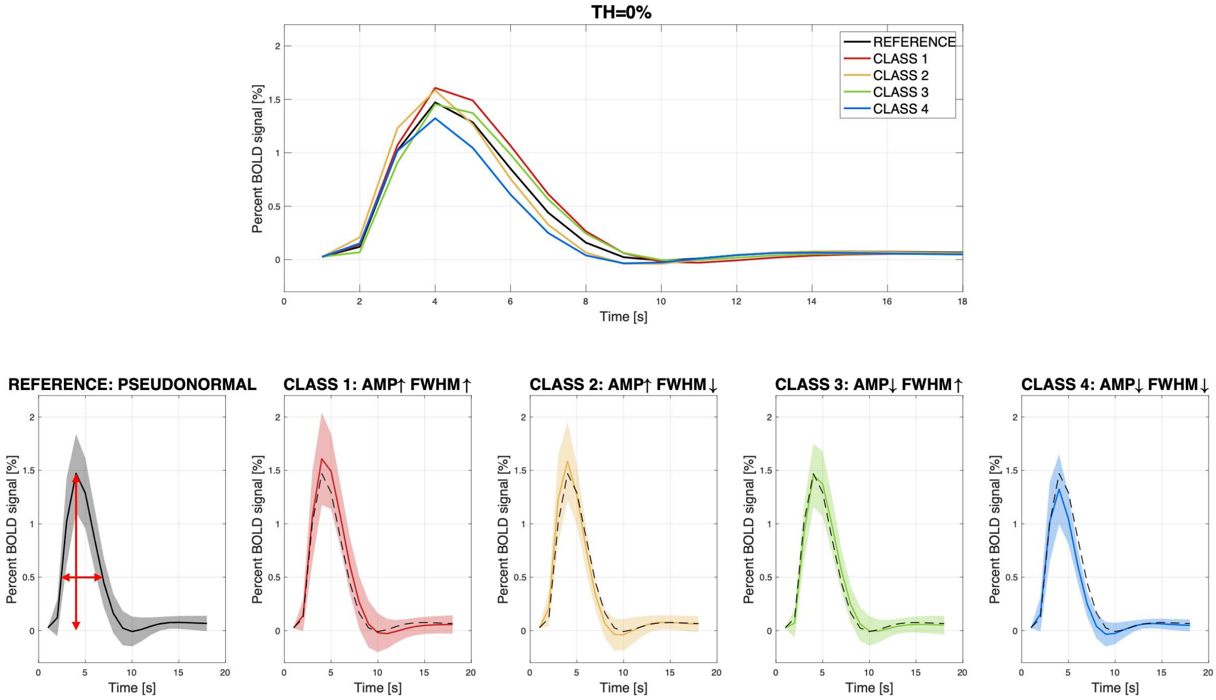

**Figure 7.21. Estimated hemodynamic responses for each of the five AMP/FWHM classes (overlap matrix threshold 0%).** The figure above shows the mean HRF estimated through every parcel's HRF. The figures below depict the HRF for every class, highlighting the mean and standard deviation, while the dashed line represents the mean of the pseudonormal values (REFERENCE).

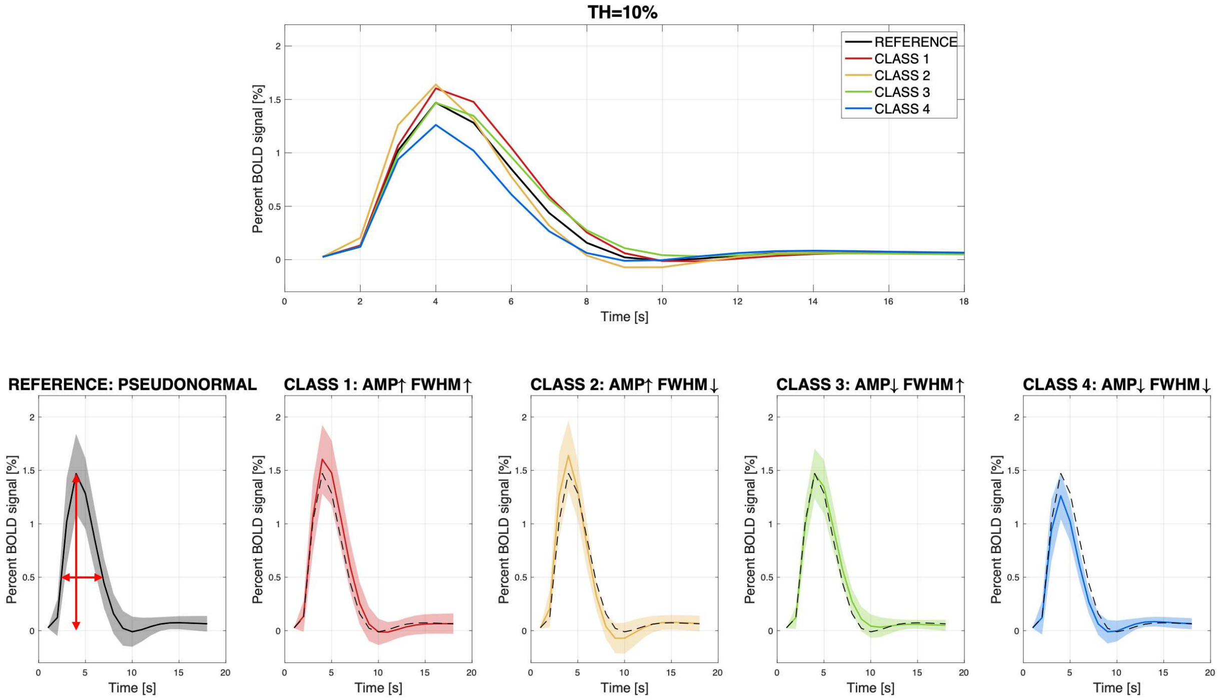

**Figure 7.22. Estimated hemodynamic responses for each of the five AMP/FWHM classes (overlap matrix threshold 10%).** The figure above shows the mean HRF estimated through every parcel's HRF. The figures below depict the HRF for every class, highlighting the mean and standard deviation, while the dashed line represents the mean of the pseudonormal values (REFERENCE).

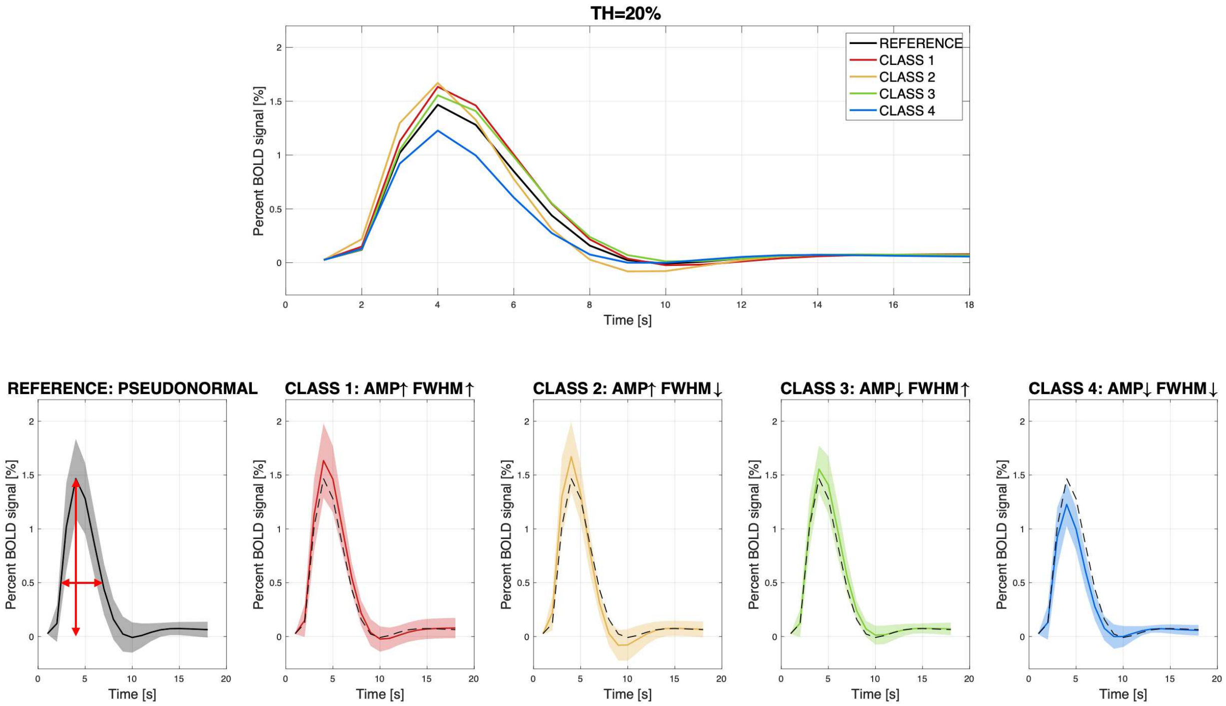

**Figure 7.23. Estimated hemodynamic responses for each of the five AMP/FWHM classes (overlap matrix threshold 20%).** The figure above shows the mean HRF estimated through every parcel's HRF. The figures below depict the HRF for every class, highlighting the mean and standard deviation, while the dashed line represents the mean of the pseudonormal values (REFERENCE).

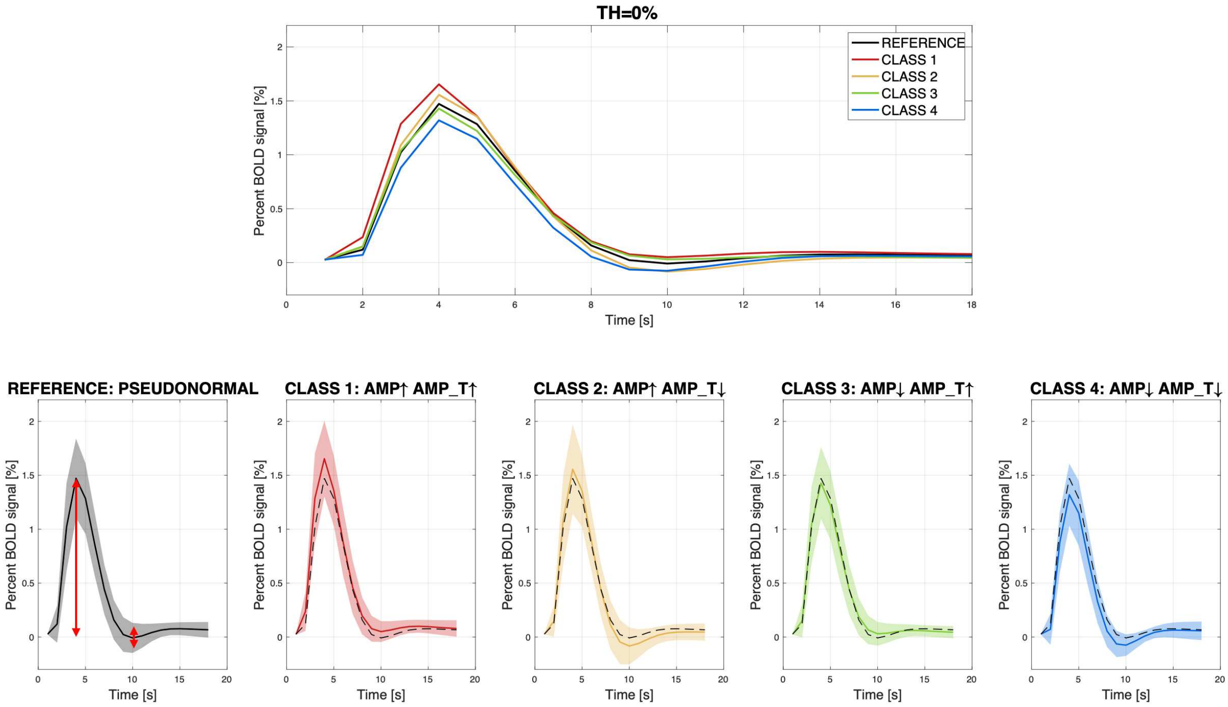

**Figure 7.24. Estimated hemodynamic responses for each of the five AMP/AMP_T classes (overlap matrix threshold 0%).** The figure above shows the mean HRF estimated through every parcel's HRF. The figures below depict the HRF for every class, highlighting the mean and standard deviation, while the dashed line represents the mean of the pseudonormal values (REFERENCE).

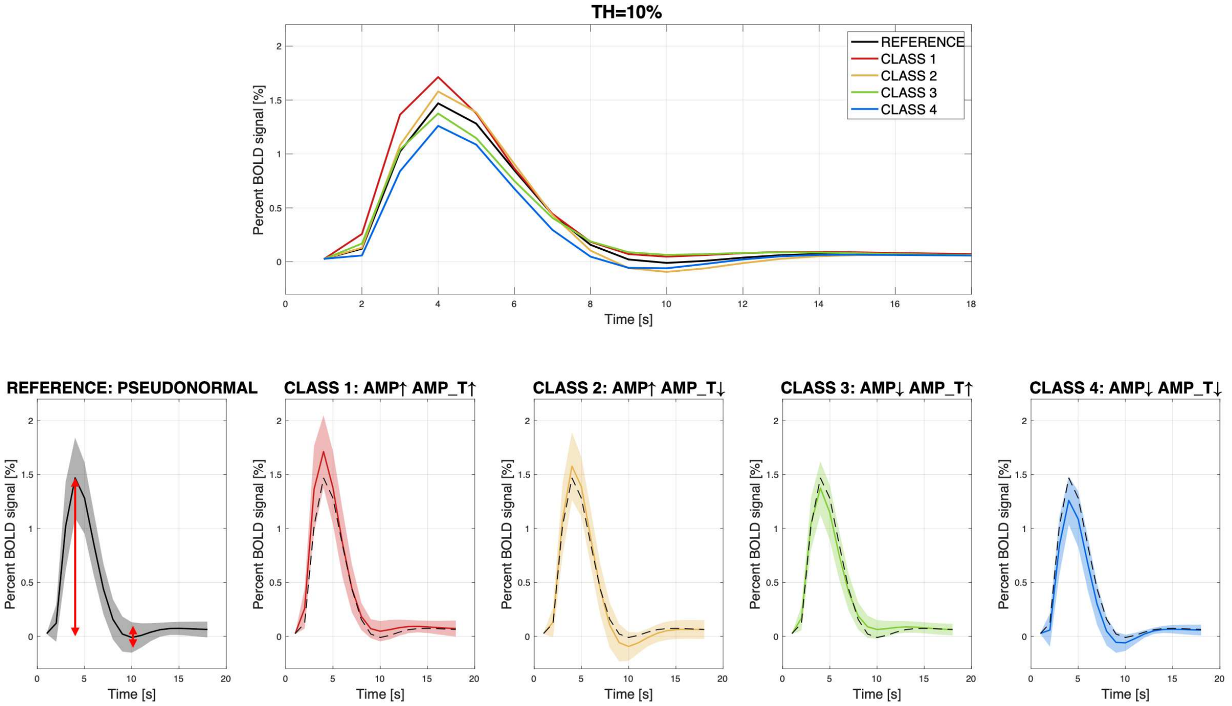

**Figure 7.25. Estimated hemodynamic responses for each of the five AMP/AMP_T classes (overlap matrix threshold 10%).** The figure above shows the mean HRF estimated through every parcel's HRF. The figures below depict the HRF for every class, highlighting the mean and standard deviation, while the dashed line represents the mean of the pseudonormal values (REFERENCE).

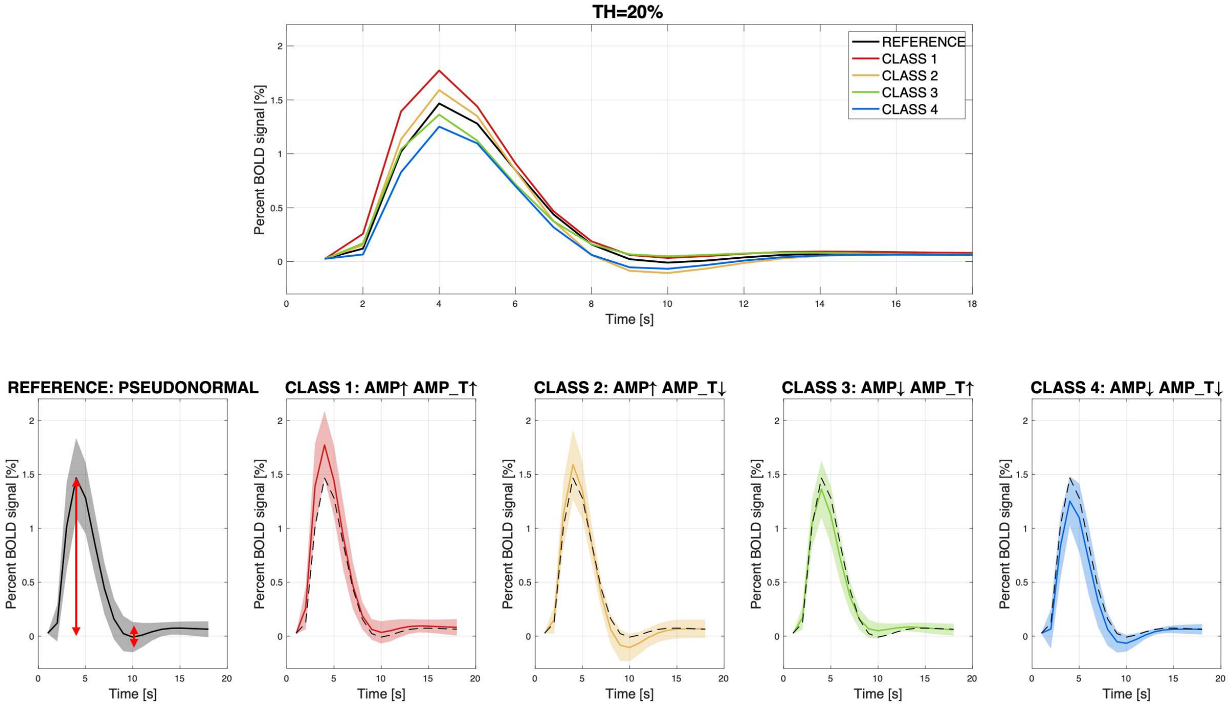

**Figure 7.26. Estimated hemodynamic responses for each of the five AMP/AMP_T classes (overlap matrix threshold 20%).** The figure above shows the mean HRF estimated through every parcel's HRF. The figures below depict the HRF for every class, highlighting the mean and standard deviation, while the dashed line represents the mean of the pseudonormal values (REFERENCE).

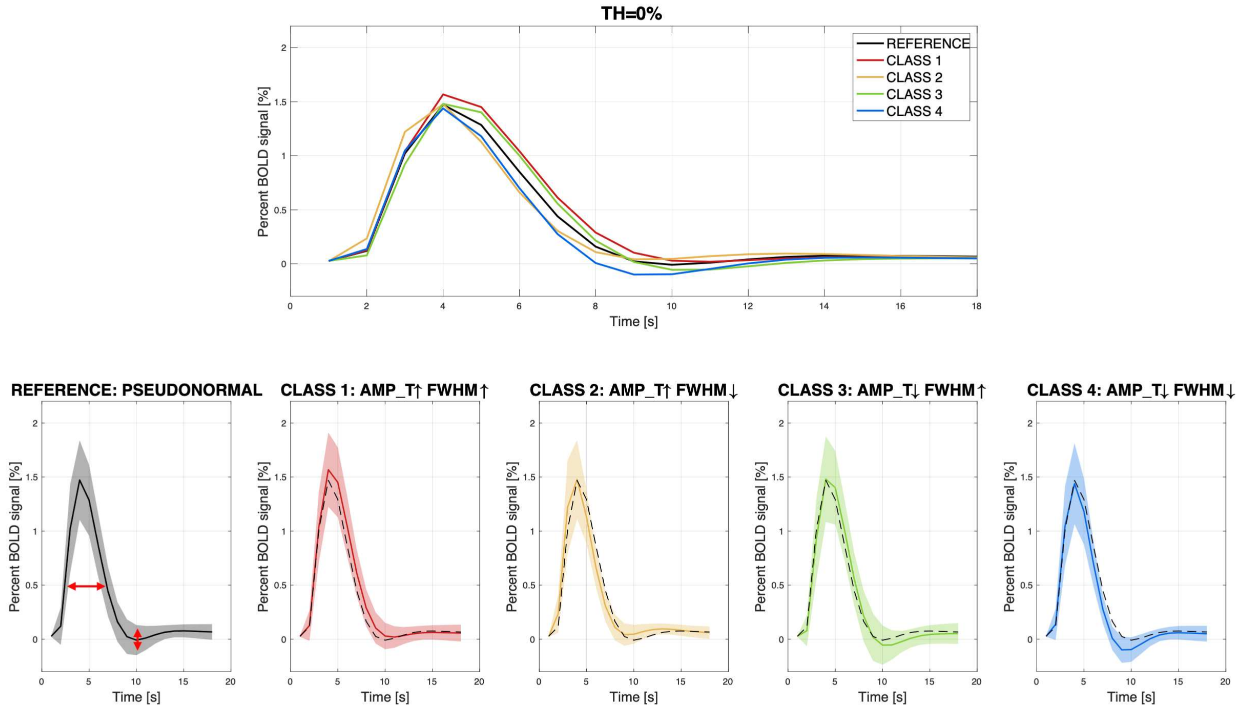

**Figure 7.27. Estimated hemodynamic responses for each of the five AMP_T/FWHM classes (overlap matrix threshold 10%).** The figure above shows the mean HRF estimated through every parcel's HRF. The figures below depict the HRF for every class, highlighting the mean and standard deviation, while the dashed line represents the mean of the pseudonormal values (REFERENCE).

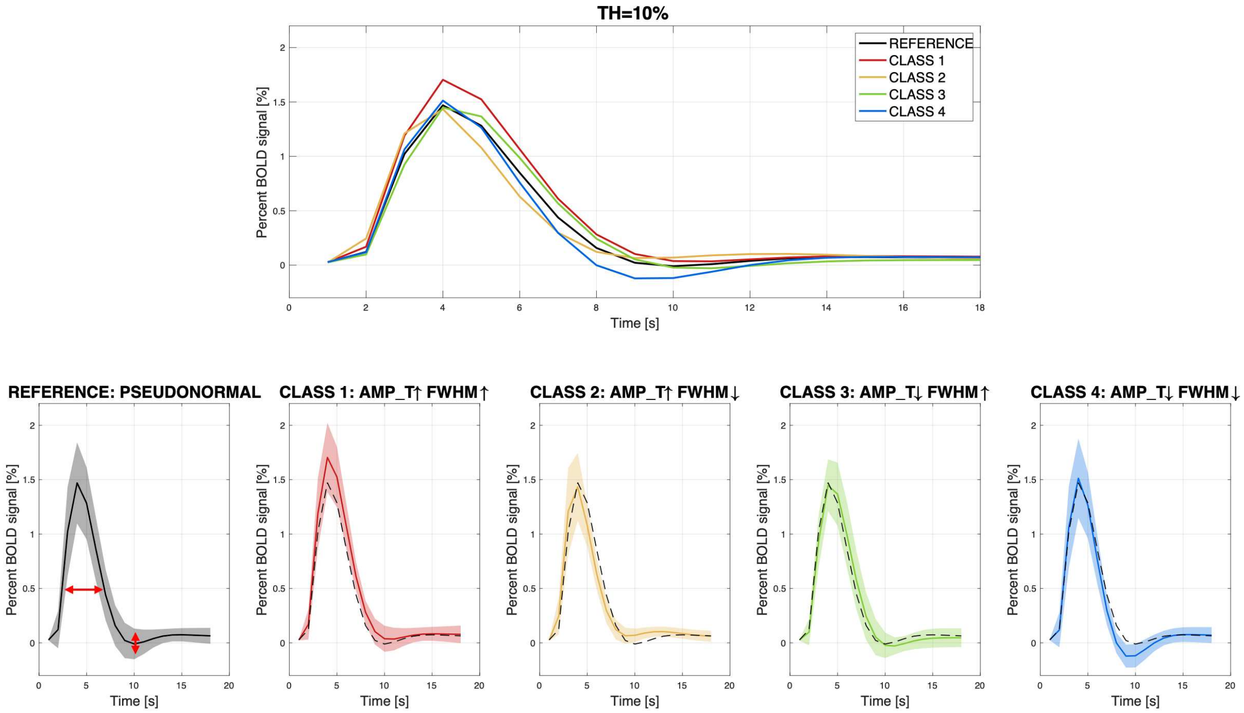

**Figure 7.28. Estimated hemodynamic responses for each of the five AMP_T/FWHM classes (overlap matrix threshold 10%).** The figure above shows the mean HRF estimated through every parcel's HRF. The figures below depict the HRF for every class, highlighting the mean and standard deviation, while the dashed line represents the mean of the pseudonormal values (REFERENCE).

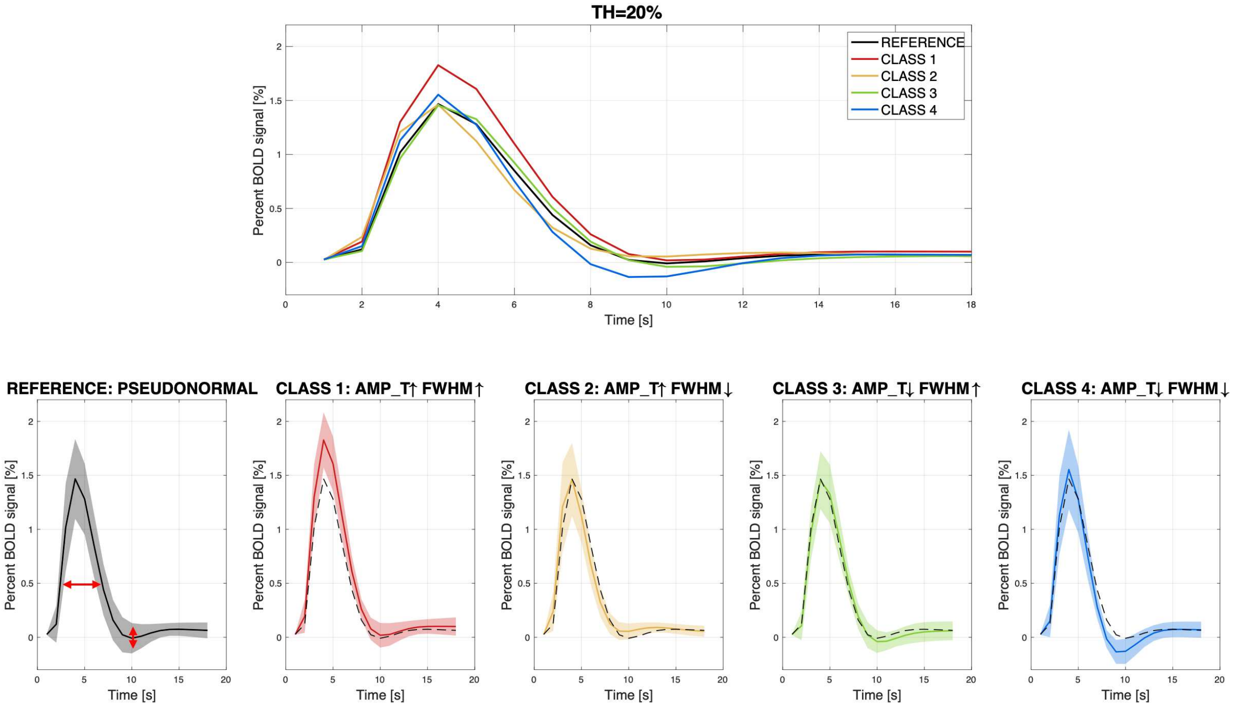

**Figure 7.29. Estimated hemodynamic responses for each of the five AMP_T/FWHM classes (overlap matrix threshold 20%).** The figure above shows the mean HRF estimated through every parcel's HRF. The figures below depict the HRF for every class, highlighting the mean and standard deviation, while the dashed line represents the mean of the pseudonormal values (REFERENCE).

## 7.3.5 Spatial distribution of classes for different thresholds

The figures show the spatial representation and distribution of the classes for three reference subjects (left, right and bilateral tumor) by varying the thresholds.

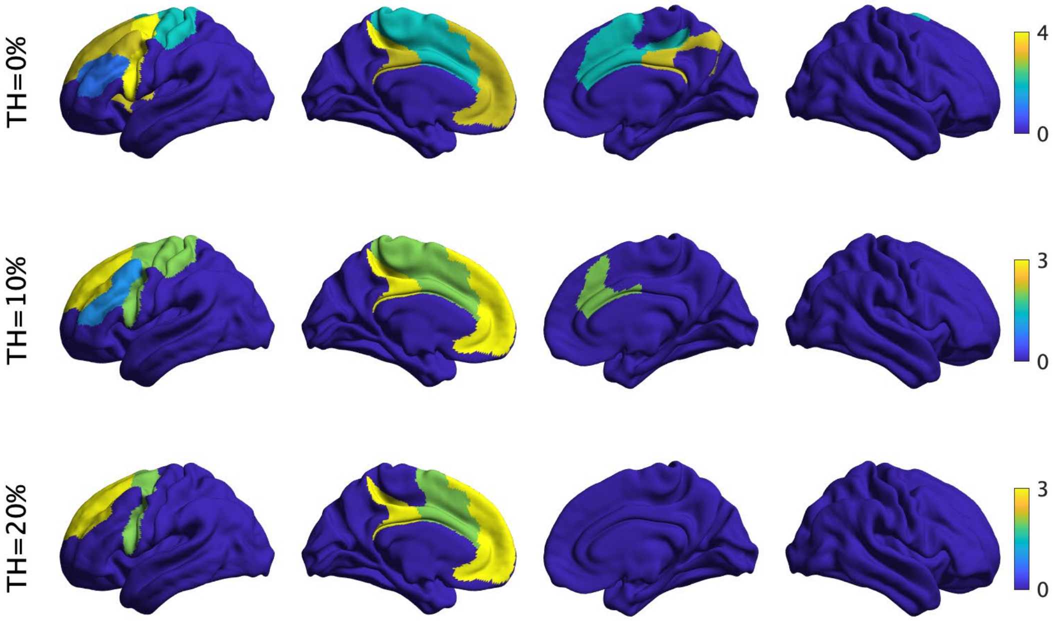

**Figure 7.30. Spatial distribution of classes for Subject 3, left hemisphere tumor.** The figures show the spatial distribution across ROIs of the classes across the three thresholds for an exemplary left hemisphere tumor subject[27].

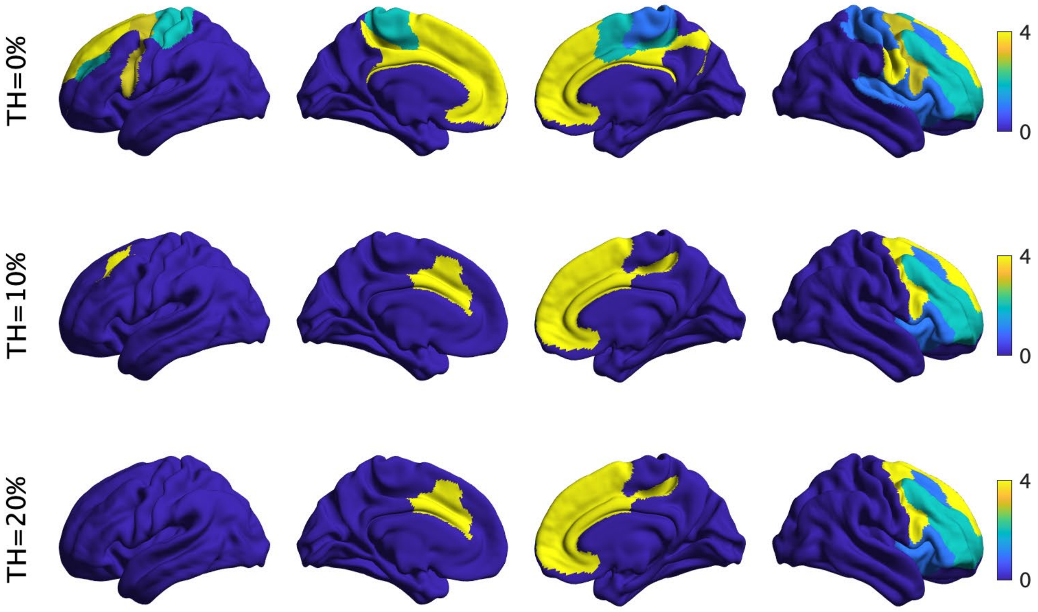

**Figure 7.31. Spatial distribution of classes for Subject 8, bilateral tumor.** The figures show the spatial distribution across ROIs of the classes across the three thresholds for an exemplary bilateral hemisphere tumor subject[27].

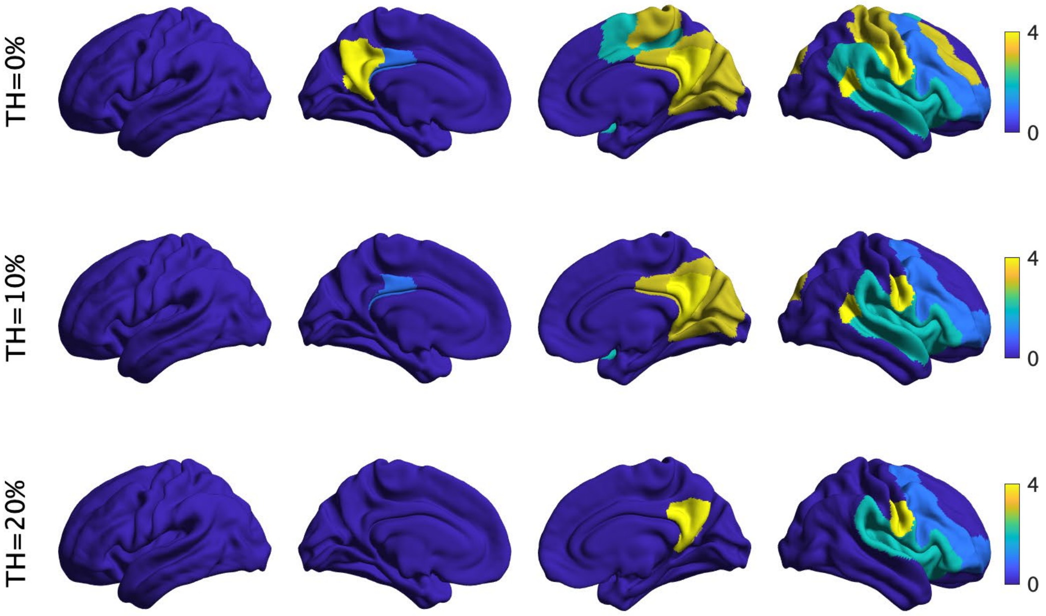

**Figure 7.32. Spatial distribution of classes for Subject 9, right hemisphere tumor.** The figures show the spatial distribution across ROIs of the classes across the three thresholds for an exemplary right hemisphere tumor subject[27].

## 7.3.6 K1 and k3 values through classes

The following results show the distribution of z-scored K1 and k3 values for each of previously formed class. In general, k3 values show more significant differences through classes than the microparameter K1. All the differences were tested using an *anova* test and multiple comparison test (significance level 5%).

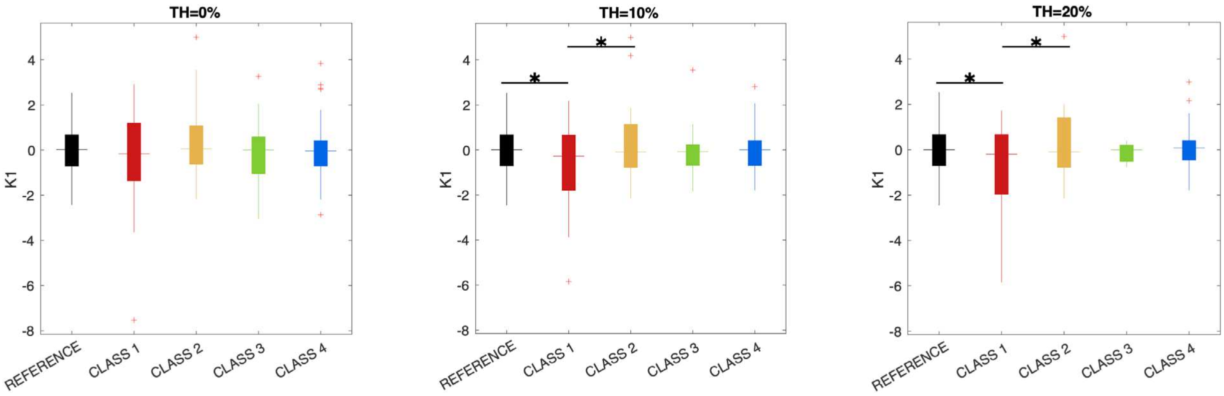

**Figure 7.33. Boxplots of z-score K1 values in the five classes for the AMP and FWHM pair of parameters.** The figure shows the boxplots of the K1 microparameter values divided into five classes, z-score across subjects and across regions of interest. The classes were created considering the AMP and FWHM pair of parameters. The asterisks (*) denote the statistically significant pairwise differences.

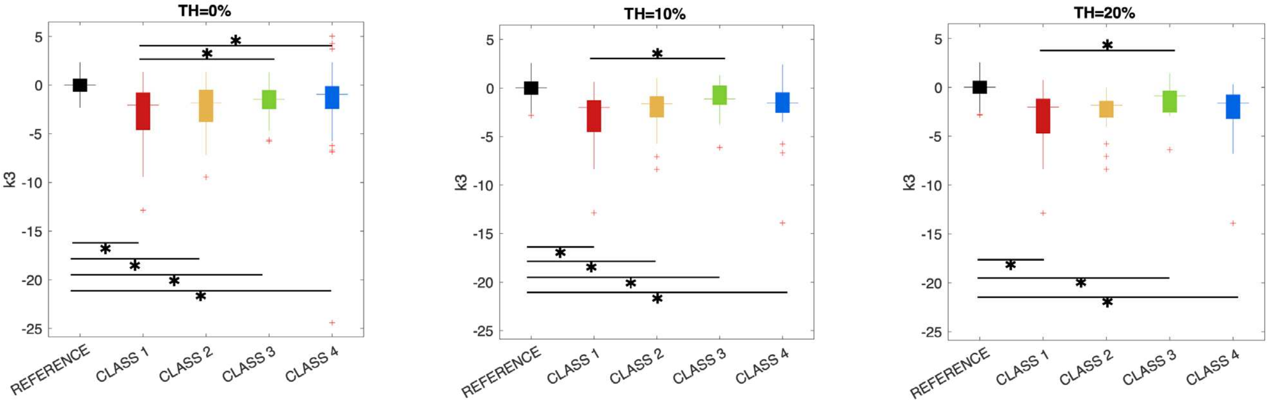

**Figure 7.34. Boxplots of z-scored k3 values in the five classes for the AMP and FWHM pair of parameters.** The figure shows the boxplots of the k3 microparameter values divided into five classes, z-score across subjects and across regions of interest. The classes were created considering the AMP and FWHM pair of parameters. The asterisks (*) denote the statistically significant pairwise differences.

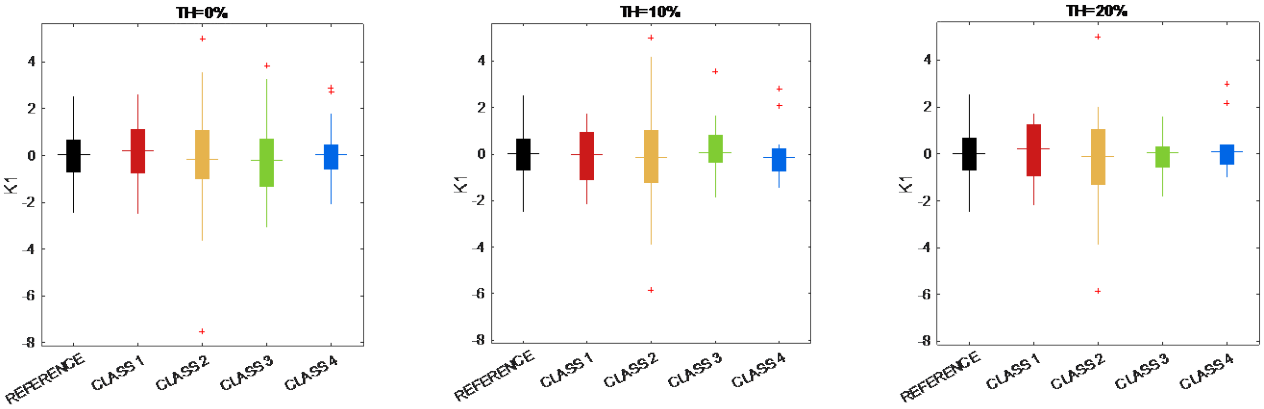

**Figure 7.35. Boxplots of z-scored K1 values in the five classes for the AMP and AMP_T pair of parameters.** The figure shows the boxplots of the K1 microparameter values divided into five classes, z-score across subjects and across regions of interest. The classes were created considering the AMP and AMP_T pair of parameters. The asterisks (*) denote the statistically significant pairwise differences.

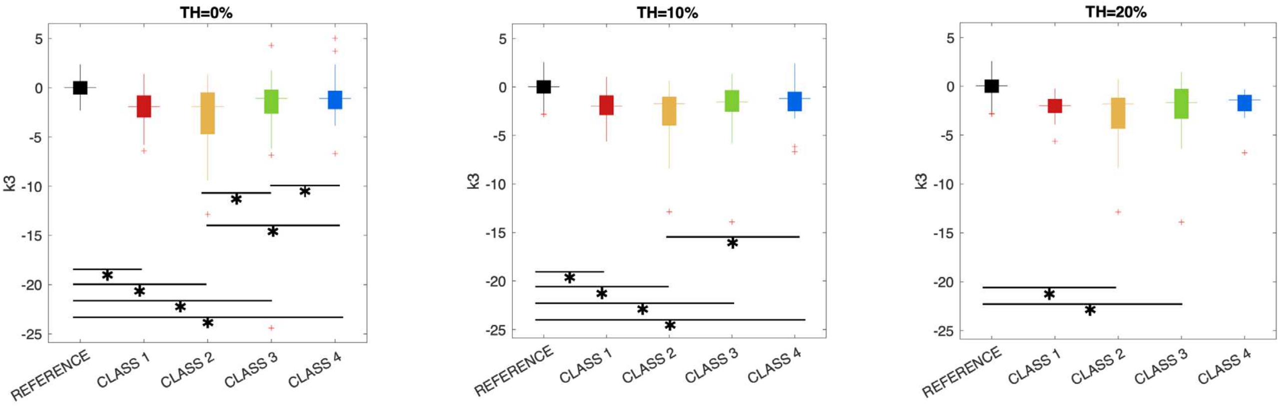

**Figure 7.36. Boxplots of z-scored k3 values in the five classes for the AMP and AMP_T pair of parameters.** The figure shows the boxplots of the k3 microparameter values divided into five classes, z-score across subjects and across regions of interest. The classes were created considering the AMP and AMP_T pair of parameters. The asterisks (*) denote the statistically significant pairwise differences.

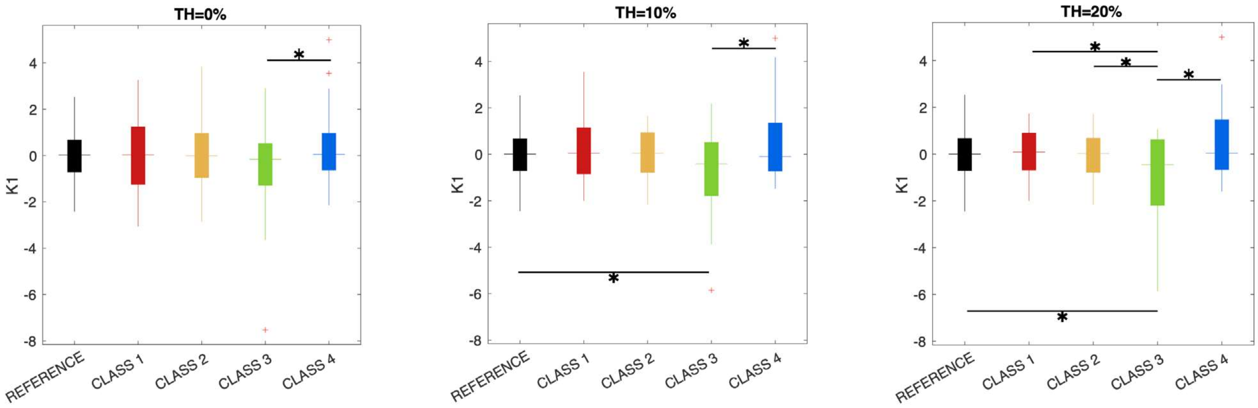

**Figure 7.37. Boxplots of z-scored K1 values in the five classes for the AMP_T and FWHM pair of parameters.** The figure shows the boxplots of the K1 microparameter values divided into five classes, z-score across subjects and across regions of interest. The classes were created considering the AMP_T and FWHM pair of parameters. The asterisks (*) denote the statistically significant pairwise differences.

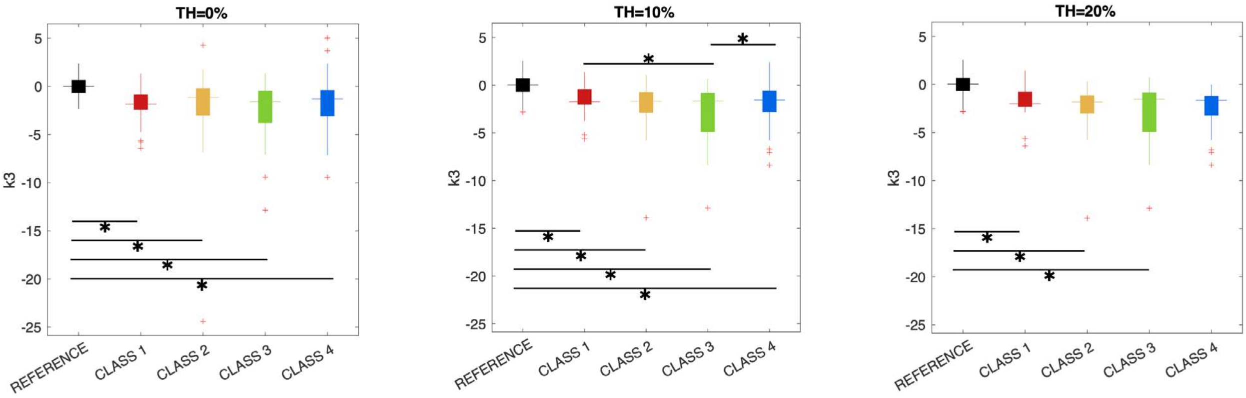

**Figure 7.38. Boxplots of z-scored k3 values in the five classes for the AMP_T and FWHM pair of parameters.** The figure shows the boxplots of the k3 microparameter values divided into five classes, z-score across subjects and across regions of interest. The classes were created considering the AMP_T and FWHM pair of parameters. The asterisks (*) denote the statistically significant pairwise differences.

# 7.4 Effective Connectivity and Gradients

## 7.4.1 EC matrix and node degree

The matrices below show the sparse EC of control and brain tumor subjects, and an initial analysis performed on them.

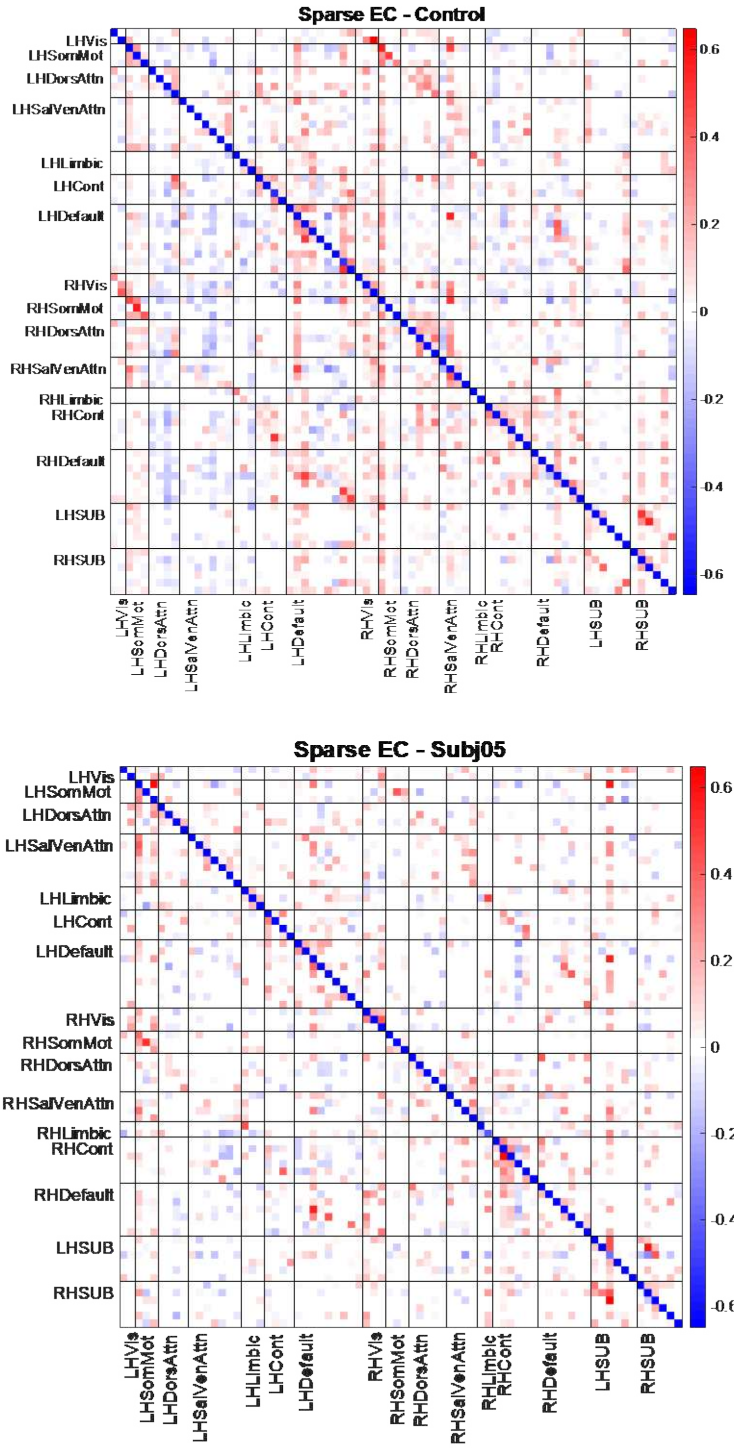

**Figure 7.39. Sparse EC matrices for a control subject and subject 5 (left hemisphere tumor).** The figures show an example of an effective connectivity matrix for a control subject and for a left hemisphere tumor subject 5.

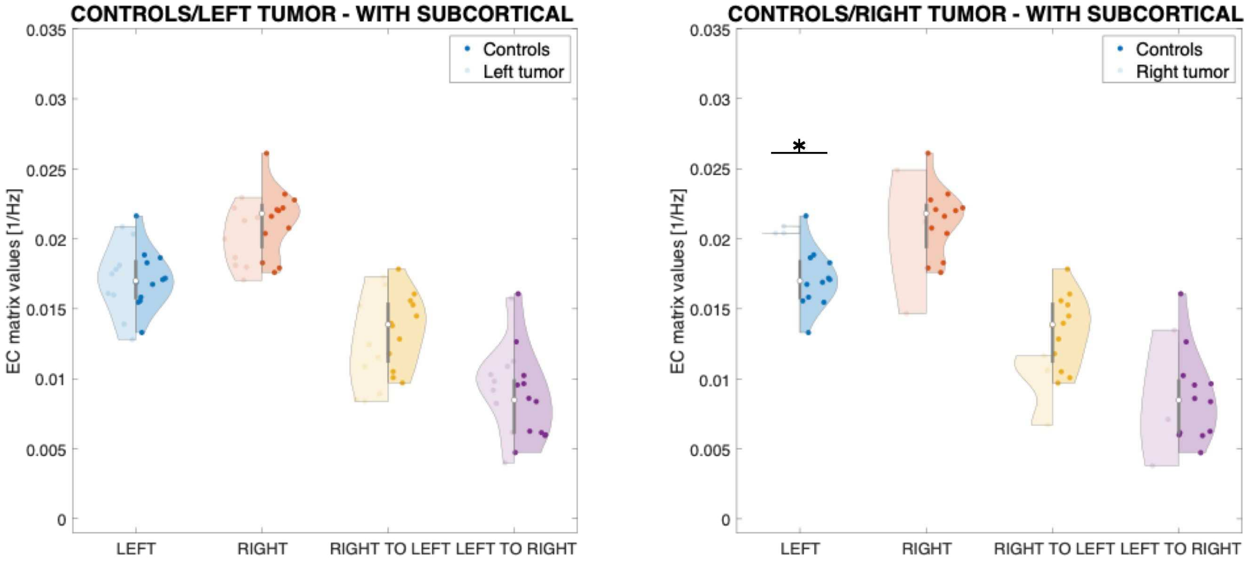

**Figure 7.40. Violin plot of mean EC matrix values.** The figures show the EC matrix mean values respectively for the intra-left, intra-right, right-to-left, and left-to-right hemispheres, by dividing the subjects according to the hemisphere of the lesion and comparing them with 12 controls. These values have been obtained by considering cortical and subcortical regions of the brain.

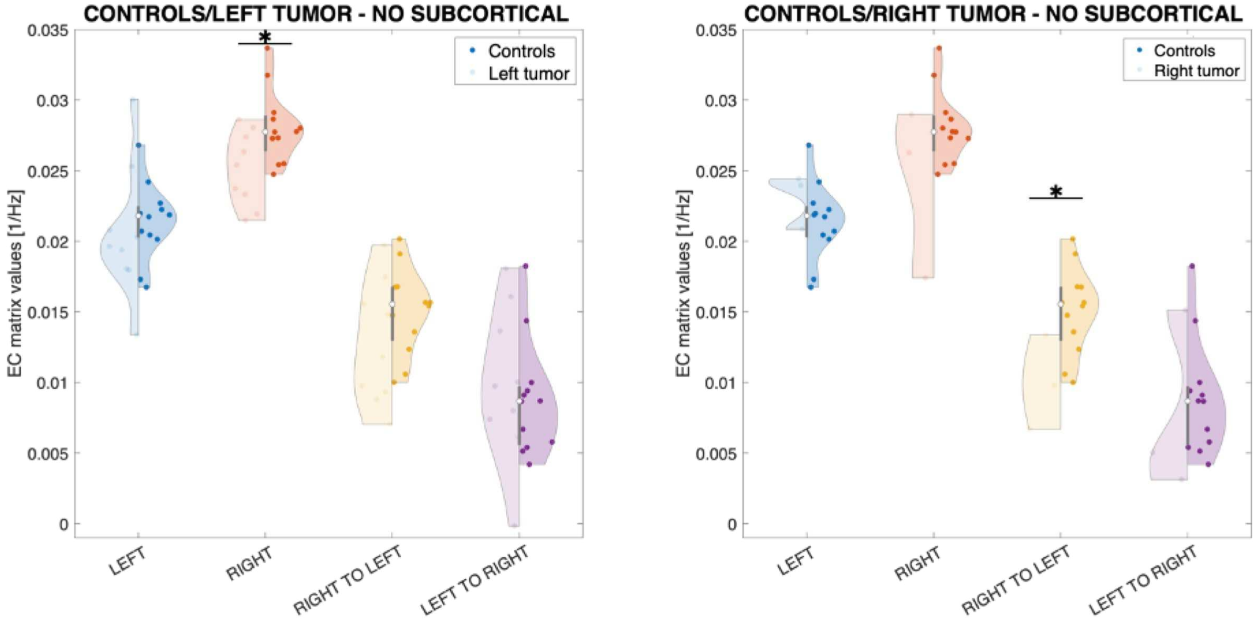

**Figure 7.41. Violin plot of mean EC matrix values.** The figure shows the EC matrix mean values respectively for the intra-left, intra-right, right-to-left, and left-to-right hemispheres, by dividing the subjects according to the hemisphere of the lesion and comparing them with 12 controls. These values have been obtained by considering only cortical regions of the brain.

It is important to emphasize that from the forthcoming analyses on EC matrices, subcortical parcels will no longer be taken into account, since in the literature the application of gradients usually does not involve them[29].

## 7.4.2 Eigenvalue assessment

The following results were obtained by applying the tools provided by the BrainSpace v0.2.1 to the effective connectivity matrices.

The diagonal values of each EC matrix have been set to zero and only cortical parcels were considered. after testing the three thresholds for the overlap matrix, the 20% threshold of the overlap matrix showed more statistically significant results compared to the other thresholds. In addition, the highest threshold ensures the presence of an evident alteration caused by the brain tumor, then only this threshold has been considered in the following connectivity analysis. Every analysis was performed taking into consideration the directionality of the matrices, thus both for incoming and outgoing EC matrices.

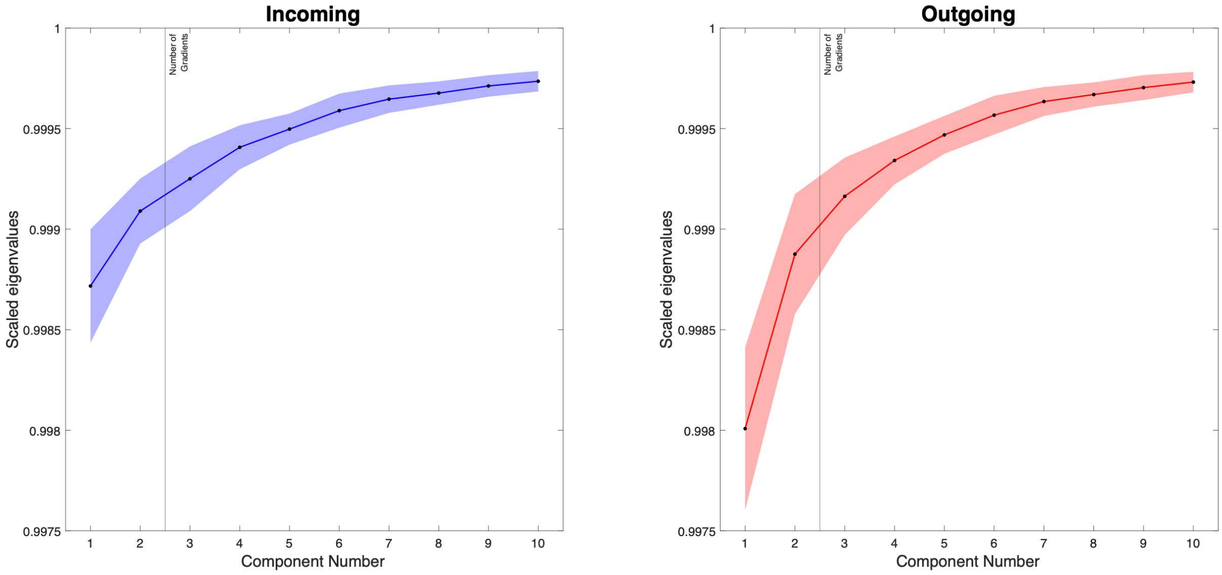

**Figure 7.42. Incoming and outgoing EC matrix eigenvalues for each component.** The figure shows the values of the eigenvalues through subjects, for each component and dividing between incoming and outgoing EC.

## 7.4.3 Alignment

After an initial analysis that showed inconsistencies in the spatial distribution of gradients, each patient was aligned to a reference common space obtained by computing gradients on the concatenated EC matrix from the 12 controls (Figure 7.43). The figures below depict the results only by considering the chosen 20% threshold of the overlap matrix. In the following analysis, the number of gradients assessed is two, as shown in Figure 7.42.

From Figure 7.43, the 2D group-level representation of Gradient1 and Gradient2 for both incoming and outgoing links is rather complex, thus the following analyses were also carried out at single-subject level.
The figures below show the 2D representation of the regions' distribution by considering the Gradient1/Gradient2 space.

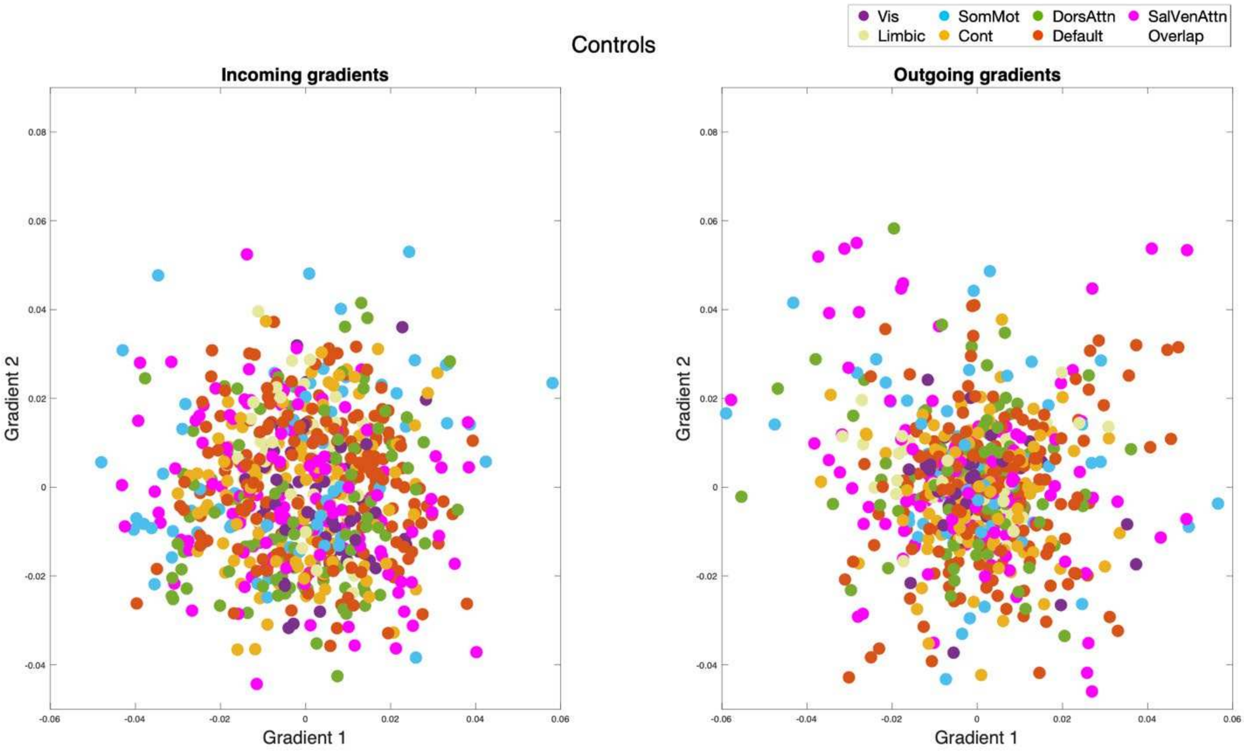

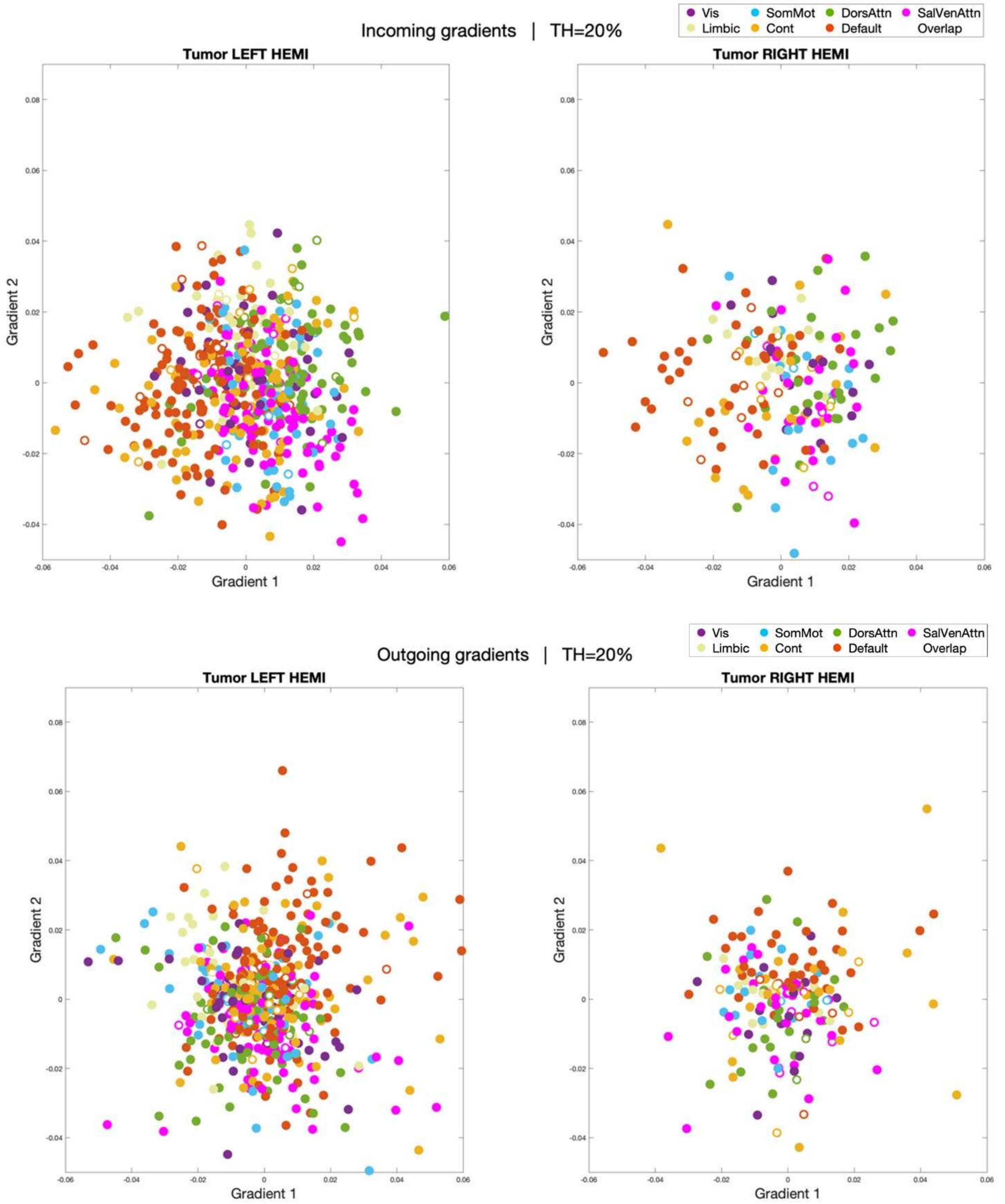

**Figure 7.43. 2D representation of incoming and outgoing Gradient 1 and Gradient 2 of control, left hemisphere, and right hemisphere subjects.** The figures show the 2D representation of Gradient 1 and Gradient 2 for twelve control subjects, nine subjects with a tumor in the left hemisphere, and three in the right hemisphere. The analysis was performed for the incoming and outgoing EC matrices. The numerosity of subjects is much different, for instance, there are only three subjects with tumors in the right hemisphere, compared to nine with a lesion on the left and 12 controls.

### 7.4.4 Single subject analysis

In addition to the group analysis, the figures below display the single-subject 2D distribution.

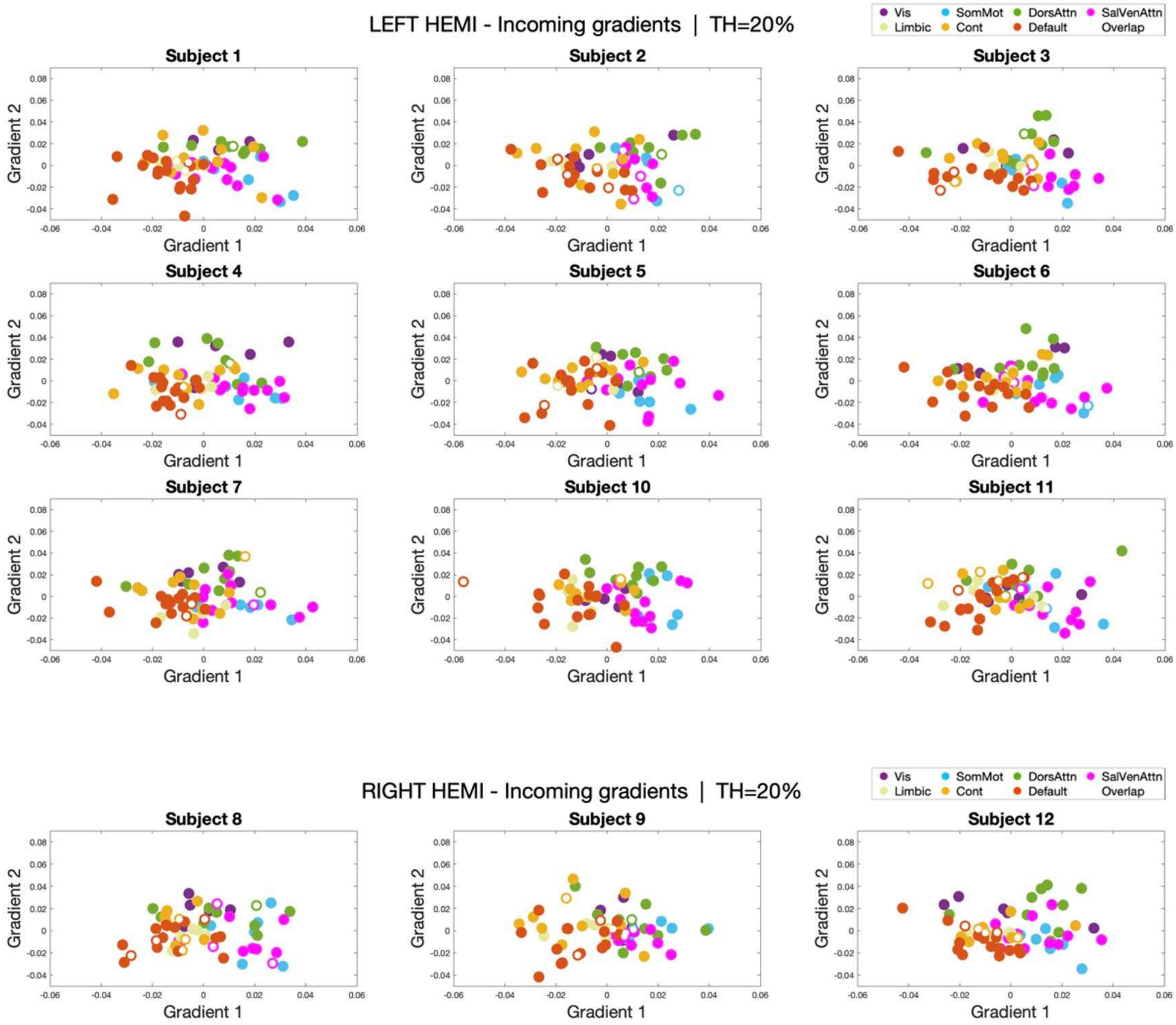

**Figure 7.44. 2D representation of incoming Gradient 1 and Gradient 2.** The figures show the 2D representation of the Gradient 1 and Gradient 2 for every aligned subject, dividing them into subjects with the tumor in left (above) and right (below) hemisphere. The analysis was performed for the incoming EC matrix.

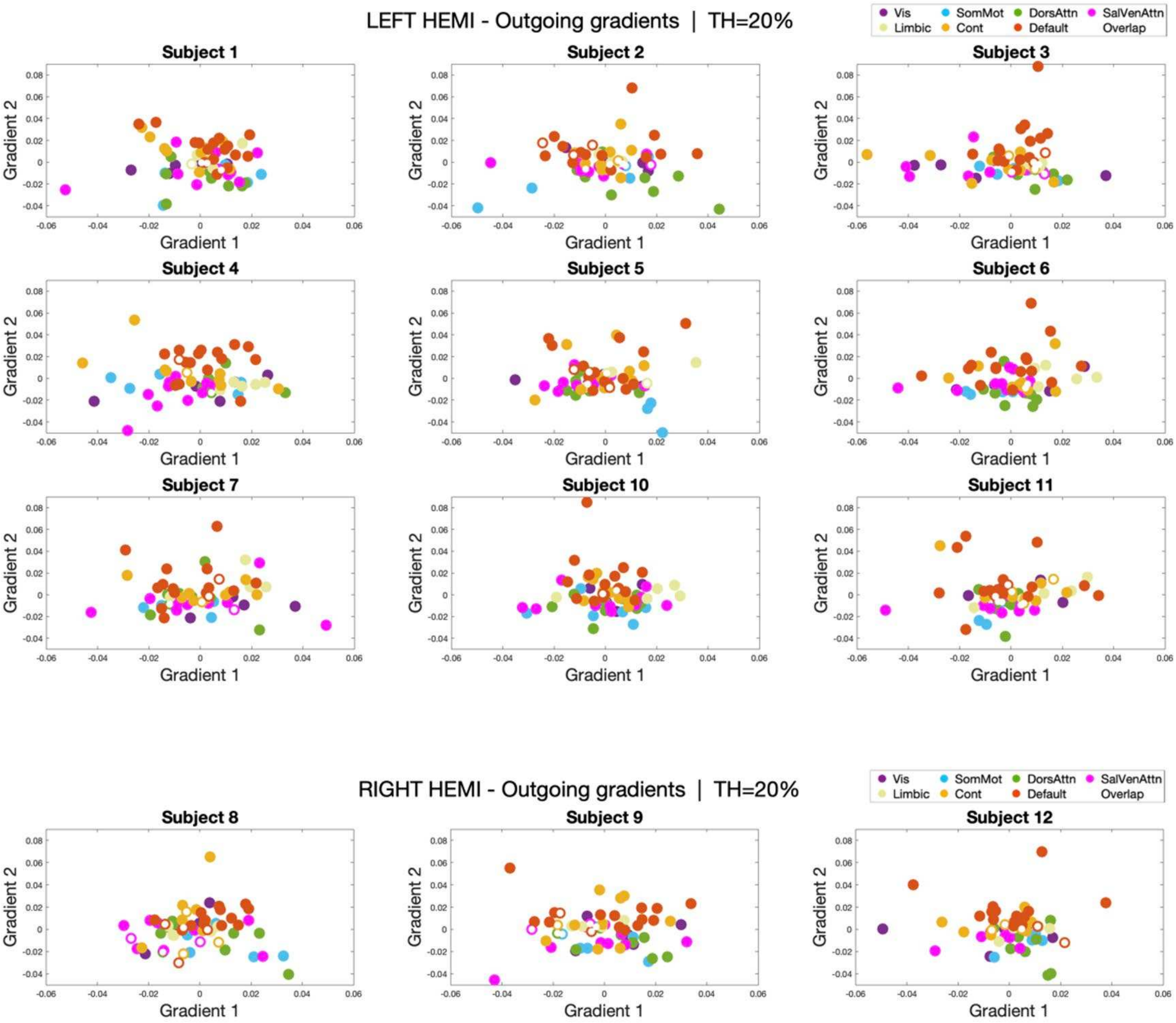

**Figure 7.45. 2D representation of outgoing Gradient 1 and Gradient 2.** The figures show the 2D representation of the Gradient 1 and Gradient 2 for every aligned subject, dividing them into subjects with the tumor in left (above) and right (below) hemisphere. The analysis was performed for the outgoing EC matrix.

## 7.4.5 Silhouette assessment

The following figures show the Silhouette values boxplots for the pseudonormal and overlapping regions, both at group and single-subject levels. All the statistically significant differences were quantified using a *Wilcoxon rank sum* test (significance level 5%).

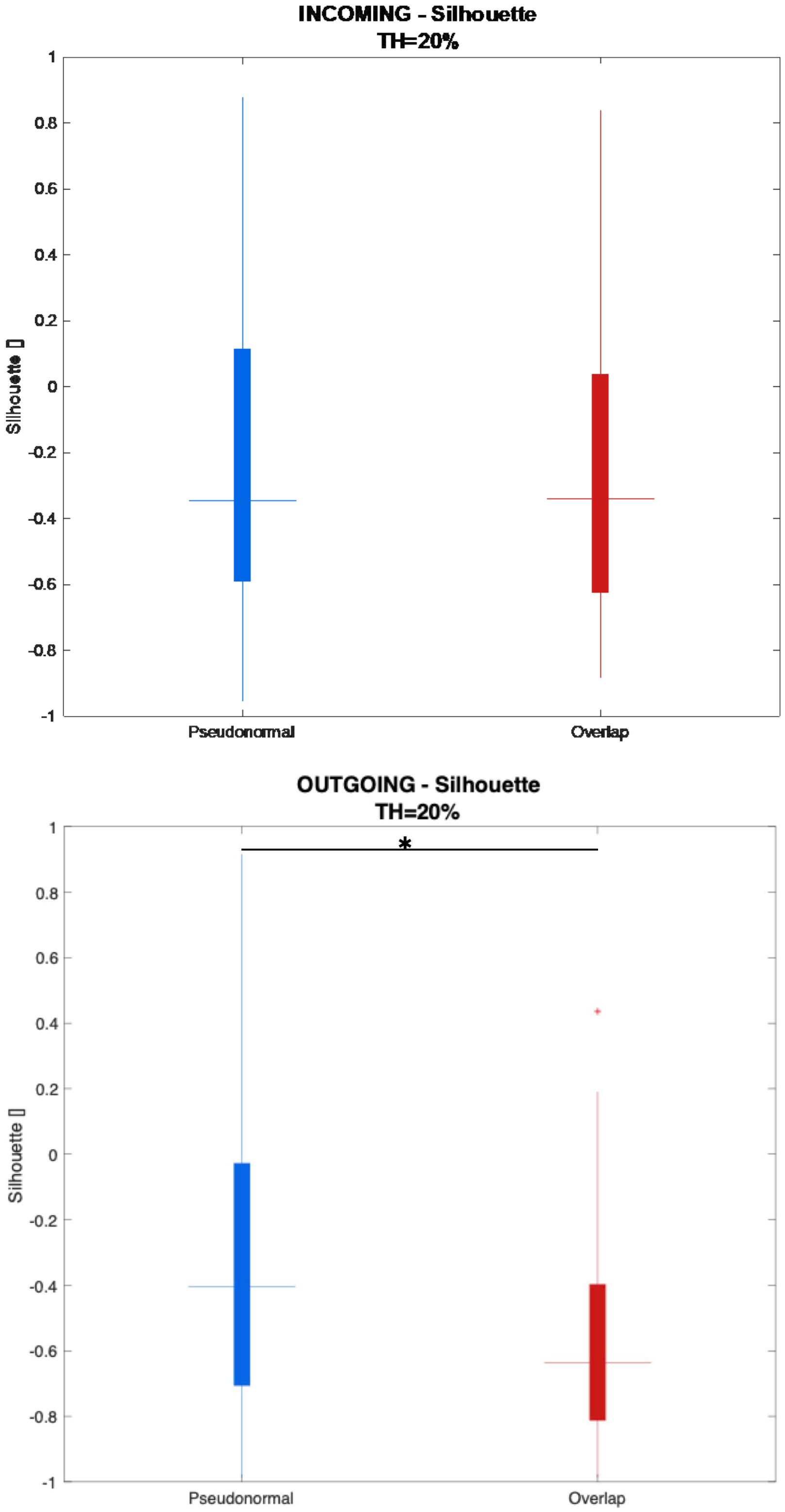

**Figure 7.46. Silhouette global coefficients.** The figure shows the boxplots of the Silhouette coefficient value for the pseudonormal and overlapping regions, highlighting a significative difference for the outgoing ones.

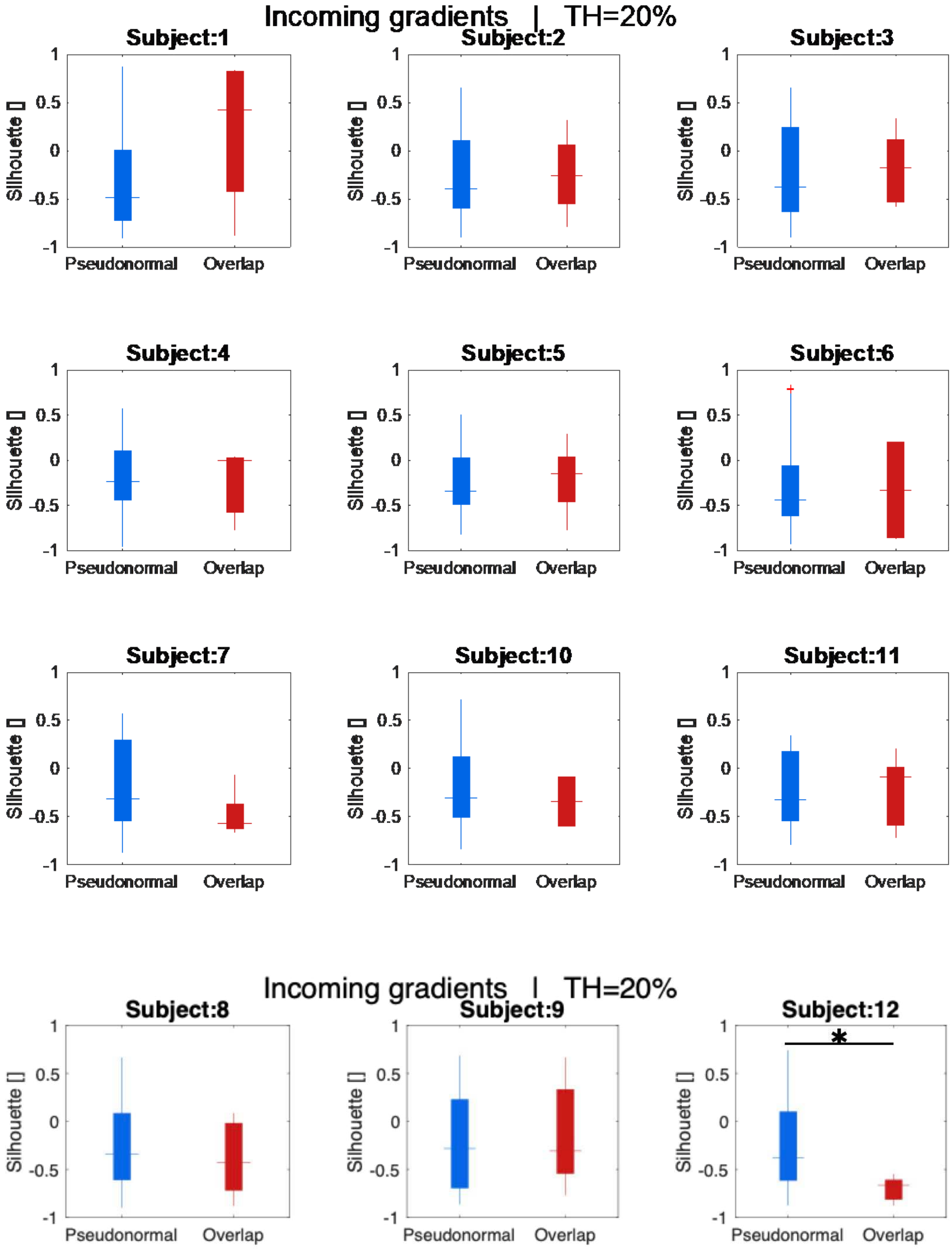

**Figure 7.47. Boxplot of the silhouette coefficient for incoming EC matrices.** The figures show the silhouette coefficient computed for every ROI, by considering the brain networks as clusters. The boxplots are divided between pseudonormal and tumor overlap ROIs.

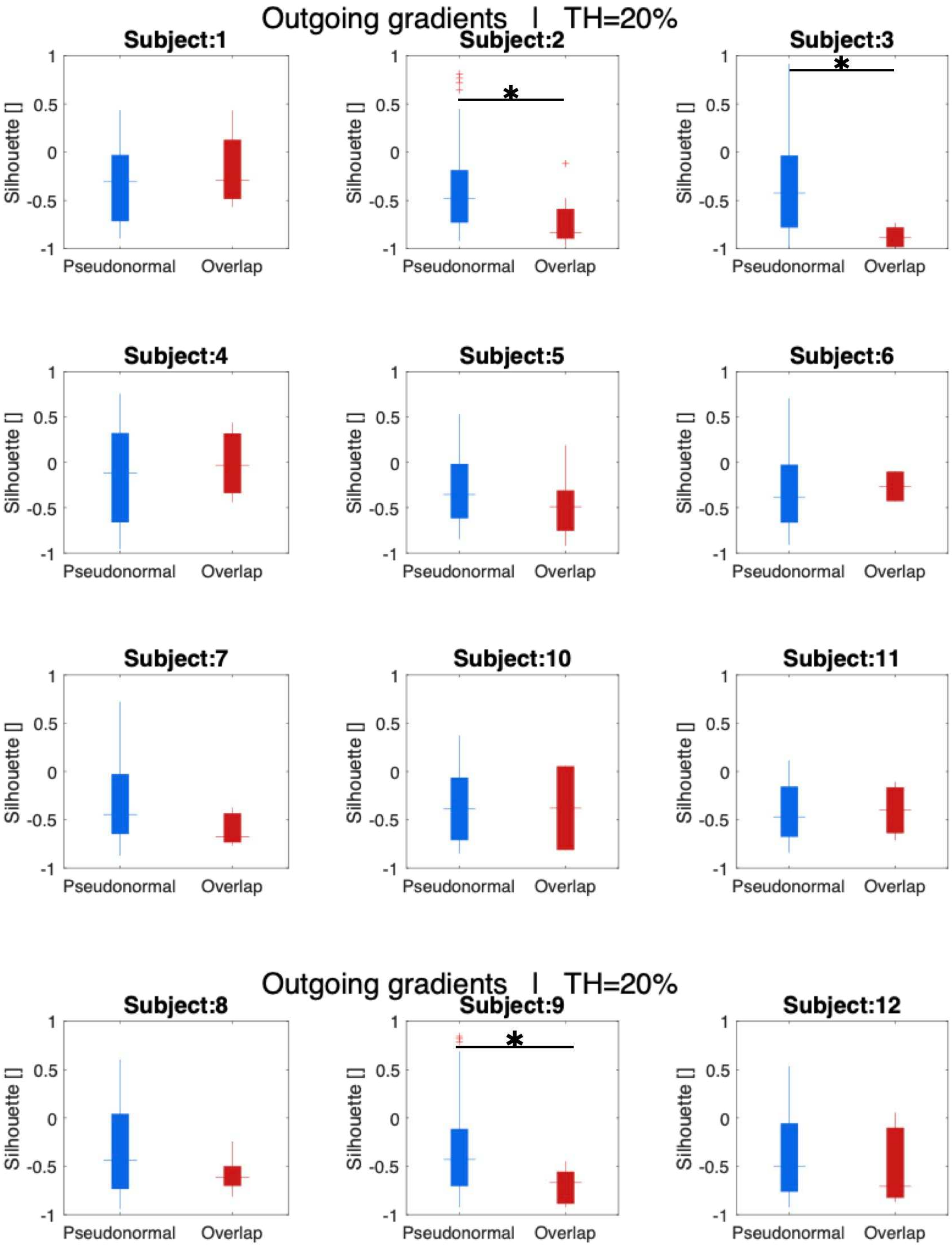

**Figure 7.48. Boxplot of the silhouette coefficient for outgoing EC matrices.** The figures show the silhouette coefficient computed for every ROI, by considering the brain networks as clusters. The boxplots are divided between pseudonormal and tumor overlap ROIs.

### 7.4.6 Euclidean distance

The following figures show the Euclidean distance values boxplots for the pseudonormal and overlapping regions, both at group and single-subject levels. Additionally, the matrices of the Euclidean distance have been displayed, and the plot of those values with respect to the tumor overlap percentage. All the statistically significant differences were calculated using a *Wilcoxon rank sum* test (significance level 5%).

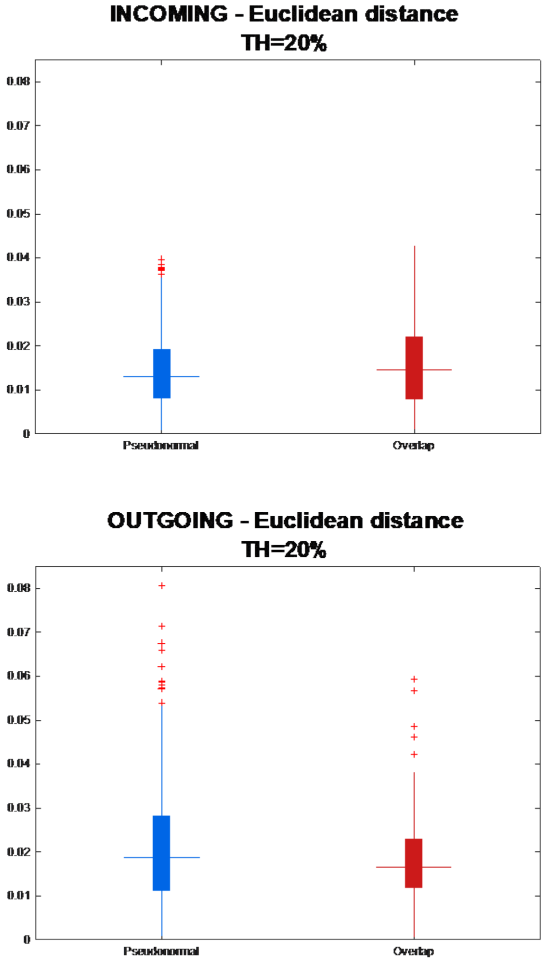

**Figure 7.49. Euclidean distance between healthy and brain tumor subjects.** The figures show the incoming and outgoing EC matrix Euclidean distance in Gradient 1 and Gradient 2 space, between a healthy subject and our twelve brain tumor subjects.

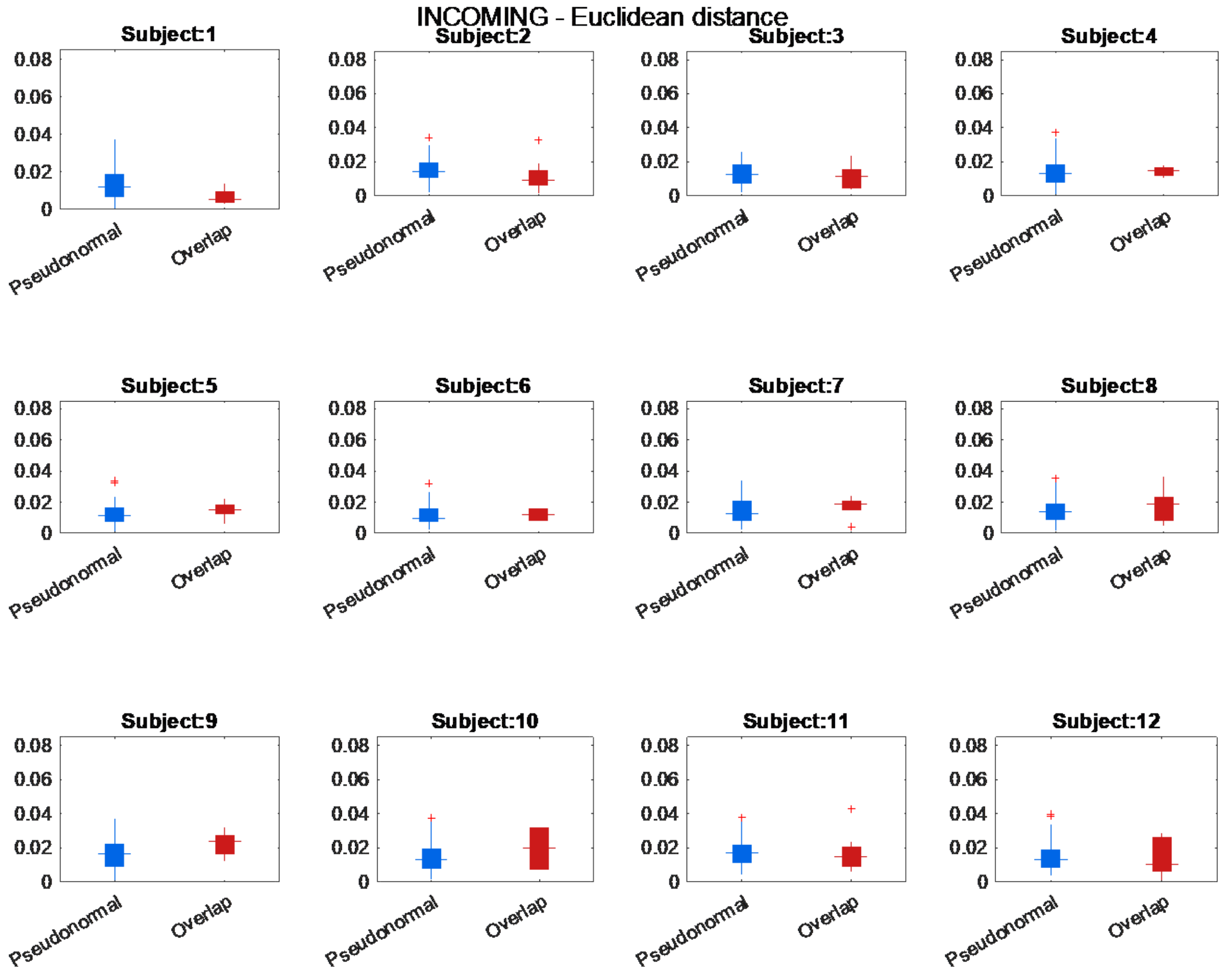

**Figure 7.50. Single-subject Euclidean distance for incoming links.** The figures show the incoming EC matrix Euclidean distance in Gradient 1 and Gradient 2 space, between a healthy subject and each brain tumor subject.

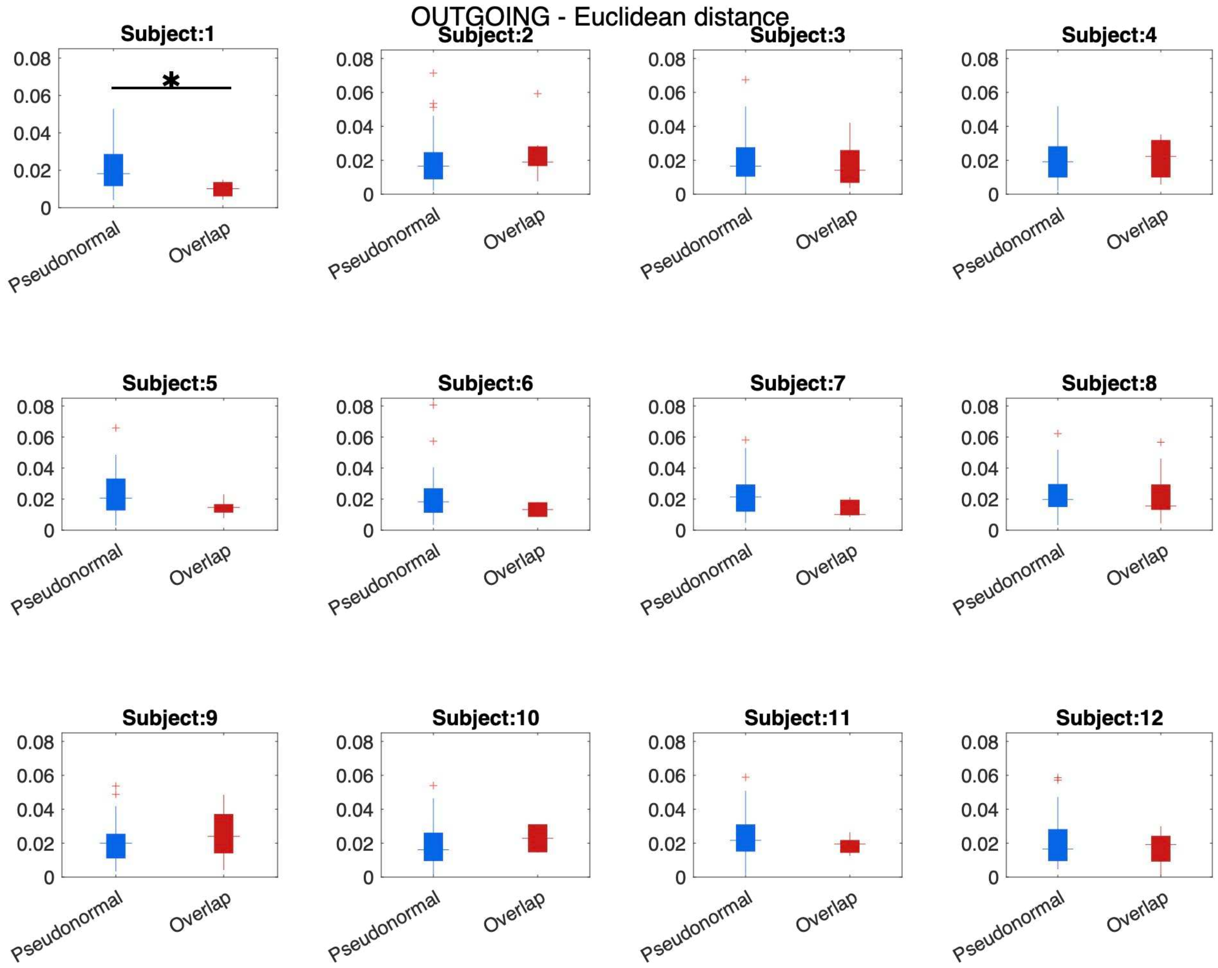

**Figure 7.51. Single-subject Euclidean distance for outgoing links.** The figures show the outgoing EC matrix Euclidean distance in Gradient 1 and Gradient 2 space, between a healthy subject and each brain tumor subject.

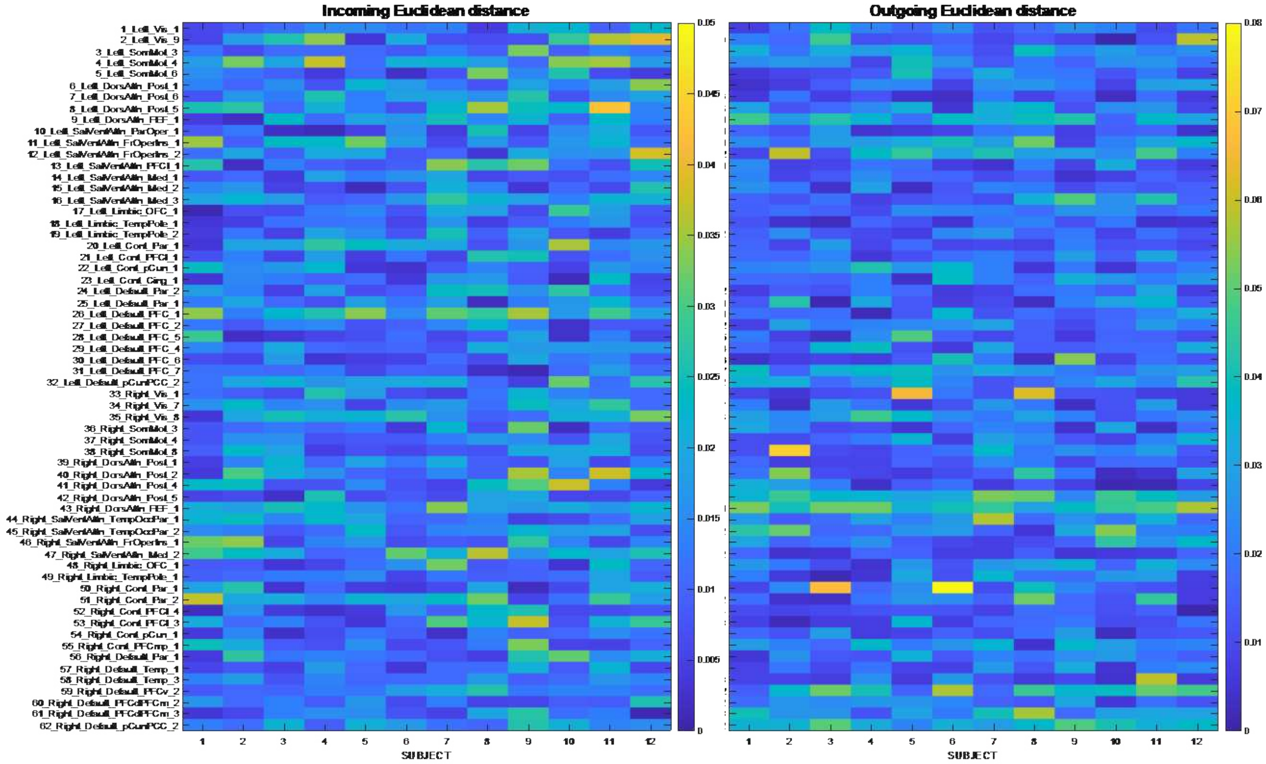

**Figure 7.52. Incoming and outgoing Euclidean distance matrices.** The figure shows, respectively, the incoming and outgoing Euclidean distance matrix for every parcel and every subject.

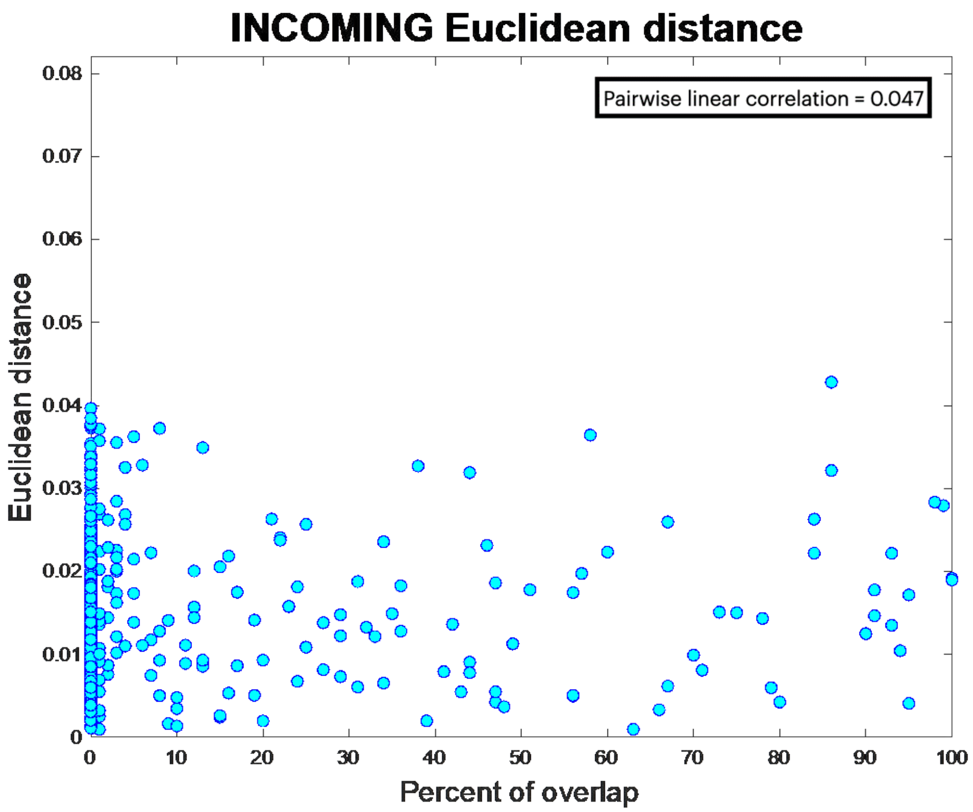

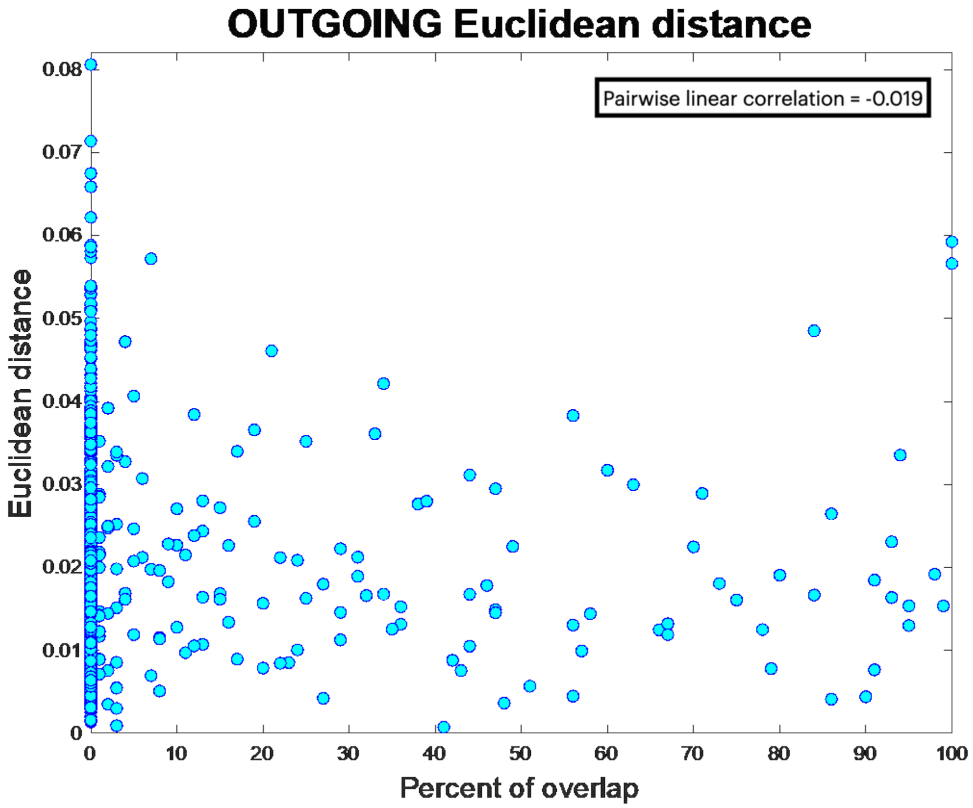

**Figure 7.53. Incoming and outgoing Euclidean distance for different tumor overlap percentages.** The figures respectively show the incoming and outgoing Euclidean distance values of the parcels for all subjects, by considering their tumor overlap percentages.

# 8 Discussion

In the following, the results presented in the previous chapter will be discussed, providing some insights into the estimated EC matrices and hemodynamic response functions, as well as their relation with metabolic parameters.

## 8.1 Sparse DCM setup

As mentioned before, the sparse DCM optimal noise variance was chosen on the basis of a balance between the empirical-simulated FC correlation and the empirical-simulated FCD Kolmogorov-Smirnov distance as shown in Figure 7.1 and Figure 7.2, by considering five reference subjects. The analysis carried out at subject-level provided a coherent result, since for both methods the optimal weight of the noise variance that maximized the eFC-sFC factor and minimized the KS distance is 1/10. This value is the same used for control subjects, thus it is inferred that the presence of the tumor has no significant effect in terms of noise variance.

Concerning the setting of the hemodynamic prior, is important to emphasize that this modified HRF prior is precisely a prior value, consequently, there are no irreversible changes in the estimates because these are always valued by considering also the likelihood provided by the input fMRI signals. The final hemodynamic prior indicated in Figure 7.10 is the result of a series of tests performed by considering the individual modifications for each parameter: the aim was to obtain a delayed HRF, which was less wide (higher Mean Transit Time) and with a flattened undershoot, as described in [35]. As a result, the variance weight of the parameter *k* has been increased, so as g and a. The physiological significance of these parameters should be emphasized; the *Signal Decay* gives us information about the elimination of the signal, which we expect to be much more variable in presence of a brain tumor. The same considerations can be made for the *Autoregolation* parameter, which should be different due to the effect of the tumor, or the *Resting Oxygen Extraction*, which reflects metabolic activities and in pathology such as the one studied can vary greatly between affected and unaffected regions.

## 8.2 Tumor overlap matrix

The tumor overlap matrix shown in Figure 7.11 gives percentage information about regions superimposed on the lesion area, which was then binarized with various thresholds. As depicted in Figure 7.15, this differentiation was made because, by varying the threshold imposed, the mean percent of overlapping regions decreases, so it makes sense to evaluate the analyses carried out subsequently with the three thresholds as a reference. Overall, by increasing the threshold it is noticed that the overlapping regions are distributed only in the parcels of the lesioned hemisphere, as shown in Table 6.1.

## 8.3 Relationship between [18F]FDG PET microparameters and HRF parameters

The purpose of this analysis was to create four hemodynamic classes differing from the reference one in order to find a relationship between the HRF parameters and the K1 and k3 [18F]FDG PET microparameters.

The first step consisted in identifying which pair of HRF parameters would have been the best to create these classes. As a result, we first corrected for data collinearity, by discarding HRF parameters that were most correlated with each other. For example, as shown in Figure 7.16, the *amplitude* is highly correlated with the *area under the curve,* the *fall slope*, and the *rise slope*, thereby we retained only *amplitude* to assess hemodynamic changes in the following analysis. Analogous assumptions were made for the other parameters and, for additional confirmation, the std ratio of each parameter in the overlapping regions with respect to the pseudonormal ROIs was estimated. This value suggests the extent to which a parameter is more or less sensitive to variations in overlap regions. As indicated in Figure 7.17, the parameters that appear to have a higher ratio are the *amplitude,* the *amplitude trough,* and the *full width at half maximum*, confirming their higher sensitivity to the presence of the brain glioma.

The three parameters were then considered two by two, thus *amplitude* vs *full width at half maximum*, *amplitude* vs *amplitude trough*, and *amplitude trough* vs *full width at half maximum* in order to define the hemodynamic classes. The classes were formed by ranking a given region according to the values of the two HRF parameters, as explained in chapter 5.5.2.

The mean parameter values follow the classification imposed, for example in Figure 7.18 we expect the *amplitude* of Class1 and Class2 to be higher than the reference value, otherwise, for Class3 and Class4, a lower value is expected and observed. Moreover, the mean HRF through classes reflects different shapes and values. In Figures 7.21 to 7.29, the estimated HRF is shown for the three pairs of parameters and the three selected thresholds. It was noticed that by increasing the threshold, thus being more conservative with respect to the tumor overlap, the shapes of the mean HRFs deviate more and more from the reference. This result proves that considering only regions with a high tumor overlap translates into a very altered HRF for different classes that are less sensitive to confounding factors. This result is consistent with what was found in the literature, in fact, it has been shown in many papers ([35] and [34]) that regions close to the tumor are highly altered.

The spatial distribution of the classes (Figures 7.30 to 7.32) highlights that the number of regions decreases with the threshold's increase, according to the assessments done with the number of overlapping regions. Additionally, their distribution focuses more and more on the hemisphere of the lesion.

After these HRF parameter analyses, the z-scored and averaged values of K1 and k3 for each class were visualized in Figures 7.33 to 38, to try to find a relationship or significant differences through the classes. The *amplitude* vs *FWHM* pair shows more significant differences at the k3 level than at K1. The same happens with *amplitude trough* vs *FWHM,* while *amplitude* vs *amplitude trough* even shows no significant difference for K1. Those results suggest that the k3 microparameter seems to be more sensitive to hemodynamic alterations, which should be expected since it reflects metabolic activity[13]. Indeed, the *oxygen extraction* and *Grubb's exponent* Balloon model parameters are related to the concept of metabolism, these respectively represent how much oxygen is extracted from the bloodstream for metabolic functions and the outflow of the venous balloon.
The hemodynamic parameters pair that actually cause more significant differences are those related to the shape and duration of the peak, like the *amplitude* and the *FWHM.* In fact, the reference is almost always statistically different from the other four classes, while Class 1 and Class 3 are always statistically different.

# 8.4 Graph theory and gradients

As expected, the EC matrix of a tumor subject (Figure 7.39) shows less strong connections between the brain regions, while a control subject presents a richer matrix. However, some particular patterns are preserved, for example, the diagonal bands of intra-network and inter-hemispheric connections, although these are much less pronounced. Additionally, the connections within the left hemisphere, the upper left sub-square, turn out to be full of connections for the control subject, while the tumor subject with a lesion on the left hemisphere loses this peculiarity. Generally, the matrix shows active connections and there do not appear to be any completely isolated areas. This can be explained by the fact that the tumor lesion is not an instantaneous pathology, as a stroke might be, but it is an expansive lesion allowing potential reorganization and compensation mechanisms.

As a preliminary analysis, the mean values of the EC matrix were extracted, by visualizing them into Violin plots (Figures 7.40 and 7.41). The main difference can be seen in the scale of the distributions between the values obtained considering subcortical regions (Figure 7.40) that result to be lower, and those without (Figure 7.41). By comparing controls with left/right tumor hemisphere patients, statistically significant differences have been found for the right tumor patients with respect to the controls in intra-left connections by including in the analysis subcortical regions. In the other case, without subcortical regions, statistical differences have been highlighted through controls and left tumor patients only in intra-right connections. However, these results should be confirmed with more subjects.

The next step has been to investigate the EC matrix through the theory of gradients. In Figure 7.43 it is evident that the incoming gradients seem to be much grouped and homogenous across networks with respect to the outgoing ones, which are more variable and scattered on the gradient space. By inspecting at group-level, there does not appear to be other discrepancies, for that reason the analysis was performed at the single-subject level. As noticed before, incoming gradients show a more localized distribution, and overlapping regions seem to be independent of the network they belong to, by placing themselves in the center of the distribution. This observation is confirmed by the analysis through the Silhouette coefficient: the overlapping regions seem to have significantly lower values, which translates into a reduced membership of the region in its own network. In the outgoing EC case (Figure 7.46), it was found a statistically significant difference. By inspecting the Silhouette values at single-subject level the statistical differences were identified in both incoming (only Subject 12) and outgoing (subjects 2,3, and 9) EC, confirming the hypothesis that for some subjects, the overlap regions do not seem to belong to their own network.

On the other hand, the Euclidean distance computation between controls and tumor subjects highlights an unexpected result since it seems that pseudonormal regions deviate more from reference ones with respect to overlapping ones (Figure 7.49). This could be explained by the fact that, especially in the case of outgoing links that give us information about the wide-ranging effect, the tumor seems to affect to regions far from the lesion area. The matrices in Figure 7.52 highlight that some regions like the *26_Left_Default* show a sort of band of higher values of Euclidean distance, and globally the incoming EC has lower distance values than the outgoing EC.
The scatter plots in Figure 7.53 represent a first attempt to look for a correlation between the percentage of overlap and the Euclidean distance, but no linear correlation was found (0.047 and -0.019). This result could suggest that directed connectivity disruptions (especially in the outgoing case) are not linearly correlated with the tumor volume, but the effect of the lesion is widespread across the whole brain connectome.

# 9 Conclusions and future work

In this thesis, the ability of the sparse DCM algorithm developed by Prando et al.[5] to capture whole-brain neural and hemodynamic disruptions in brain gliomas has been assessed. The estimated subject-level EC matrices and region-wise HRFs were deeply analyzed in order to deepen the effective connectivity alterations and the hemodynamic response variability in presence of a tumor lesion.

In general, additional investigations are needed, in order to optimize the procedure of analysis in the identification of connectivity and hemodynamic alterations induced by tumors. Although the algorithm is able to reliably work at the individual level, the testing of sparse DCM on a larger cohort of tumor individuals is necessary in order to validate preliminary results obtained from the analyzed subjects. Moreover, a larger dataset would make it possible to look into how individual traits like age, gender, and cognitive abilities affect hemodynamic parameters and effective connections. Additionally, in order to determine how the lesion's three-dimensional conformation projects its pathogenic consequences on the cortical surface, EC estimates should be informed with structural information derived from the lesion's size and position. To provide a more detailed description of EC changes following brain plasticity-related adaptations, other connectivity measures developed from graph theory (e.g., clustering coefficient, betweenness centrality, participation coefficient, etc.) should be considered.

Finally, the results obtained from the comparison between hemodynamic response parameters and K1 and k3 PET microparameters represent the starting point for a more in-depth analysis of this link in the tumor patient's case. Indeed the study of brain effective connectivity in pathology is in its infancy. For both hemodynamic and connectivity analyses, the goal would be to evaluate and reintroduce the pipeline applied in a larger dataset, so as to obtain more robust and reliable statistically significant differences.

In conclusion, the findings of this work may open up additional pathways for understanding the widespread effects of tumors and other complicated neuropathological conditions, including motor disorders, mental illnesses, and others, which are linked to the dysfunction of neural networks. According to this perspective, studies on hemodynamic and connectivity alterations should offer a strong foundation for new prognostic factors of cognitive and behavioral deficits caused by brain lesions, in addition to simulation tools for creating specialized therapeutic regimens based on pathophysiological mechanisms defining brain disorders.

# Bibliography

[1] M. Rubinov and O. Sporns, “Complex network measures of brain connectivity: Uses and interpretations,” *Neuroimage*, vol. 52, no. 3, pp. 1059–1069, Sep. 2010, doi: 10.1016/J.NEUROIMAGE.2009.10.003.

[2] E. Silvestri *et al.*, “Widespread cortical functional disconnection in gliomas: an individual network mapping approach,” *Brain Commun*, vol. 4, no. 2, Mar. 2022, doi: 10.1093/BRAINCOMMS/FCAC082.

[3] L. Liu, H. Zhang, I. Rekik, X. Chen, Q. Wang, and D. Shen, “Outcome prediction for patient with high-grade gliomas from brain functional and structural networks,” *Lecture Notes in Computer Science (including subseries Lecture Notes in Artificial Intelligence and Lecture Notes in Bioinformatics)*, vol. 9901 LNCS, pp. 26–34, 2016, doi: 10.1007/978-3-319-46723-8_4/FIGURES/2.

[4] K. J. Friston, L. Harrison, and W. Penny, “Dynamic causal modelling,” *Neuroimage*, vol. 19, no. 4, pp. 1273–1302, Aug. 2003, doi: 10.1016/S1053-8119(03)00202-7.

[5] G. Prando, M. Zorzi, A. Bertoldo, M. Corbetta, M. Zorzi, and A. Chiuso, “Sparse DCM for whole-brain effective connectivity from resting-state fMRI data,” *Neuroimage*, vol. 208, p. 116367, Mar. 2020, doi: 10.1016/J.NEUROIMAGE.2019.116367.

[6] “Cellular respiration review (article) | Khan Academy.” https://www.khanacademy.org/science/high-school-biology/hs-energy-and-transport/hs-cellular-respiration/a/hs-cellular-respiration-review (accessed Nov. 21, 2022).

[7] M. H. Lee, C. D. Smyser, and J. S. Shimony, “Resting-State fMRI: A Review of Methods and Clinical Applications,” *AJNR Am J Neuroradiol*, vol. 34, no. 10, p. 1866, Oct. 2013, doi: 10.3174/AJNR.A3263.

[8] H. F. Wehrl *et al.*, “Simultaneous PET-MRI reveals brain function in activated and resting state on metabolic, hemodynamic and multiple temporal scales,” *Nature Medicine 2013 19:9*, vol. 19, no. 9, pp. 1184–1189, Aug. 2013, doi: 10.1038/nm.3290.

[9] M. E. Phelps, S. C. Huang, E. J. Hoffman, C. Selin, L. Sokoloff, and D. E. Kuhl, “Tomographic measurement of local cerebral glucose metabolic rate in humans with (F-18)2-fluoro-2-deoxy-D-glucose: Validation of method,” *Ann Neurol*, vol. 6, no. 5, pp. 371–388, Nov. 1979, doi: 10.1002/ANA.410060502.

[10] M. Reivich *et al.*, “The [18F]fluorodeoxyglucose method for the measurement of local cerebral glucose utilization in man.,” *Circ Res*, vol. 44, no. 1, pp. 127–137, 1979, doi: 10.1161/01.RES.44.1.127.

[11] A. Bertoldo, P. Peltoniemi, V. Oikonen, J. Knuuti, P. Nuutila, and C. Cobelli, "Kinetic modeling of [18F]FDG in skeletal muscle by PET: A four-compartment five-rate-constant model," *Am J Physiol Endocrinol Metab*, vol. 281, no. 3 44-3, pp. 524–536, 2001, doi: 10.1152/AJPENDO.2001.281.3.E524/ASSET/IMAGES/LARGE/H10910476007.JPEG.

[12] "Kinetic modeling in positron emission tomography - PubMed." https://pubmed.ncbi.nlm.nih.gov/12072847/ (accessed Dec. 08, 2022).

[13] J. Zhang, K. Chu, E. A. Hazlett, and M. S. Buchsbaum, "A study of cerebral glucose metabolism and hemodynamic response in schizophrenia," *Proceedings - 2011 4th International Conference on Biomedical Engineering and Informatics, BMEI 2011*, vol. 1, pp. 77–81, 2011, doi: 10.1109/BMEI.2011.6098316.

[14] S. A. Sheth, M. Nemoto, M. Guiou, M. Walker, N. Pouratian, and A. W. Toga, "Linear and Nonlinear Relationships between Neuronal Activity, Oxygen Metabolism, and Hemodynamic Responses," *Neuron*, vol. 42, no. 2, pp. 347–355, Apr. 2004, doi: 10.1016/S0896-6273(04)00221-1.

[15] K. J. Friston, A. Mechelli, R. Turner, and C. J. Price, "Nonlinear Responses in fMRI: The Balloon Model, Volterra Kernels, and Other Hemodynamics," *Neuroimage*, vol. 12, no. 4, pp. 466–477, Oct. 2000, doi: 10.1006/NIMG.2000.0630.

[16] X. Hu and E. Yacoub, "The story of the initial dip in fMRI," *Neuroimage*, vol. 62, no. 2, pp. 1103–1108, Aug. 2012, doi: 10.1016/J.NEUROIMAGE.2012.03.005.

[17] R. B. Buxton, E. C. Wong, and L. R. Frank, "Dynamics of blood flow and oxygenation changes during brain activation: The balloon model," *Magn Reson Med*, vol. 39, no. 6, pp. 855–864, 1998, doi: 10.1002/MRM.1910390602.

[18] R. B. Buxton, K. Uludağ, D. J. Dubowitz, and T. T. Liu, "Modeling the hemodynamic response to brain activation," *Neuroimage*, vol. 23 Suppl 1, no. SUPPL. 1, 2004, doi: 10.1016/J.NEUROIMAGE.2004.07.013.

[19] A. A. Phillips, F. H. Chan, M. M. Z. Zheng, A. v. Krassioukov, and P. N. Ainslie, "Neurovascular coupling in humans: Physiology, methodological advances and clinical implications," *Journal of Cerebral Blood Flow and Metabolism*, vol. 36, no. 4, pp. 647–664, 2015, doi: 10.1177/0271678X15617954.

[20] O. Sporns, "Graph theory methods: applications in brain networks," *https://doi.org/10.31887/DCNS.2018.20.2/osporns*, vol. 20, no. 2, pp. 111–120, 2022, doi: 10.31887/DCNS.2018.20.2/OSPORNS.

[21] E. Bullmore and O. Sporns, "Complex brain networks: graph theoretical analysis of structural and functional systems," *Nature Reviews Neuroscience 2009 10:3*, vol. 10, no. 3, pp. 186–198, Feb. 2009, doi: 10.1038/nrn2575.

[22] O. Sporns, “The human connectome: a complex network,” *Ann N Y Acad Sci*, vol. 1224, no. 1, pp. 109–125, Apr. 2011, doi: 10.1111/J.1749-6632.2010.05888.X.

[23] E. W. Lang, A. M. Tomé, I. R. Keck, J. M. Górriz-Sáez, and C. G. Puntonet, “Brain connectivity analysis: A short survey,” *Comput Intell Neurosci*, vol. 2012, 2012, doi: 10.1155/2012/412512.

[24] “(PDF) Multimodal Imaging Brain Connectivity Analysis (MIBCA) toolbox.” https://www.researchgate.net/publication/274735027_Multimodal_Imaging_Brain_Connectivity_Analysis_MIBCA_toolbox (accessed Nov. 21, 2022).

[25] J. D. Medaglia and D. S. Bassett, “Network Analyses and Nervous System Disorders,” Jan. 2017, Accessed: Nov. 21, 2022. [Online]. Available: https://www.researchgate.net/publication/312058510_Network_Analyses_and_Nervous_System_Disorders

[26] G. Lioi, V. Gripon, A. Brahim, F. Rousseau, and N. Farrugia, “Gradients of connectivity as graph Fourier bases of brain activity,” *Network Neuroscience*, vol. 5, no. 2, pp. 322–336, Jun. 2021, doi: 10.1162/NETN_A_00183.

[27] R. Vos de Wael *et al.*, “BrainSpace: a toolbox for the analysis of macroscale gradients in neuroimaging and connectomics datasets,” *Communications Biology 2020 3:1*, vol. 3, no. 1, pp. 1–10, Mar. 2020, doi: 10.1038/s42003-020-0794-7.

[28] D. S. Margulies *et al.*, “Situating the default-mode network along a principal gradient of macroscale cortical organization,” *Proc Natl Acad Sci U S A*, vol. 113, no. 44, pp. 12574–12579, Nov. 2016, doi: 10.1073/PNAS.1608282113/-/DCSUPPLEMENTAL/PNAS.201608282SI.PDF.

[29] Ş. Bayrak *et al.*, “The impact of ischemic stroke on connectivity gradients,” *Neuroimage Clin*, vol. 24, Jan. 2019, doi: 10.1016/J.NICL.2019.101947.

[30] K. J. Friston, J. Kahan, B. Biswal, and A. Razi, “A DCM for resting state fMRI,” *Neuroimage*, vol. 94, pp. 396–407, Jul. 2014, doi: 10.1016/J.NEUROIMAGE.2013.12.009.

[31] Q. T. Ostrom *et al.*, “The epidemiology of glioma in adults: a ‘state of the science’ review,” *Neuro Oncol*, vol. 16, no. 7, pp. 896–913, Jul. 2014, doi: 10.1093/NEUONC/NOU087.

[32] L. Liu *et al.*, “Overall survival time prediction for high-grade glioma patients based on large-scale brain functional networks,” *Brain Imaging and Behavior 2018 13:5*, vol. 13, no. 5, pp. 1333–1351, Aug. 2018, doi: 10.1007/S11682-018-9949-2.

[33] Q. T. Ostrom, S. S. Francis, and J. S. Barnholtz-Sloan, “Epidemiology of Brain and Other CNS Tumors,” *Curr Neurol Neurosci Rep*, vol. 1, p. 3, 1910, doi: 10.1007/s11910-021-01152-9.

[34] L. Wang, D. Chen, J. Olson, S. Ali, T. Fan, and H. Mao, “Re-examine tumor-induced alterations in hemodynamic responses of BOLD fMRI: implications in presurgical brain mapping,” *http://dx.doi.org/10.1258/ar.2012.120118*, vol. 53, no. 7, pp. 802–811, Sep. 2012, doi: 10.1258/AR.2012.120118.

[35] M. K. Montgomery *et al.*, “Glioma-Induced Alterations in Neuronal Activity and Neurovascular Coupling during Disease Progression,” *Cell Rep*, vol. 31, no. 2, Apr. 2020, doi: 10.1016/j.celrep.2020.03.064.

[36] E. Silvestri *et al.*, “Assessment of structural disconnections in gliomas: comparison of indirect and direct approaches,” *Brain Struct Funct*, vol. 227, no. 9, pp. 3109–3120, Dec. 2022, doi: 10.1007/S00429-022-02494-X/FIGURES/4.

[37] M. Moretto *et al.*, “The dynamic functional connectivity fingerprint of high-grade gliomas,” Nov. 2022, doi: 10.21203/RS.3.RS-2285853/V1.

[38] E. Silvestri *et al.*, “Widespread cortical functional disconnection in gliomas: an individual network mapping approach,” *Brain Commun*, vol. 4, no. 2, Mar. 2022, doi: 10.1093/BRAINCOMMS/FCAC082.

[39] C. N. Ladefoged *et al.*, “A multi-centre evaluation of eleven clinically feasible brain PET/MRI attenuation correction techniques using a large cohort of patients,” *Neuroimage*, vol. 147, pp. 346–359, Feb. 2017, doi: 10.1016/J.NEUROIMAGE.2016.12.010.

[40] A. Schaefer *et al.*, “Local-Global Parcellation of the Human Cerebral Cortex from Intrinsic Functional Connectivity MRI,” *Cerebral Cortex*, vol. 28, no. 9, pp. 3095–3114, Sep. 2018, doi: 10.1093/CERCOR/BHX179.

[41] C. Caballero-Gaudes and R. C. Reynolds, “Methods for cleaning the BOLD fMRI signal,” *Neuroimage*, vol. 154, pp. 128–149, Jul. 2017, doi: 10.1016/J.NEUROIMAGE.2016.12.018.

[42] J. E. Chen and G. H. Glover, “BOLD fractional contribution to resting-state functional connectivity above 0.1 Hz,” *Neuroimage*, vol. 107, pp. 207–218, Feb. 2015, doi: 10.1016/J.NEUROIMAGE.2014.12.012.

[43] R. Henson and K. Friston, “Convolution Models for fMRI,” *Statistical Parametric Mapping: The Analysis of Functional Brain Images*, pp. 178–192, Jan. 2007, doi: 10.1016/B978-012372560-8/50014-0.

[44] S. Ryali, T. Chen, A. Padmanabhan, W. Cai, and V. Menon, “Development and validation of consensus clustering-based framework for brain segmentation using resting fMRI,” *J Neurosci Methods*, vol. 240, pp. 128–140, Jan. 2015, doi: 10.1016/J.JNEUMETH.2014.11.014.

[45] G. Deco, M. L. Kringelbach, V. K. Jirsa, and P. Ritter, "The dynamics of resting fluctuations in the brain: metastability and its dynamical cortical core," *Scientific Reports 2017 7:1*, vol. 7, no. 1, pp. 1–14, Jun. 2017, doi: 10.1038/s41598-017-03073-5.

[46] G. Deco, A. Ponce-Alvarez, D. Mantini, G. L. Romani, P. Hagmann, and M. Corbetta, "Resting-State Functional Connectivity Emerges from Structurally and Dynamically Shaped Slow Linear Fluctuations," *The Journal of Neuroscience*, vol. 33, no. 27, p. 11239, Jul. 2013, doi: 10.1523/JNEUROSCI.1091-13.2013.

[47] D. J. Lurie *et al.*, "Questions and controversies in the study of time-varying functional connectivity in resting fMRI," *Network Neuroscience*, vol. 4, no. 1, p. 30, Feb. 2020, doi: 10.1162/NETN_A_00116.

[48] K. L. West *et al.*, "BOLD hemodynamic response function changes significantly with healthy aging," *Neuroimage*, vol. 188, pp. 198–207, Mar. 2019, doi: 10.1016/J.NEUROIMAGE.2018.12.012.

[49] P. Zanotti-Fregonara, K. Chen, J. S. Liow, M. Fujita, and R. B. Innis, "Image-derived input function for brain PET studies: many challenges and few opportunities," *J Cereb Blood Flow Metab*, vol. 31, no. 10, pp. 1986–1998, Oct. 2011, doi: 10.1038/JCBFM.2011.107.

[50] M. Tonietto, G. Rizzo, M. Veronese, and A. Bertoldo, "Modelling arterial input functions in positron emission tomography dynamic studies," *Proceedings of the Annual International Conference of the IEEE Engineering in Medicine and Biology Society, EMBS*, vol. 2015-November, pp. 2247–2250, Nov. 2015, doi: 10.1109/EMBC.2015.7318839.

[51] M. Castellaro *et al.*, "A Variational Bayesian inference method for parametric imaging of PET data," *Neuroimage*, vol. 150, pp. 136–149, Apr. 2017, doi: 10.1016/J.NEUROIMAGE.2017.02.009.

[52] "Max Planck Institut Leipzig Mind-Brain-Body Dataset - LEMON." http://fcon_1000.projects.nitrc.org/indi/retro/MPI_LEMON.html (accessed Dec. 09, 2022).